THE FAR-INFRARED POWDER ABSORPTION SPECTRA OF BIS-TETRAMETHYLTETRASELENAFULVALENE SALTS [$(TMTSF)_2X$, X=(PF_6, AsF_6, SbF_6, BF_4, ClO_4 and ReO_4)]

By

CHRISTOPHER C. HOMES

B.Sc.(Hon.), McMaster University, 1983

A THESIS SUBMITTED IN PARTIAL FULFILLMENT OF
THE REQUIREMENTS FOR THE DEGREE OF
MASTER OF SCIENCE
in
THE FACULTY OF GRADUATE STUDIES
(DEPARTMENT OF PHYSICS)

We accept this thesis as conforming
to the required standard.

THE UNIVERSITY OF BRITISH COLUMBIA

November 1985

In presenting this thesis in partial fulfilment of the requirements for an advanced degree at the University of British Columbia, I agree that the Library shall make it freely available for reference and study. I further agree that permission for extensive copying of this thesis for scholarly purposes may be granted by the Head of the Department or by his or her representatives. It is understood that copying or publication of this thesis for financial gain shall not be allowed without my written permission.

Department of Physics

The University of British Columbia
6224 Agriculture Road
Vancouver, B.C.
CANADA V6T 2A6

Date: November 27, 1985

ABSTRACT

The far-infrared powder absorption spectra from 20–250 cm^{-1} have been examined in a series of six protonated and deuterated $(TMTSF)_2X$ compounds, with X=PF_6, AsF_6 and SbF_6 (octahedral anions) and X=BF_4, ClO_4 and ReO_4 (tetrahedral anions) as a function of temperature from 10K to 290K . The octahedral-anion spectra are all very similar, having 4 sharp resonances which have been attributed to three lattice modes and one internal mode. These assignments were made on the basis of isotope shifts upon deuteration, and wave number temperature dependence. The intensity of the lines is roughly proportional to the d.c. conductivity, and indicate a phase transition around 12K. The spectra of the tetrahedral-anion compounds are also similar. They show, however, extra structure below the anion-ordering temperature, T_{AO}, including a strong feature at 30 cm^{-1}. The 30-cm^{-1} feature shows a magnetic field depedence and may be related to the superconductivity. Simple one- and two-dimensional models are presented that indicate that this feature may be due to the activation of a transverse acoustic zone-boundary phonon, due to zone-folding, which accompanies the formation of a superlattice created by the anion-ordering transition.

Extended measurements from 100–300 cm^{-1} have been performed on protonated AsF_6 and SbF_6 compounds, allowing the identification of two internal modes. Extended measurements from 100–400 cm^{-1} have been performed on protonated and deuterated BF_4 and ReO_4 compounds, which show internal modes of both the TMTSF and anion molecules, and a torsional mode of the TMTSF methyl groups.

These assignments were made on the basis of isotope shifts upon deuteration and an extensive published vibrational analysis of TMTSF.

TABLE OF CONTENTS

LIST OF TABLES

LIST OF FIGURES

ACKNOWLEDGEMENTS

I would like to thank my supervisor, Dr. J.E. Eldridge for his help with the experiments and many useful suggestions.

I would also like to thank Dr. G.S. Bates of the Department of Chemistry at U.B.C. for preparing the crystals, and Dr. Frances E. Bates for valuble discussion.

I am grateful to Mary-Ann Potts, as well as the electronics shop, for setting up the data acquistion system. I would like to thank Kevin Kornelsen for his help in the lab.

During this research, I have been supported by a Natural Sciences and Engineering Research Council (NSERC) Postgraduate Scholarship. This work was also supported by Grant No. A5653 from NSERC.

CHAPTER 1

INTRODUCTION

1.1 Quasi-one-dimensional Conductors

Organic molecules display an amazing diversity of forms and have many different properties. One of the physical properties that organic molecules seldom display, however, is electrical conductivity and even more rarely, superconductivity.

The first stable organic conductors were synthesized in the early 1960's. The organic molecule tetracyanoquinodimethane, or TCNQ, was prepared in 1960 by workers at E.I du Pont de Nemours & Company. Little energy is needed to introduce an extra electron into TCNQ and the negatively charged structure that results is chemically stable. TCNQ by itself, however, is not able to conduct electrons, and so in an electronically neutral system there is no tendancy for the electrons to move from one TCNQ molecule to another. If the TCNQ molecules (anions) can obtain a fraction of electronic charge from other atoms or molecules (cations), the material can become conductive and is called a charge transfer salt. In the cesium salt of TCNQ, $(Cs^{+})_2(TCNQ^{-\frac{2}{3}})_3$ for example, each cesium atom gives up an average of two-thirds of an electron to each TCNQ molecule. Thus, two out of every three TCNQ molecules become negatively charged, and if an electric field is imposed, the extra electrons can move from the charged TCNQ molecules to the neutral ones. Another TCNQ charge transfer salt, tetrathiafulvalene-tetracyanoquinodimethane (TTF-TCNQ), was synthesized in 1973 by Cowan and Ferraris, and by Heeger

and Garito. In the solid form the TTF and TCNQ molecules stack in seperate columns, and electrons are donated from the TTF stack to the TCNQ stack. A fractional charge of 0.59 electron per molecule is transferred from one stack to another. Because of the electron transfer there can be a net motion of electrons along both stacks; hence the material is conductive. At room temperature TTF-TCNQ has a conductivity of $\sim 2000\ (\Omega\,\mathrm{cm})^{-1}$, or about three orders of magnitude smaller than that of copper.

The architecture of the TTF-TCNQ crystal gives rise to a striking electrical property: the material is highly conductive in one direction only. The most favourable direction is 500 times as conductive as the least favourable direction. This is because the TTF and TCNQ molecules are large planar molecules, with the valence $\pi-$ electrons located above and below the planar framework. They stack together like pancakes so that the orbitals of the valence $\pi-$ electrons overlap, allowing the electrons to move freely up and down the stacks. The reason for the anisotropy is that the TTF and TCNQ molecules are stacked in parallel planes, with little overlap between adjacent stacks. Compounds that display this anisotropic behavior are called quasi-one-dimensional solids or linear-chain materials.

1.2 High Temperature Organic Superconductors

Some of the highly conducting inorganic linear-chain solids have been known for a long time. Tetracyanoplatinate, or TCP, was first synthesized in 1842 and the material poly(sulfurnitride), $(SN)_x$, in 1910. However, the properties of TCP and $(SN)_x$ were not examined until the 1970's. There are two good historical reviews in the Scientific American[2,3].

The search for new linear chain compounds was prompted by W.A. Little, who in 1964 proposed an alternative method for the formation of Cooper pairs[4]. The theory of superconductivity in metals was formulated in 1957 by John Bardeen, Leon Cooper and J. Robert Schriffer[5]. Superconductivity results when the electrons

in a metal form into bound pairs called Cooper pairs. As an electron moves through the lattice there is an electrostatic attraction between the electron and the positive ions around it. As the electron moves away, the positive ions remain displaced for a comparatively long time since the vibrational motion of the lattice is much slower than the motion of the electron. This lattice distortion creates a temporary region of positive charge to which another electron is attracted and a Cooper pair is formed. At high temperatures, the effect is destroyed by the random, thermal vibrations of the lattice, but it can emerge below a certain critical temperature (T_c) and cause the electrons that make up each Cooper pair to act as if they were connected by a weak spring. The electrons vibrate back and forth in response to the variations in charge density set up by their own motions in the atomic lattice.

Electrical conduction in a superconductor is caused by the net motion of the centers of mass of the Cooper pairs, whereas electrical conduction in an ordinary metal is caused by the net motion of individual valence electrons. A quantum mechanical aspect of the Cooper pairs is that when the electrons enter the bound state, the total energy of the system is minimized if all of the Cooper pairs have the same momentum. If there is no current flowing through the material, the momentum of each Cooper pair is zero: the electrons in each pair are thereby constrained to move in opposite directions with respect to the lattice, and the velocity of each center of mass must be zero. When there is a current in the material, the electrons in each pair must move in such a way that all of the Cooper pairs have the same constant momentum. Every motion of one electron that threatens to break up the Cooper pair must be immediately compensated for by its partner so that equilibrium is always maintained.

This itself does not explain why the resistance in a superconductor is zero. In an ordinary metal, electrical resistance is the result of the scattering of moving electrons by imperfections in the lattice and by the thermal vibrations of the lattice at any temperature above absolute zero. Each time an electron is scattered, the

energy of the electronic system is reduced by a small amount, and there is a corresponding increase in the vibrational energy of the lattice at a finite temperature. The resistivity of a perfectly regular metallic lattice would theoretically be zero at absolute zero because there is no vibrational energy available in the lattice for the scattering of electrons.

In a superconductor, the electrical resistivity can be zero at finite temperature because once the Cooper pairs are put into motion by an electric field, they acquire a net momentum. The net momentum cannot decay through scattering: unlike the scattering of an ordinary electron which costs little energy, the scattering of the Cooper pair costs much more energy than the binding energy which holds the electrons together. Furthermore, in the highly organized superconducting state, changing the momentum of one Cooper pair requires a change in the momenta of all of the other Cooper pairs as well. The energy needed to redistribute the momenta is much larger than the vibrational energy available in the lattice at low temperature and hence the Cooper pairs do not encounter resistance as they move through the lattice. At higher temperatures, it is possible for the lattice to redistribute the momenta and break up the pairs, and the electrons are scattered as they are in an ordinary conductor; the resistance of the material jumps from zero to some finite value.

Since the condensation of electrons into Cooper pairs depends on deformations of the atomic lattice, T_c is related to the "stiffness" of the lattice: its resistance to deformation by a passing electron. If the atoms in the lattice have small masses and the interatomic bonds are relatively "soft", the deformations are large compared with the deformations caused by thermal vibrations and T_c is high. More precisely, the critical temperature varies inversly with the square root of the mass of the anions in the lattice[5]

$$T_c \sim (M_{ion})^{-\frac{1}{2}}. \qquad (1-1)$$

Little proposed a way that Cooper pairs might be produced without lattice distortions. He consided a large organic molocule consisting of two parts: a long chain of carbon atoms called the "spine" and a series of arms or side chains attatched to the spine. Each molecule would be a hydrocarbon with loosely bound valence electrons, such as an organic dye. An electron travelling along the spine of the carbon atoms would repel the outer electrons of the hydrocarbon molecules, thus creating a region of net positive charge on the parts of the side chains nearest to the spine. A second electron moving along the spine in the opposite direction, would be attracted by the relatively dense positive charge and indirectly to the first electron thus forming a Cooper pair. The region of enhanced positive charge is created by the displacement of electrons rather than atoms in a lattice. Since the electron is about 100,000 times less massive than a typical ion, equation 1–1 gives us that T_c for this material should be increased by a factor of $\sim$ 300. Such a material would be superconducting at room temperature, and in principle the superconducting state could be stable up to 2000 K. It is known from theoretical calculations that it is impossible to sustain the formation of Cooper pairs in a strictly one-dimensional conductor at any temperature above absolute zero. Thus the strictly one-dimensional superconductor cannot exist. In any real molecular system, however, the conductors are only approximately one-dimensional, and there will be some interaction between the chains that will allow a Cooper pair to jump from one stack to another. Hence the theoretical obstacle to superconductivity in one-dimension is not a practical one. While no one has succeeded in constructing the sort of organic molecule that Little envisoned, the idea has generated a strong interest in organic superconductors, and the possibilities of technological applications for such materials have been discussed[3].

1.3 The $(TMTSF)_2X$ Charge Transfer Salts

The organic conductor TTF-TCNQ is a good electrical conductor at room

temperature. As the temperature is lowered the conductivity increases in a metallic fashion until at about 60 K the uniform molecular spacing in the stacks gives way to a more energetically favourable structure in which the seperation of adjacent molecules in the stack changes. The result of this structural change is to alter the electronic density along the chain. The charge density undergoes a periodic concentration and rarefaction that is called a Peierls distortion or a charge-density wave (CDW)[6].

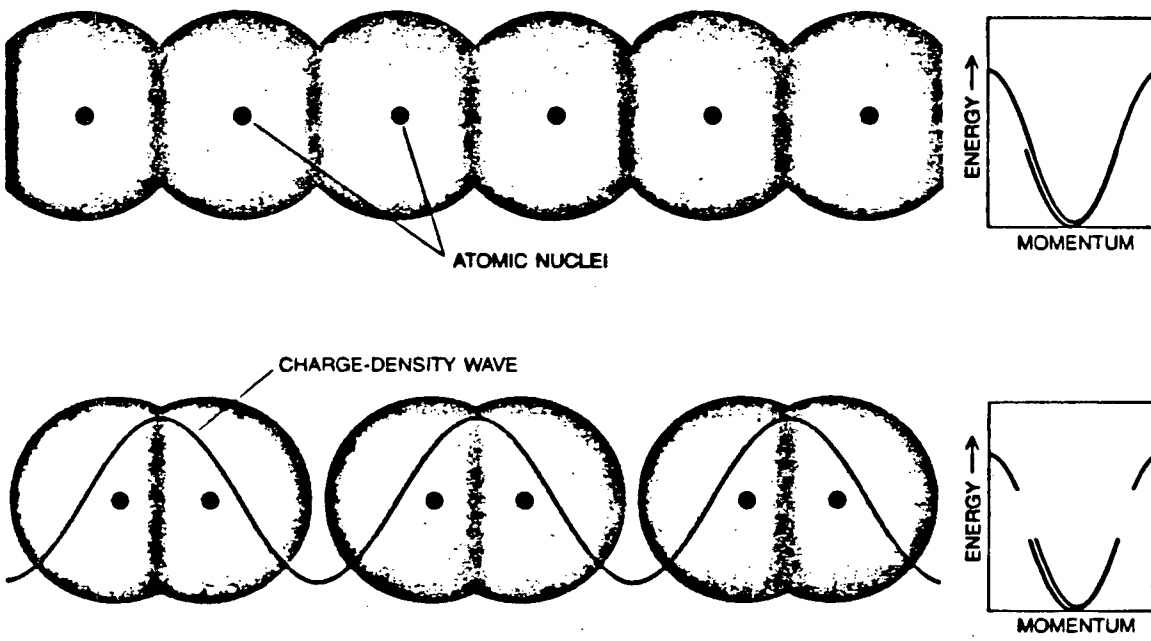

Figure 1-1 The dimerization of a linear-chain material (Peierls distortion) resulting in the formation of a charge-density wave. The diagrams at the right depict the creation of a band gap due to band splitting[3].

The onset of a CDW causes the partially filled conduction-electron band to split into two bands, the lower one completely filled, the upper one completely empty. Conduction may occur only if electrons are promoted across the energy gap by thermal activation or photon-absorption. Thus, the material changes suddenly

from a conductor to a semiconductor or an insulator. In TTF-TCNQ the CDW transition occurs at 53 K. While the valence electrons are no longer available for free conduction, an alternate mechanism for conduction is the sliding CDW[7], which slides along the lattice stacks. The electrons "surf-ride" on the CDW. It is this effect which is responsible for the enhanced conductivity in TTF-TCNQ at $\sim$ 68 K[8,9]. As the temperature is lowered below 58 K for TTF-TCNQ, there is a decrease in the conductivity. This is attributed to the CDW becoming pinned to charged impurities, lattice defects and significant interchain coupling[10]. In other words the oppositely-charged CDW's on adjacent stacks are pinned to each other by Coulomb attraction, as well as to impurities and defects.

This motivated the search for a new organic conductor which would have small molecules in the anion stacks that would not be susceptable to CDW formation, thus allowing sliding CDW's and suppressing pinning due to interchain coupling. In 1979 a fascinating new series of charge transfer salts were synthesized by K. Bechgaard *et al*[11]. The *bis*-tetramethyltetraselenafulvalene-X compounds have the chemical form $(TMTSF)_2X$, where X is any one of a number of relatively small inorganic radical anions *e.g.* hexafluorophosphate (PF_6), hexafluoroarsenate (AsF_6), hexafluoroantimonate (SbF_6), tetrafluoroborate (BF_4), perchlorate (ClO_4), perrhenate (ReO_4), nitrate (NO_3), etc., and are known as Bechgaard salts.

1.4 Structure of $(TMTSF)_2X$ Salts

The crystal structure is shown in Fig. 1–2. It is triclinic with a $P\bar{1}$ (C_i^1) space group[12]. The anion positions are centers of inversion symmetry, but no other symmetry operations apply to the crystal lattice. The planar TMTSF molecules are slightly dimerized as they stack together in a zig-zag fashion to form a linear chain. The chain direction is the **a**-axis. The stacks are tightly arranged along the interchain or **b**-axis, forming a sheet in the **ab**-plane. The anions form a well

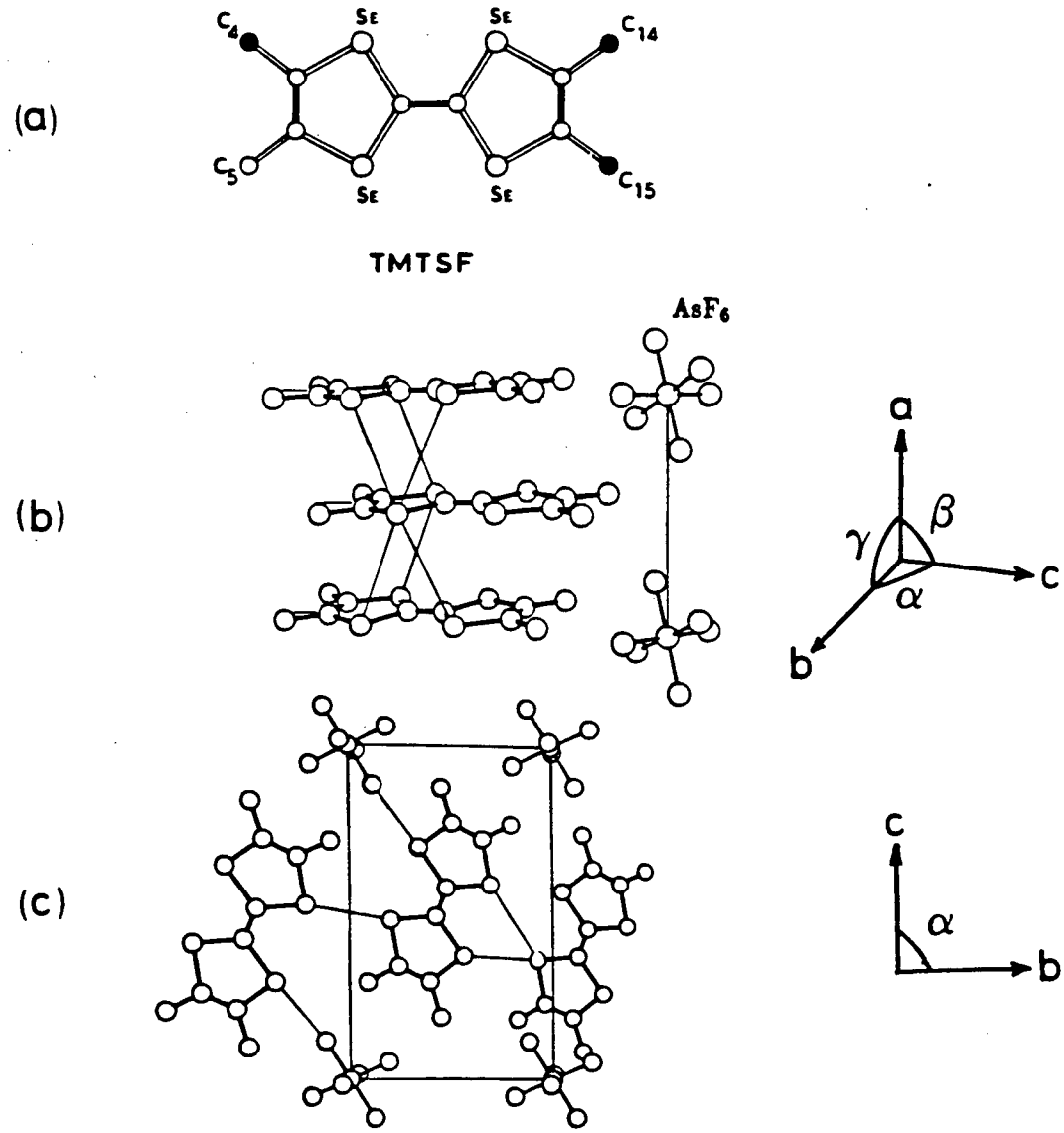

Figure 1-2 The structure of $(TMTSF)_2X$. (a) The TMTSF molecule. The methyl groups strongly involved in the definition of the anion cavity are indicated by the solid shading[13]. (b) Molecular stacking in $(TMTSF)_2AsF_6$. This shows the side view of the chain and the set of crystallographic coordinates[14]. (c) View of $(TMTSF)_2AsF_6$ down the **a**-axis showing the anion lattice[14]. Typical dimensions for the unit cell of $(TMTSF)_2AsF_6$ are $a = 7.277(2)$ Å, $b = 7.711(1)$ Å, $c = 13.651(2)$ Å, $\alpha = 83.16(1)°$, $\beta = 86.00(2)°$, $\gamma = 71.27(2)°$[14].

defined lattice and sit in the cavities left by the TMTSF molecules. The **c**-axis lies along the anion lattice direction that is almost normal to the **ab**-plane.

Other sets of axes that are routinely used are the orthogonal set (**a**, **b**′ and **c**′) and the set of principal magnetic axes (**a***, **b*** and **c***). In the orthogonal set **b**′ is orthogonal to **a** and in the **ab** plane, and **c**′ completes the set. The principal magnetic axes are those crystal directions along which the magnetic susceptability is greatest. In fact **a** and **a*** are the same, but **b*** and **c*** are close to, but not the same as **b** and **c** respectivley.

The TMTSF molecules stack almost perpendicular to the **a**-axis, deviating from perpendicularity by $\sim 1.1°$[15]. The stack units repeat by inversion with overlap displacements alternating along the **a**-axis.

The value of the lattice parameters for the unit cell will vary depending on the anion substitution[13–19]. There are two TMTSF molecules per unit cell, and there is a transfer of one electron from two TMTSF molecules to one anion giving a half filled band if we take **a** to be two molecular distances. Conduction along the TMTSF stacks is by normal band conduction. Unlike most other charge tranfer salts the anion stacks do not have overlapping atomic orbitals and thus conduction electrons do not move up and down the anion stacks. The anions are important in controlling lattice parameters and play a major role in the bandfilling.

1.5 Electronic Band Structure of $(TMTSF)_2X$

The effect that charge-density waves can have on the band structure has been examined, but the actual band structure of the $(TMTSF)_2X$ compounds has not yet been discussed. A tight-binding calculation for a unified single-particle model has been developed by Grant at IBM[20] to calculate the band structure of these compounds. If one were to consider all of the valence electrons in this method, it would involve solving a secular equation for 76 bands. The calculations are simplified considerably if some simple assumptions are made about the $(TMTSF)_2X$

salts, the most important of which being that only the highest occupied molecular orbital (HOMO) will be relevent to transport in the solid. Immediately we have reduced the number of bands to just two. Rather than labor through Grant's developement of the problem, we will jump directly to his results.

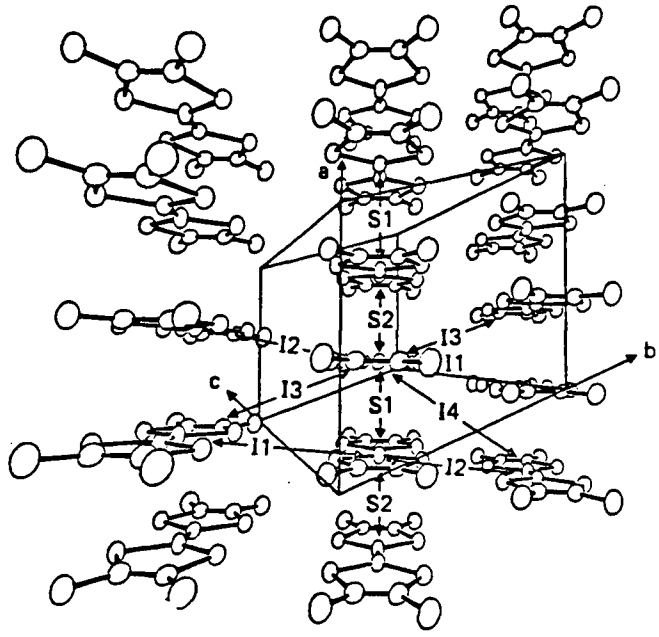

Figure 1-3 Perspective view of the $(TMTSF)_2X$ crystal structure showing the crystallographic axes **a**, **b** and **c**. The lables I1 → I4 refer to the interstack interactions, and S1 and S2 to the chain interactions that Grant uses in his calculations[20].

The crystal structure Grant uses in his calculations is shown in Fig. 1–3. Along with the crystallographic axes, there are also the labels I1 → I4, S1 and S2. The labels correspond to interstack and chain interactions, with the chain interactions being treated as distinct due to the dimerization of the stack.

The high temperature band structure and Fermi contour for $(TMTSF)_2AsF_6$ are shown in Fig. 1–4. The band structure shown here is representative of basically all the $(TMTSF)_2X$ compounds. The model is solved in two-dimensions because

the anisotropy is basically two-dimensional; the difference between the **b**- and **c**-axis being minor with respect to the **a**- and **b**-axis.

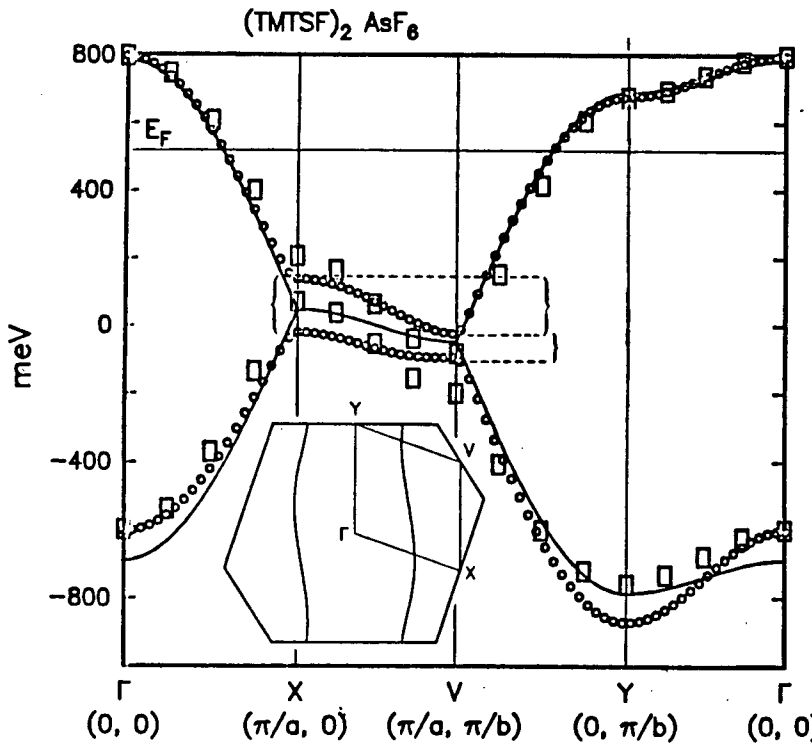

Figure 1-4 The high temperature band structure and Fermi contour in the first Brillouin zone of the reciprocal lattice for $(TMTSF)_2AsF_6$[20].

If one were just to consider a one-dimensional conductor along the highly conducting **a**-axis, then this would correspond to the electronic band structure along the $\Gamma \rightarrow X$ path. The location of the ε_F below the top of the band, and the absence of any gap indicates that the band is not closed and that conduction by valence electrons is possible. This is just the sort of band structure that one expects from a quasi-one-dimensional system.

The formation of a charge-density wave at low temperatures can change the lattice parameters and alter the reciprocal space and the shape of the first Brillouin zone thus changing the band structure of the system. Such a change in the

lattice parameter is referred to as a broken symmetry. The band structures shown in Figs. 1–5(a),(b) and (c) are for the most highly commensurate two-dimensional broken symmetries. Besides the formation of a CDW, lattice parameters may also be changed by an anion-ordering transition which alters the size of the unit cell. The anion-ordering transition arises only in those Bechgaard salts that have non-symmetric (*i.e.* tetrahedral, planar, etc.) anions. Diffuse X-ray studies show no $2k_F$ scattering indicating that the transition is not due to a charge-density wave[21,22]. Single-crystal neutron-diffraction experiments establish that the salts with non-symmetyric anions undergo crystallographic phase transitions at low temperatures due to anion ordering[23]. These anions have different orientations in the anion cavity which are non-degenerate. The octahedral anions do not display anion-ordering transitions because they are symmetric; all the allowed anion orientations are the same. At high temperatures the non-symmetric anions are randomly oriented and the anion lattice shows no long-order due to the presence of a crystallographic inversion center[24]. Below the anion-ordering temperature, T_{AO}, the anions order along preferential directions. The anion sites do not interact directly, but rather through the cation/anion Se–X interaction for X=ReO_4, ClO_4 and BF_4[23] the CH_3–X interaction for X=NO_3[19]. The strength of these interactions is thought to determine how the anions will order. In $(TMTSF)_2ReO_4$ the anions order in an alternating sequence along the **a**-, **b**- and **c**-directions, whereas in $(TMTSF)_2ClO_4$ the anions order only along the **b**-direction. The formation of long-range order in the anion lattice along any one of these crystal directions creates a superlattice structure which changes the size of the unit cell. The anion-ordering transitions that have been observed in these compounds[23] show that these transitions are commensurate with the existing lattice parameters, and double the size of the unit cell in the direction which the anions order. The three cases that are considered are: (a) doubling of the lattice parameter along the chain direction only, corresponding to a modulation wave-vector of $\mathbf{Q} = (1/2, 0)$; (b) doubling of the lattice parameters in both the chain

and transverse directions, resulting in a modulation wave-vector of $\mathbf{Q} = (1/2, 1/2)$ and (c) a doubling of the lattice parameter in the transverse direction only, resulting in a modulation wave-vector of $\mathbf{Q} = (0, 1/2)$. In each case the figures show the change in the shape of the first Brillouin zone in the reciprocal lattice.

A doubling of the lattice parameter along the stack direction occurs in the NO_3 compound at $\sim$ 41 K due to an anion-ordering transition[28], resulting in a $2a \times b \times c$ unit cell with a modulation wave vector of $(\pi/a, 0, 0)$[36], or a $\mathbf{q} = (1/2, 0)$ broken symmetry in Grant's model. An anomaly in the conductivity is observed in the NO_3 compound at 41 K, however, unlike other Bechgaard salts which undergo AO transitions and experience a decrease in the conductivity, the NO_3 is a better conductor in the $2a \times b \times c$ superlattice. As the temperature is lowered below T_{AO} the conductivity continues to increase in this compound until 12 K, where a metal-insulator (MI) transition occurs[11]. The differences in the crystal structures of $(TMTSF)_2NO_3$ at 41 K and 12 K are minor. It is thought that the change in the magnitude and the anisotropy of the cation/cation and cation/anion interactions at 12 K may be responsible for the MI transiton in this compound[19]. In the model a gap of 2Δ opens near the Fermi energy resulting in either a semimetal or an indirect gap semiconductor, depending on the size of Δ. The Fermi contour is a line that joins all the points in the first Brillouin zone where the electron energy is equal to the Fermi energy. The creation of a gap is represented by a break in the Fermi contour, as shown in Fig. 1–5(a). In Fig. 1–5(a) the Fermi energy (shown by a line) is tangent to the valence band at X and to the conduction band at V resulting in a zero-gap semiconductor. Increasing the size of Δ shifts ε_F above the valence band leaving the conduction band empty and resulting in a semiconductor. In view of Grant's model and the behavior of the NO_3 compound, it is possible that at 41 K a zero-gap seimconductor forms due to the $\mathbf{Q} = (1/2, 0)$ broken symmetry. At 12 K, the size of the energy gap may increase resulting in a semiconductor and explaining sudden decrease in the conductivity.

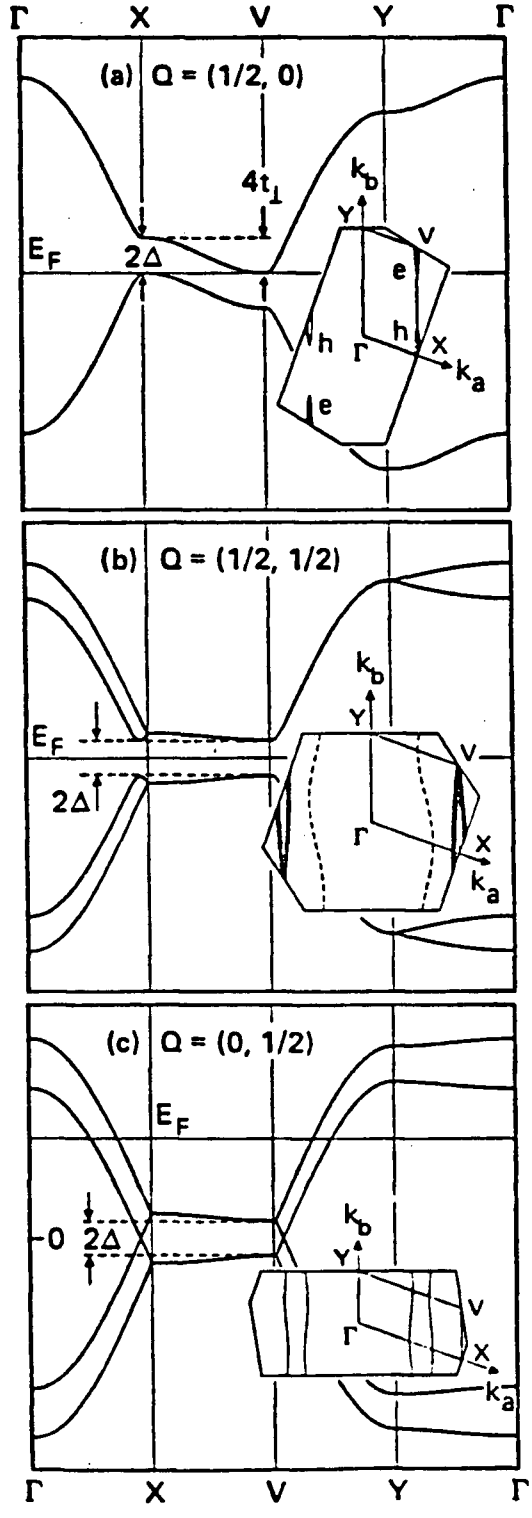

Figure 1-5 Model band structures for the three most highly commensurate two-dimensional broken symmetries: (a) $\mathbf{Q} = (1/2, 0)$; (b) $\mathbf{Q} = (1/2, 1/2)$; (c) $\mathbf{Q} = (0, 1/2)$[20].

A doubling of the lattice parameter along both the stack and transverse directions occurs in $(TMTSF)_2BF_4$ at $\sim$ 38 K and in $(TMTSF)_2ReO_4$ at $\sim$ 180 K due to an anion-ordering transition resulting in a $2a \times 2b \times 2c$ unit cell[23]. This gives a modulation wave-vector of $(\pi/a, \pi/b, \pi/c)$[36] and corresponds to the $\mathbf{Q} = (1/2, 1/2)$ broken symmetry in Grant's model. From Fig. 1–5(b) a direct gap of 2Δ is created in the band structure. This can also be seen from the Fermi contour. This is the only symmetry that yields an insulator for every finite value of 2Δ, since ϵ_F is in the middle of the gap and thus the valence band is closed for any non-zero gap.

A doubling of the lattice parameter along the transverse direction occurs in $(TMTSF)_2ClO_4$ at $\sim$ 24 K due to an anion-ordering transition resulting in a $a \times 2b \times c$ unit cell and a modulation wave-vector of $(0, \pi/b, 0)$[23,36]. This corresponds to the $\mathbf{Q} = (0, 1/2)$ broken symmetry in the model. A gap 2Δ is introduced, but it is not near ϵ_F and the number of Fermi contours increases from two to four preserving the metallic ground state. This may explain why no anomaly in the conductivity of $(TMTSF)_2ClO_4$ is observed.

1.6 $(TMTSF)_2X$ Salts with Centrosymmetric Anions

The Bechgaard salts display a variety of interesting low temperature states. Despite having the same stoichiometry, the compounds having centrosymmetric anions have different physical properties than those with non-centrosymmetric anions.

The salts with the centrosymmetric anions (PF_6, AsF_6, SbF_6 and TaF_6) display electrical conductivities as large as 10^5 $(\Omega\,\mathrm{cm})^{-1}$ along the **a**-axis at $\sim$ 20 K. Some plots of d.c. resistivity versus temperature for some $(TMTSF)_2X$ compounds are shown in Fig. 1–6(a)[11]. The resistivity at 35 Ghz is also shown in Fig. 1–6(b)[11] for comparison. The superconductivity occurs in the centrosymmetric compounds under pressure. The first organic material discovered to exhibit superconductivity was $(TMTSF)_2PF_6$[12], which becomes a bulk superconductor at $T_c \sim 1$ K with the

application of $\geq$ 6.5 kbar of pressure (T_c is used to indicate the critical temperature at which the material becomes superconducting in three-dimensions). Evidence for type II superconductivity includes both zero resistance[12] and a partial Meissner effect[25,26]. Increasing the pressure decreases T_c[27]. Superconductivity has also been observed at $\sim$ 11 kbar in $(TMTSF)_2AsF_6$[28], $(TMTSF)_2SbF_6$[29] and $(TMTSF)_2TaF_6$[29].

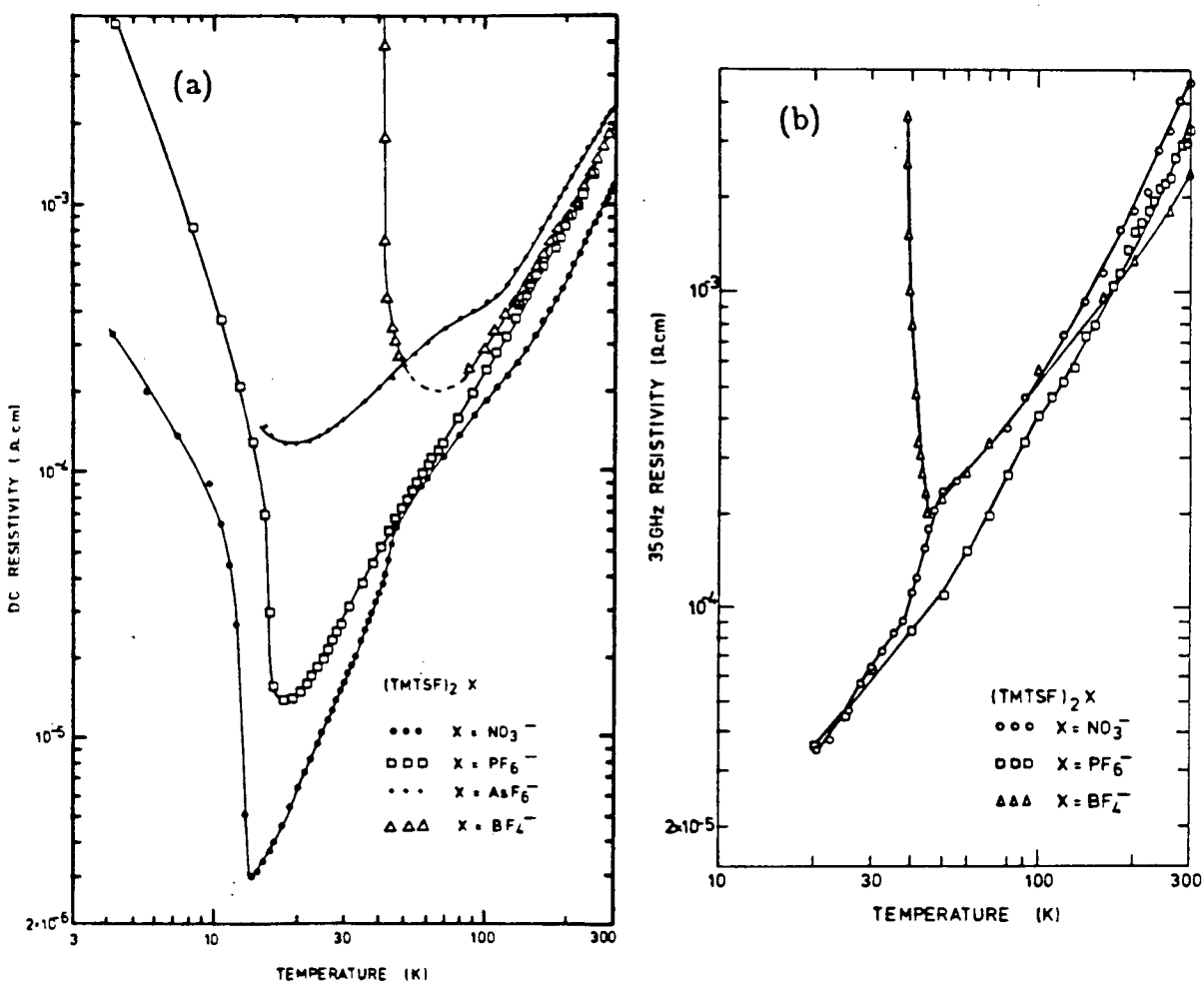

Figure 1-6 The (a) d.c. resistivity and (b) resistivity at 35 GHz versus temperature for some typical samples of of $(TMTSF)_2X$. Note the logarithmic temperature and resistivity scales[11].

The one-dimensional behavior of the superconducting state in these compounds has been shown using a Schottky electron-tunneling technique[30,31].

All of these salts undergo metal-insulator (MI) transitions at $\sim$ 12 K at ambient pressure. The absence of a $2k_F$ superlattice below the MI transition rules out a charge-density wave for the formation of an energy gap at the Fermi surface[21,22]. The disappearance of the ESR signal[32], the anisotropic lattice magnetic susceptibility below the transition[33], and a spin-flop transition at 4.5 kG[34] using the static magnetic susceptability measurements indicate the occurence of an Overhauser antiferromagnetic transition to a spin-density-wave (SDW) state, making these materials itinerant antiferromagnets. The nuclear spin-lattice relaxation rate of enriched ^{13}C nuclei in $(TMTSF)_2PF_6$ indicate that the spin-density-wave state interacts weakly with the carbon sites in the crystal[35]. This transition marks a dimensionality crossover from two- or three-dimensional behavior at low temperatures to one-dimensional behavior at higher temperatures[35]. The SDW state is interesting because a Peierls instability is more common among low-dimensional metals. The anisotropy of the susceptibility is consistent with expectations of a simple antiferromagnet with the easy, intermediate and hard axes close to the $\mathbf{b}^*$, $\mathbf{a}$ and $\mathbf{c}^*$ directions[33]. In the SDW state the periodicity of the spin structure along the chain direction is given by the Fermi wave-vector, leading to a doubling of the unit cell, *i.e.* there are now four TMTSF molecules in the unit cell[36]. The band structure calculations by Grant indicate that the SDW antiferromagnetic state may possess the $\mathbf{Q} = (1/2, 1/2)$ broken symmetry, which results in an insulator. Confirmation of a doubling of the transverse lattice constants in the centrosymmetric compounds must await a polarized neutron study[36]. A phase diagram for the $(TMTSF)_2AsF_6$ salt is shown in Fig. 1–7. This diagram may be generalized for all of the compounds with centrosymmetric anions. For a constant pressure ($\sim$ 10 kbar), it is possible to enter the insulating SDW state for some critical temperature, and then to enter

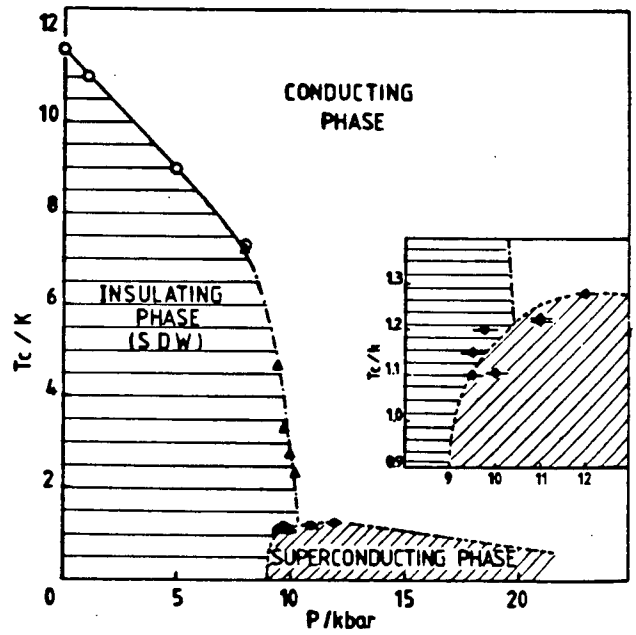

Figure 1-7 The phase diagram of $(TMTSF)_2AsF_6$ under pressure ($P \leq 8$ kbar open dots, $P > 8$ kbar open triangles). T_c is the critical temperature (for some pressure P) for either a SDW or SC transition. The inset shows the re-entrance of the superconductivity at $\sim$ 10 kbar from the insulating SDW state[87].

the superconducting state. This striking feature is referred to as the re-entrant superconductivity.

The d.c. conductivity in $(TMTSF)_2PF_6$ is highly anisotropic ($\mathbf{a} : \mathbf{b} : \mathbf{c} \simeq 10^5 : 400 : 1$) and increases beyond $10^5\ (\Omega\,\mathrm{cm})^{-1}$ upon cooling to $\sim T_{MI}$, and then decreases rapidly with the onset of the SDW state[88]. These values of $\sigma_{\|}$ are about ten times larger than the maximum conductivity observable in other charge transfer compounds at low temperatures. Given the electron density of 10^{22} charges cm^{-3}, a mobility of $\approx 2 \times 10^3\ \mathrm{cm}^2\,\mathrm{V}^{-1}\,\mathrm{s}^{-1}$ is derived at 1.3 K (for $\sigma_{\|} = 5 \times 10^5\ (\Omega\,\mathrm{cm})^{-1}$) leading to an approximate mean-free path of 700 intermolecular spacings along the **a**-axis. The conductivity of $(TMTSF)_2PF_6$ in the SDW state increases at frequencies above $\sim$ 1 GHz[89], and is attributed to the

SDW response to the a.c. field[40]. The SC state (type II) in $(TMTSF)_2PF_6$ and $(TMTSF)_2AsF_6$ is destroyed by a small magnetic field. The critical fields are also highly anisotropoic, with $H_{c2}^{c^*} = 200$ G along the **c**-axis and $H_{c2}^{b'} = 2$ kG along the **b**-axis for $(TMTSF)_2PF_6$, and $H_{c2}^{c^*} = 1.4$ kG along the **c**-axis, and $H_{c2}^{b'} = 20$ kG along the **b**-axis for $(TMTSF)_2AsF_6$.[41]. Some of the properties of the $(TMTSF)_2X$ salts are shown in Table I–I.

1.7 $(TMTSF)_2X$ Salts with Non-centrosymmetric Anions

The non-centrosymmetric anions include BF_4, ReO_4, ClO_4, FSO_3 and NO_3. Superconductivity is observed in $(TMTSF)_2ReO_4$ at $\sim$ 1.3 K under $\sim$ 9 kbar of pressure[42]. Efforts to eliminate the need for pressure led to the substitution of very small anions in order to decrease the interstack distance. When this was done with the ClO_4 anion in 1980, the resulting salt became superconducting at $\sim$ 1.2 K at ambient pressure[43,44]. Thus $(TMTSF)_2ClO_4$ was the first ambient pressure organic superconductor! The superconductivity in $(TMTSF)_2ClO_4$ was confirmed by the observation of Meissner signals[45] and specific heat measurements using an a.c. calorimetric technique[46], indicating a type II character. The molar specific heat displays a very large anomaly around 1.2 K. Above $T^2 = 1.2$ K^2 the specific heat obeys the classical relation $C/T = \gamma + \beta T^2$, where $\beta = 11.4$ mJ mol^{-1} K^{-4} and $\gamma = 10.5$ mJ mol^{-1} K^{-2}. The C/T versus T plot of the electronic contribution allows a very accurate determination of the critical temperature, namely $T_c = 1.22$ K.

These salts are different than those with centrosymmetric anions in that they undergo metal-insulator transitions[47], but at much higher temperatures. Neutron-diffraction[38] and X-ray diffuse scattering[21,22] studies have shown that this transition is due to an ordering of the anion lattice, thus forming a superlattice structure. The compounds $(TMTSF)_2BF_4$ and $(TMTSF)_2ReO_4$ have MI transitions at 38 K and 180 K respectively, and below these temperatures the anions alternate in orientation along all three lattice directions, thus the unit cell changes from $a \times b \times c$ to

Table I–I[a,b,c]

Properties of some $(TMTSF)_2X$ salts

Anion	Anion Symmetry	T_{MI} (°K)	Transition	T_c (°K)	P_c (kbar)
PF_6	Octahedral	12	SDW	1.4	8.5
AsF_6	Octahedral	12	SDW	1.4	9.5
SbF_6	Octahedral	17	SDW	0.38	10.5
TaF_6	Octahedral	11	SDW	1.3	11
BF_4	Tetrahedral	39	AO	–	–
ClO_4	Tetrahedral	24	AO	1.2	atm
		3.5	SDW	–	–
ReO_4	Tetrahedral	180	AO	2	5
FSO_3	Asymmetric	87	AO	2	5
NO_3	Planar	40	AO	–	–
		12	?	–	–

T_{MI} The temperature of the SDW or AO transition.

SDW Spin-density wave transition.

AO Anion-ordering transiton.

T_c Temperature at which the salt becomes a superconductor.

P_c Minimum pressure for superconductivity to occur.

[a] Ref. 22

[b] Ref. 23

[c] Ref. 36

$2a \times 2b \times 2c$. This corresponds to a modulation wave-vector $(\pi/a, \pi/b, \pi/c)$, corresponding to the $\mathbf{Q} = (1/2, 1/2)$ broken symmetry in the electronic band structure model. It is apparent that the gap created by the AO transition is responsible for a semiconducting state. While $(TMTSF)_2ClO_4$ has an anion-ordering transition at 24 K, the anions only alternate along the **b**-axis, thus the unit cell changes from

$a \times b \times c$ to $a \times 2b \times c$[23]. With a modulation wave-vector of $(0, \pi/b, 0)$, this corresponds to the $\mathbf{Q} = (0, 1/2)$ broken symmetry in the electronic band structure model. The fact that $(TMTSF)_2ClO_4$ remains metallic below the AO transition agrees with the model.

If $(TMTSF)_2ClO_4$ is cooled rapidly below 50 K ($\sim$ 25 K/min – quenched), the anion disorder is frozen in and a magnetic SDW state is observed below $\sim$ 3.5 K[47,48], with no SC transition. This effect is reversible, and when the sample is cooled slowly below 50 K, ($\sim$ 1 K/min – relaxed), then the usual anion ordering transition is observed at 24 K and an SC state at $\sim$ 1.4 K.

The SC state in $(TMTSF)_2ClO_4$ is very sensitive to the magnetic field. The critical magnetic fields for a type II superconductor, extrapolated to $T = 0$ K, are highly anisotropic, with $H_{c2}^{c^*} \sim 150$ G and $H_{c2}^{b'} \sim 10$ kG[41,50]. Some of the properties of the non-centrosymmetric salts are included in Table I-I.

1.8 Far-Infrared Optical Properties

The far-infrared region of the optical spectrum, 10–1000 cm^{-1} (1–120 meV), is important because many of the physical properties displayed by quasi-one-dimensional conductors, such as spin-density waves, charge-density waves, semiconducting and superconducting transitions, low-lying lattice modes and free-carrier absorption all have activation energies in this region.

The far-infrared optical properties of the $(TMTSF)_2X$ compounds have been studied by a number of groups, including Challener *et al.*, Eldridge *et al.*, Tanner *et al.* and Timusk *et al.* Single-crystal reflectance measurements have been performed on ClO_4[51,52,53,54], PF_6[54,55], SbF_6[56,57] and AsF_6[57,58] compounds, however, there is disagreement between the results obtained for the all of the compounds. The difficulty arises from the small crystal sizes which necessitates the use of crystal mosaics below 1000 cm^{-1} when measuring the reflectivity. The problem with this method is that it is almost impossible to align the crystals properly. The use of

a mosaic also introduces diffraction effects into the reflectance spectra, making it difficult to obtain absolute values of reflectance; especially when R is very close to 100% as it is for these compounds.

A completely different method of obtaining R was used by Eldridge, Bates and Bates. It involves a bolometric technique whereby that part of the incident radiation which is absorbed by a single crystal at liquid-helium temperatures, heats the crystal by a small amount. If the crystal is semiconducting then this temperature rise produces a drop in the electrical resistance which can be measured and is proportional to $1-R$ since everything not reflected is absorbed and none is transmitted. (The absorption coefficient of these crystals is very high). This "simple-bolometric" technique has been used to measure R for TTF-TCNQ[59,60]. The $(TMTSF)_2X$ salts at low temperature, even though they may be semiconducting, have conductivities too high for a good bolometer, so that "composite-bolometers" have been made instead. A small germanium bolometer is glued to the rear face of the single crystal and the temperature rise measured in this way. Once again the signal is proportional to $1-R$, which is exactly what one wishes when R is so close to unity. The results for $(TMTSF)_2PF_6$ obtained by this method[54] and the mosaic reflectance method[55] are shown in Figure 1–8.

The incident radiation may be polarized for either $\mathbf{E} \parallel \mathbf{a}$ or $\mathbf{E} \perp \mathbf{a}$ to give information about the electronic properties along the parallel and transverse axes. By sampling the reflectivity of a crystal over a very large interval (from $\bar{\nu} \sim 0$ to $\bar{\nu} \rightarrow \infty$), then a Kramers-Kronig[61,62] analysis may be used to determine the optical properties of the material, such as the electrical conductivity.

The single-crystal reflectance spectra of $(TMTSF)_2PF_6$ for $\mathbf{E} \parallel \mathbf{a}$, shown in Fig. 1–8(a)[55] and (b)[54], illustrates the different experimental results for this compound. The electrical conductivity is calculated using a Kramers-Kronig analysis of the reflectivity spectra in Figs. 1–8(a) and (b), and is shown in Figs. 1–8(c)[55] and (d)[54] respectively. The calculated conductivities are quite different, and more study

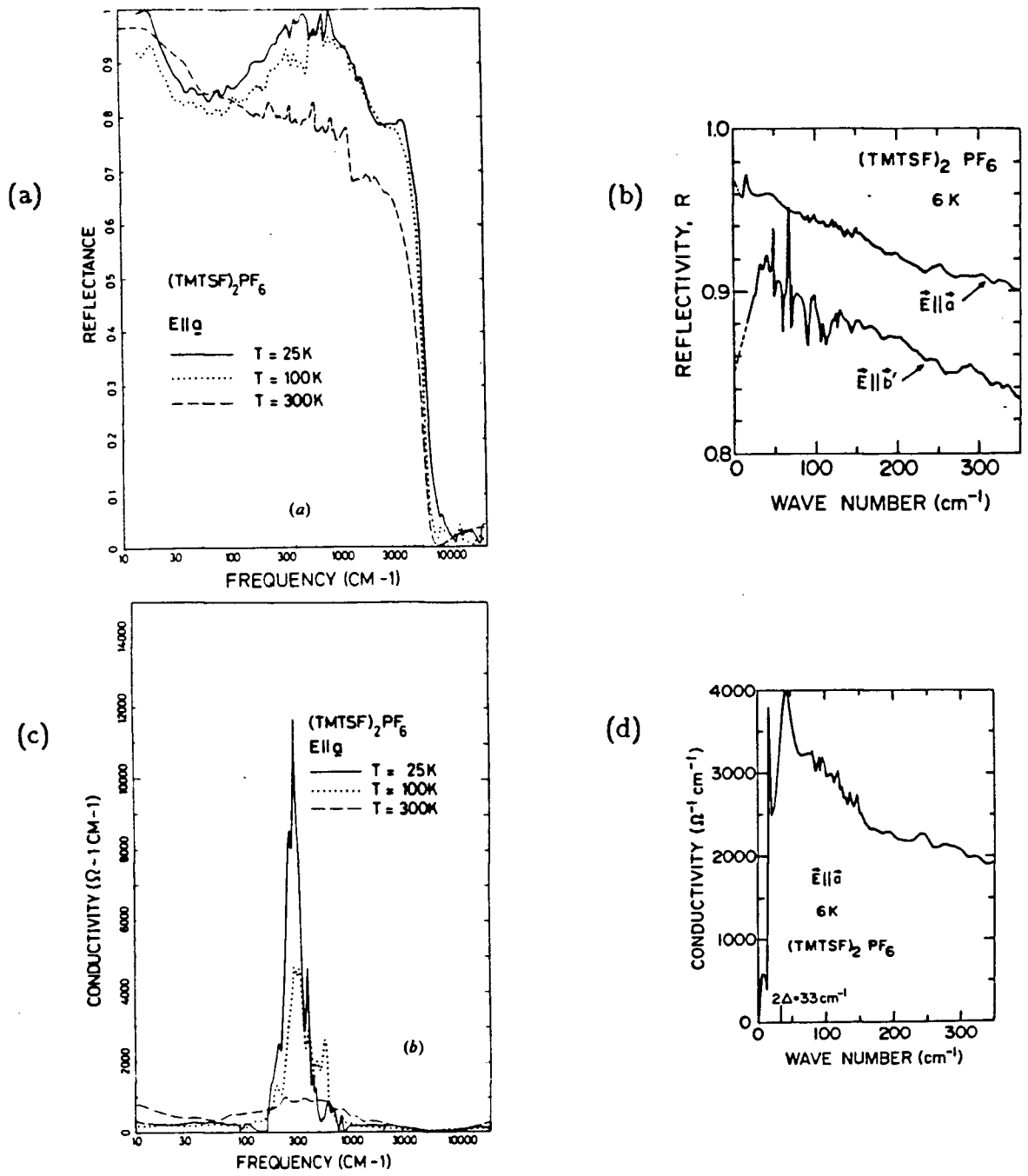

Figure 1-8 The single-crystal reflectance of $(TMTSF)_2PF_6$ for **E** || **a** at various temperatures (a) by Tanner *et al.*[55] and (b) Eldridge *et al.*[54] The conductivity calculated from the reflectivity in (a) is shown in (c)[55], and the conductivity calculated from (b) is shown in (d)[54]. The experimental results are not in agreement.

is needed to resolve this issue. One thing the conductivities do emphasize is the low far-infrared conductivity above the SDW transition ($\sim 300\ (\Omega\,\mathrm{cm})^{-1}$) compared to the large d.c. conductivity ($> 10^4\ (\Omega\,\mathrm{cm})^{-1}$)[11]. Below the SDW transition at ~ 6 K, the far-infrared conductivity agrees with the d.c. conductivity.

The measurements done in this thesis are with powders rather than single crystals, and we are concerned with the 20-250 cm^{-1} region. The main disadvantage of powder samples is that they are not oriented along any one direction, thus the information they give is for all polarizations rather than just one. The powder spectra of $(TMTSF)_2PF_6$ and $(TMTSF)_2ReO_4$ has been measured by Bozio and Pecile *et al.* in the mid-infrared region[63]. Meneghetti *et al.* have made an extensive vibrational analysis of TMTSF, and its radical cation, $TMTSF^+$[64]. No powder measurements have been made below 250 cm^{-1}. The results from the powder measurements that have been made for $(TMTSF)_2X$, X=PF_6, AsF_6, SbF_6, BF_4, ClO_4 and ReO_4 will be compared with the vibrational studies.

1.9 Fluctuating Superconductivity

The idea of fluctuating superconductivity (FSC) in quasi-one-dimensional compounds, such as the $(TMTSF)_2X$ salts, was first advanced by Jérome *et al.*, and refined by Schultz[65]. The one-dimensional superconductor can be considered an array of stacks of organic molecules whose average dimensions amount to a few Angström. By introducing a weak interchain coupling $t_\perp$, where $t_\perp \ll t_\parallel$, there is a finite probability that an electron will jump from one stack to another, *i.e.* transverse electron motion is possible. In the presence of such coupling fluctuations long-range three-dimensional order is possible at finite temperature. To investigate the behavior of these fluctuations more carefully, the Ginzburg-Landau theory is employed. In this phenomenalogical description, the free energy of the system is expanded in terms of an order parameter (the gap energy), which is allowed to vary slowly and is treated as a classical variable. By demanding that the free energy

be minimized over all configurations by the use of a self-consistent field approximation, the properties of the system may be obtained. One of the consequences of the Ginzburg-Landau theory is that because the free energy contains high order terms that are usually ignored in simpler models (such as mean-field approximation), the correlation lengths in the stack and transverse directions ($\xi_{\|}$ and $\xi_{\perp}$) are allowed to fluctuate. The SC transition temperature also exhibits fluctuations in this model. Fluctuating superconductivity is normally discussed in the temperature regime $T_3 < T < T_1$ where below T_3 three-dimensional behavior dominates and below T_1 one-dimensional properties characterize the system. The bulk superconducting transition temperature $T_c < T_3$. FSC effects may be possible at temperatures up to 40 K. There is also a pairing of electrons in FSC. Normal electrons form virtual Cooper pairs above the Fermi surface in time τ_N. They decay back to the normal state in time τ_S. Because of the formation of virtual Cooper pairs, there is a decrease in the density of states at the Fermi level given by $[N(\varepsilon_F) - N_0]/N_0 = \tau_N/\tau_S$. This reduction, but not complete removal of the density of states is called a pseudo-gap. Since FSC is thought to occur below T_1, this would imply a large pseudo-gap.

There is some evidence to support the premise of a fluctuating superconductivity in the $(TMTSF)_2X$ salts. The longitudnal conductivity exceeds 10^4 $(\Omega\,cm)^{-1}$ at 4.2 K for $(TMTSF)_2PF_6$, $(TMTSF)_2AsF_6$, etc. under pressure[11] and for the ClO_4 compound at ambient pressure[43]. These conductivities are larger than any other organic material by an order of magnitude. This is considered to be evidence for a new form of electrical transport (FSC). In addition, the temperature dependence of the electrical resistivity is still large below 4.2 K, in a temperature domain where the resistivity of all three-dimensional metallic conductors with single-particle transport is limited by residual impurities[16,36,66]. The large magnetoresistance in the $(TMTSF)_2X$ salts may be explained by the destruction of fluctuating Cooper pairs. The extreme sensitivity of the conductivity to radiation-induced defects is difficult to explain in terms of single-particle transport, but if the

defects are magnetic then they can destroy the fluctuating Cooper pairs by acting as orbital pair-breakers[16,36,66].

The large drop in the thermal conductivity below $\sim$ 50 K can be restored by a magnetic field applied parallel to the **a**-axis. Carriers that are involved in FSC do not contribute to the thermal conductivity, but if the fluctuating Cooper pairs are destroyed by the magnetic field, then carriers are freed and the thermal conductivity will be restored, in agreement with experiment[36,65,67]. The conductivity at 4.2 K may be explained for single-particle transport only if the mean-free path of the carriers is $\sim$ 700 intermolecular spacings along the **a**-axis. This would require samples of high purity, which is unlikely[66].

Electron quantum tunnelling is by far the most sensitive probe of the density of states. The transition probability of single electrons, which obey Fermi statistics, to tunnel between two metal electrodes seperated by a thin insulating barrier, is proportional to the density of final states. Measurement of tunnelling resistance can thus be used to determine changes in the density of states of quasiparticles in a one-dimensional conductor above T_c, which indicate the development of the pseudo-gap below T_1. Such measurments have been sucessfully made with $(TMTSF)_2PF_6$ using the Schottky barrier geometry, namely studying the tunnel resistance of quasiparticles between a single crystal and an evaporated N/GaSb semiconductor through the intrinsic potential existing at the interface. The zero-tunnel resistance measurements shows a psuedo-gap in the conductivity at $\sim$ 6.3 meV ($\sim$ 50 cm^{-1}). This gap is much too large to be associated with the 1 K SC gap, and in addition is measured at temperatures well above 1 K. It cannot be associated with the magnetic SDW, because a magnetic field tends to destroy the measured gap in the tunnelling experiment rather than stabalize it. Also, if a SDW pseudo-gap exists at $\sim$ 30 K, the resistivity should begin to increase with decreasing temperature

as the SDW state becomes more stable, something that is not seen in the experiments. These results would, however, be consistent with the theory of fluctuating superconductivity[29,30,36,66].

Not all experimental data is in agreement with the theory of a FSC. Green *et al.* think the in general the interchain coupling is much stronger than the weak interchain coupling used by Schultz in the Ginzburg-Landau formalism[41]. The measured anisotropy of the SC critical magnetic field in $(TMTSF)_2ClO_4$ is 28:15:1 for H^a_{c2}:$H^{b'}_{c2}$:$H^{c^*}_{c2}$. The Ginzburg-Landau theory predicts 200:20:1 if the same mechanism is involved in limiting H_c in all three directions. The critical field is much smaller than expected, and therefore it must be limited by something other than orbital pair-breaking, such as the Pauli limiting effect due to spin pair-breaking. The Pauli critical magnetic field is directly related to T_c and the size of the SC energy gap. The measured H^a_{c2} is in good agreement with the 1 K transition temperature. The large gap measured in the tunnelling experiment, however, implies a Pauli limit which is 20 times larger than the measured H^a_{c2} and therefore the tunnel gap must not be related to the superconductivity.

The thermopower drops toward zero, with decreasing temperature, but then becomes negative at 7.5 K[67]. The change in sign of the thermopower cannot be explained by superconducting fluctuations, and demonstrates that a different transport mechanism is giving rise to the temperature dependence.

If the scattering rate at the Fermi surface is anisotropic, then the large magnetoresistance can be explained by the single-particle transport model. The d.c. conductivity is principally due to carriers in regions of the Fermi surface with long lifetimes, but in a magnetic field these carriers are swept into other regions with a high scattering rate and the conductivity is reduced. An increased scattering rate caused by radiation induced defects is also sufficient to explain the reduced conductivity for a single-particle transport system[68].

The pseudo-gap measured in the infrared data for $(TMTSF)_2PF_6$[55], is at $\sim 200\ cm^{-1}$ (25 meV), and not at $\sim 50\ cm^{-1}$. It is much too large to be associated with the gap measured in the tunnelling experiment (3–4 meV). The pseudo-gap in the infrared data also exists up to 300 K, well above the temperaures at which superconducting fluctuations are thought to be important. Furthermore, Green argues that off stoichiometric films of GaSb are superconducting with T_c as high as 8 K[69]. It is possible that such Ga or Sb superconducting phases could be formed on the $(TMTSF)_2PF_6$ surface during the tunnel junction preparation. The transition temperature T_c also decreases as the pressure is increased[27]. The simplest explanation is that the pressure decreases the distance between the stacks allowing the initial onset of superconductivity, however in this view increasing the pressure should then increase T_c even more. The fact that just the opposite happens seems to contradict FSC.

The issue of whether FSC is viable or not has not yet been resolved, and will continue to be a source of debate.

CHAPTER 2

EXPERIMENTAL TECHNIQUES

2.1 Sample Preparation

Samples of protonated (TMTSF-h_{12})$_2$X and deuterated (TMTSF-d_{12})$_2$X, for X=PF_6, AsF_6, SbF_6, BF_4, ClO_4 and ReO_4, were prepared by electrocrystallization using a modified H-cell[70] by Gordon Bates of the Chemistry Department at the University of British Columbia. The reaction was typically carried out under a nitrogen atmosphere in anhydrous dichloromethane (5×10^{-2} M in electrolyte, 4×10^{-3} M in TMTSF at the anode) at a constant current of 2.2 or 4.0 μA. The electrolysis was discontinued at $\sim$ 50% conversion. The R_4NX electrolytes were purified by recrystallization prior to use. Initially, the TMTSF was prepared in our laboratory. However, comercially available[71] material is now routinely used. The TMTSF-d_{12} was prepared from deuterated 3-methanesulphonyl-2-butanone (from 2,3-butandione-d_6) using a modification of the literature procedures[72]. Deuterium incorporation levels in the intermediate products were esitmated by proton magnetic resonance and/or high resolution mass spectrometry. The deuterium content of 4,5-dimethyl-1, 3-diselenole-2-selone, the immeadiate precursor to TMTSF-d_{12} ($\sim$ 90%) is assumed to be that of the 2-selone precursor.

The crystals were ground up in Nujol mineral oil with a mortar and pestle and the resulting mull was transferred to a wedged piece of TPX. Photomicrographs of the powder samples were made with a high power microscope at 400×. The small

particles in the powder had a typical diameter of $\leq 1\mu$ and the larger particles had a typical diameter of $\leq 3\mu$.

2.2 Michelson Interferometer

The far infrared measurements were made on a modified Beckman/RIIC FS-720 Fourier spectrophotometer. The polarizing Martin-Puplett mode[73] was used for measurements in the 20–125 cm^{-1} region. This method employs a beam-splitter oriented at 45° to the roof-top mirrors and two fixed tungsten wire beam-splitters (with a wire thickness of 10 μm and a separation of 25 μm), one before and one after the beam-splitter. The main advantage of this type of interferometer is its excellent high constant transmission characteristics below about 150 cm^{-1}, unlike a mylar beam splitter which has a sinusoidal response. For measurements in the 100–350 cm^{-1} range a 25G (6.25 μm) mylar beam splitter was used. For measurements in the 100–750 cm^{-1} range a polycarbonate beam splitter was used. A Beckman/RIIC IR-7L d.c. mecury arc lamp was used as a source. The optical system is shown in Fig. 2–1.

The interferometer has a stepping mirror which is driven by a Superior Electronic SLO-SYN MO61-FC08 synchronous/stepping motor which is controlled by a modified Beckman/RIIC FS-MC1 step control. At each discrete position the preamplified signal from the bolometer was sent to another Princeton Applied Research 116 Preamplifier and then to a P.A.R. 124A Lock-In Amplifier. The reference signal of 70 Hz was provided by a phototransistor and diode on the chopper assembly. The signal output was then sent to a true integrator and integrated for a selected time interval (typically one second) after a chosen delay. The delay time allows the mirror vibrations to damp out improving the signal to noise ratio. This feature is only used in cases where the signal is extremely small, and the detector is very sensitive to vibrations. The integrated value is given to a 12 bit ADC, and the binary number is sent serially via RS-232C line to a PDP-11/23 PLUS computer

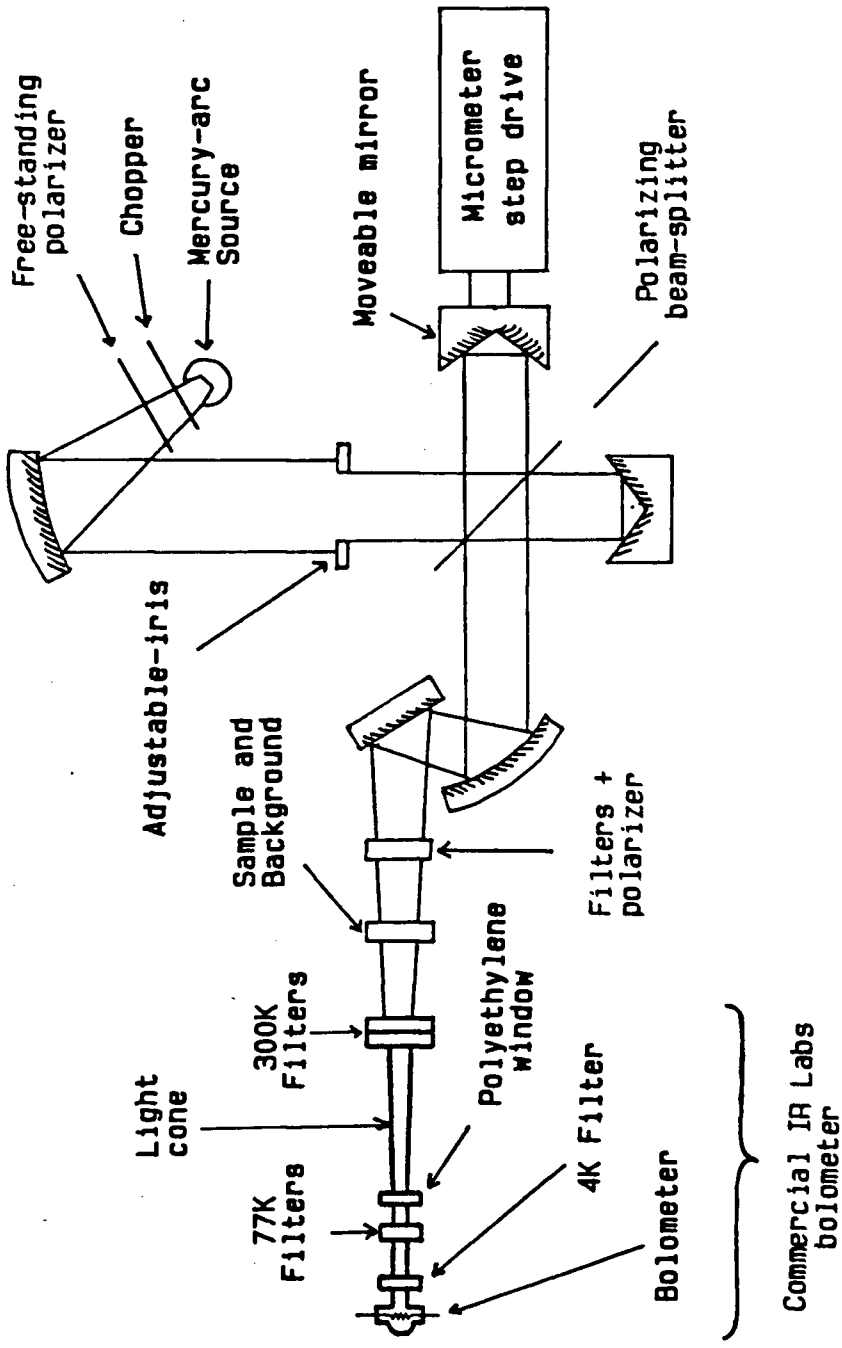

Figure 2-1 A shcematic of the Beckman/RIIC FS-720 spectrophotometer, with the tail of the Janis dewar. In the 100–750 cm^{-1} range the cold filters and the bolometer are are replaced by a Golay detector.

where it is written by a data acquistion program onto a RL02 removable hard disk. The sample-and-hold from the integrator is sent to a Heath SR 206 Dual pen chart recorder so that the interferogram is drawn out as it is measured. The detection and recording electronics are shown in Fig. 2–2.

A cryotrapped Varian VHS 4 diffusion pump evacuates the spectrometer chamber directly under the beam-splitter at a rate of $\sim$ 400 litres per second for air. The Welch 1376-B80 300 ℓ/min backing pump is mechanically isolated by a dual bellows to prevent it from vibrating the spectrometer. Pressures of $\sim 10^{-6}$ Torr may be attained in the spectrometer chamber with this configuration. The spectrometer table is also acoustically isolated from the floor.

2.3 Cryostat

The samples were mounted in a Janis Supervaritemp Optical Research Dewar (model 8 CNDT)[74]. The tail of the dewar sits at the focus of the spectrometer. A cross-section of the dewar and sample arrangement is shown in Fig. 2–3. Up to two samples may be mounted in the dewar at one time. The usual procedure was to place the sample, and a wedged piece of TPX (with a thin coat of Nujol mineral oil) used as a background, in these positions.

Temperatures from 4.2 K up to room temperature were achieved by vaporizing helium with a heater located beneath the sample. The temperature of the sample was measured using a silicon diode embeded in the sample holder. A second silicon diode is located on the vaporizer. A P.A.R. 152 Temperature Controller monitors the voltage of the diode on the vaporizer and compares it to a reference voltage (determined by the user), and then adjusts the heater current to minimize the difference between them. The reference voltage is used to hold the temperature controller at a fixed temperature. Above 20 K temperatures are accurate to ± 1 K, while below 20 K the sensitivity of the diodes improves and accuracies better than ± 0.1 K are typical.

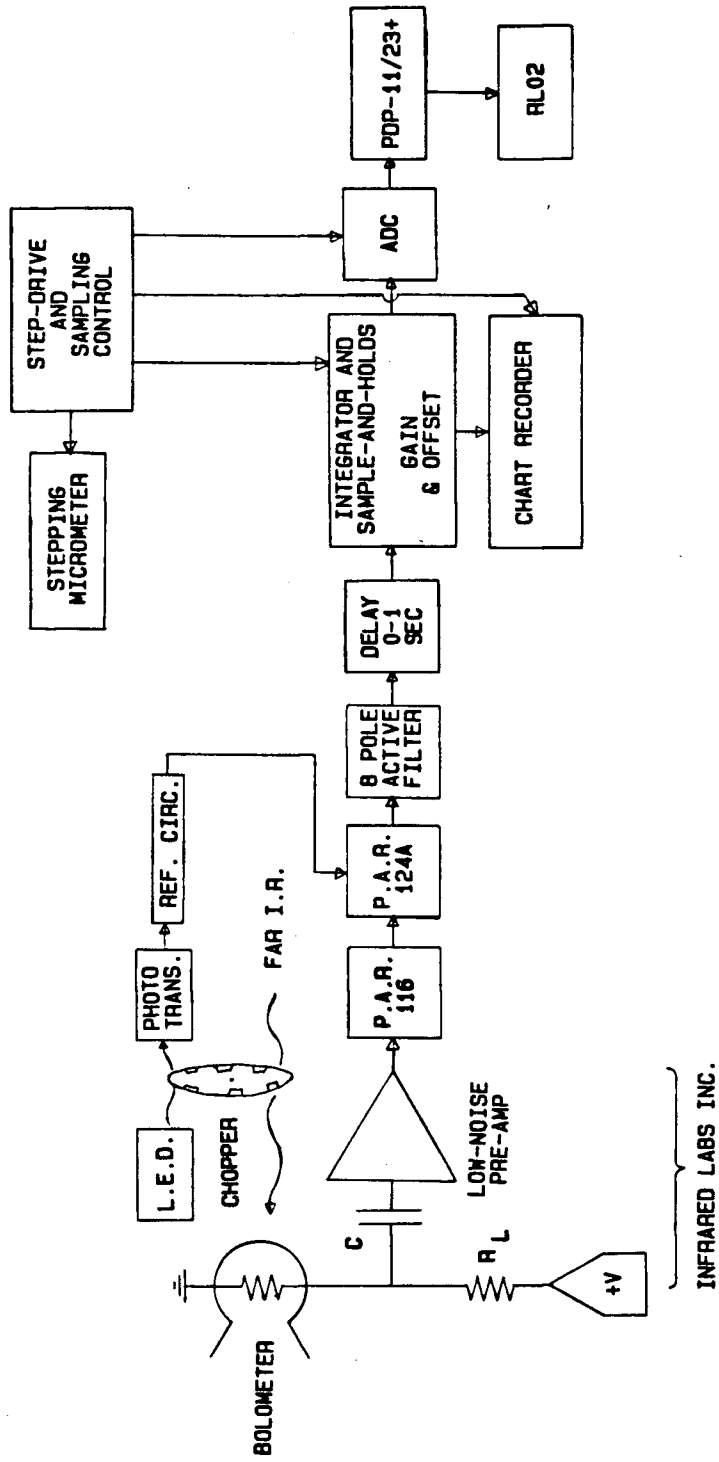

Figure 2-2 A schematic of the detection and recording electronics used in the 10–350 cm^{-1} region. In higher regions the bolometer circuit is replaced by a Golay detector. The rest of the configuration remains unchanged.

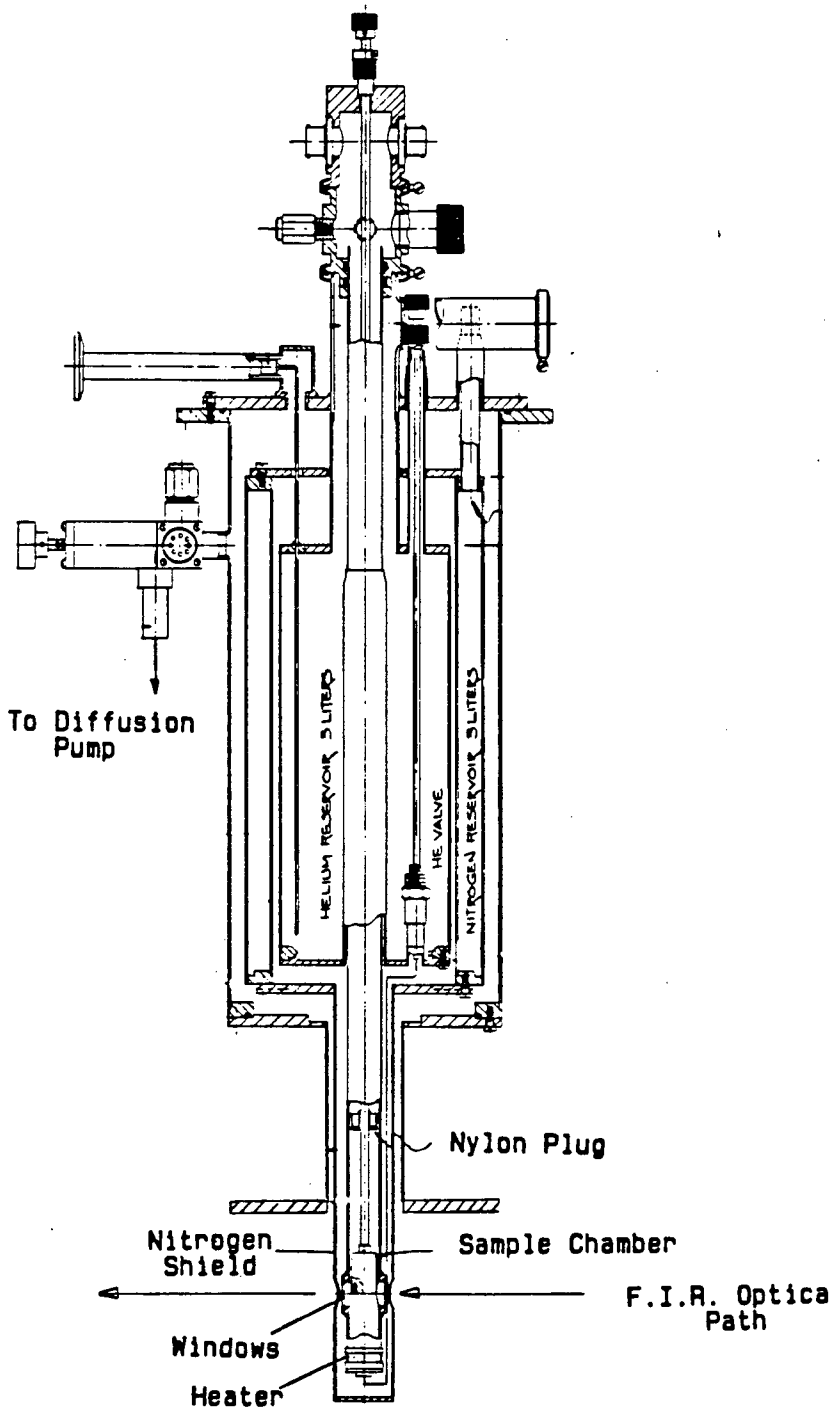

Figure 2-3 A longitudnal cross-sectional view of the Janis Supervaritemp dewar (model 8 CDNT)[74]. The original drawing has been modified to show the changes made in it so that the Nitrogen shield and the sample mount sit in the optical path of the interferometer.

Activated charcoal getter was placed inside the dewar vacuum chamber in order to absorb any Helium gas which goes through the mylar windows above 100 K.

2.4 Detectors

An Infrared Labs[75] composite bolometer of Gallium-doped Germanium on a metalized saphire sheet was used for the experiments in the 10–350 cm^{-1} region. At its operating temperature of 4.2 K it had a responsivity of 8.75×10^3 V/W and a noise equivalent power of 4.8×10^{-13} $W/Hz^{-\frac{1}{2}}$ at 80 Hz.

For those experiments conducted in the 100–750 cm^{-1} region a Pye Unicam[76] type IR50 Golay infrared detector was used.

2.5 The Powder Absorption Coefficient

The powder absorption coefficient (α) is defined by

$$D \approx e^{-\alpha d} \qquad (2-1)$$

where D is the transmitted power and d is the thickness of the powder sample. Because we are measuring the transmitted power through the powder sample, D is equal to the intensity through the sample (I_s) divided by the intensity of the background (I_b), or $I_s/I_b = D$. In this way an absorption line would appear as a dip in the spectrum, however, we represent the absorptions as peaks, so that we consider I_b/I_s, thus

$$\ln\left(\frac{I_b}{I_s}\right) = \ln(D^{-1}) = \alpha d. \qquad (2-2a)$$

Since the thickness (d) of the sample is constant, then this term may be neglected, thus equation 2–2a may be written

$$\alpha \propto \ln\left(\frac{I_b}{I_s}\right). \qquad (2-2b)$$

All of the spectra discussed in this thesis are the powder absorption spectra αd, unless specifically stated otherwise.

2.6 Numerical Analysis

The great advantage of the interferometer is that many different wave numbers may be examined at the same time. This is referred to as the Felgett advantage or "multiplex". To change the interferogram $I(x)$ to its wave number representation $I(\bar{\nu})$ means using a complex Fourier transform (CFT). The CFT $I(\bar{\nu})$ of $I(x)$ is defined as

$$I(\bar{\nu}) = \int_{-\infty}^{\infty} I(x) e^{2\pi i \bar{\nu} x} d\bar{\nu} \qquad (2-3a)$$

or

$$I(\bar{\nu}) = C(\bar{\nu}) + S(\bar{\nu}) \qquad (2-3b)$$

where

$$C(\bar{\nu}) = \int_{-\infty}^{\infty} I(x) \cos(2\pi i \bar{\nu} x) d\bar{\nu} \qquad (2-3c)$$

$$S(\bar{\nu}) = i \int_{-\infty}^{\infty} I(x) \sin(2\pi i \bar{\nu} x) d\bar{\nu} \qquad (2-3d)$$

are refered to as the cosine and sine transforms respectively. We do not deal directly with the real and imaginary parts of the CFT, but rather with the power spectrum (PS) and the phase error (φ) which are defined

$$PS(\bar{\nu}) = \frac{1}{2} \mid I(\bar{\nu}) \mid = \frac{1}{2} \left[C^2(\bar{\nu}) + S^2(\bar{\nu}) \right]^{\frac{1}{2}} \qquad (2-4)$$

$$\varphi(\bar{\nu}) = -\arctan\left(\frac{S(\bar{\nu})}{C(\bar{\nu})} \right). \qquad (2-5)$$

For a symmetric interferogram, $I(x) = I(-x)$, the sine transform is zero, giving the result that $PS(\bar{\nu}) = \frac{1}{2} \mid C(\bar{\nu}) \mid$ and the phase error is zero everywhere. In a real

system, because of component drift and other technical problems, the interferogram will probably not be sampled at the zero path-difference. This effectively adds a phase shift $\phi(\bar{\nu})$ to the transform

$$I(\bar{\nu}) \rightarrow I(\bar{\nu})e^{-i\phi(\bar{\nu})} \qquad (2-6)$$

this yields

$$C(\bar{\nu}) = \frac{I(\bar{\nu})}{2}\cos(\phi(\bar{\nu})) \qquad (2-7)$$

$$S(\bar{\nu}) = \frac{I(\bar{\nu})}{2}\sin(\phi(\bar{\nu})) \qquad (2-8)$$

thus

$$PS(\bar{\nu}) = \frac{1}{2} \mid I(\bar{\nu}) \mid \qquad (2-9)$$

$$\varphi(\bar{\nu}) = -\phi(\bar{\nu}). \qquad (2-10)$$

Thus, the phase error introduced by not sampling symmetrically is eliminated from the PS by taking the two-sided interferogram and performing a complex Fourier transform.

For single-sided interferogram analysis and the averaging of different power spectra, it is necessary to include this phase. This involves symmetrizing the interferogram. Initially, the first ten and the last ten points of the interferogram are fitted to a straight line using a linear least-squares routine. This line is then subtracted from the interferogram to give it a true zero-level and remove any slope caused by temperature drift. The problem remains that it has not been centered through the zero path-difference. By making use of the known fact that the phase error $\varphi(\bar{\nu})$ of a practical interferometer operating in the far infrared is a smooth function and does not vary rapidly with $\bar{\nu}$, we can calculate $\varphi(\bar{\nu})$ from a short

double-sided interferogram. The original center is taken to be the central maximum of the interferogram. When a symmetric interferogram is off-center by an amount ϵ ($\epsilon <$ mirror increment), then the phase error is linear with slope m[77]

$$\varphi(\bar{\nu}) = 2\pi\epsilon\bar{\nu} = m\bar{\nu} \qquad (2-11a)$$

or

$$\epsilon = \frac{m}{2\pi} \qquad (2-11b)$$

The CFT can now be calculated with respect to this new point. The power spectrum will remain unchanged since it has no dependence on $\varphi(\bar{\nu})$. The phase error, which was previously an arbitrary function $\phi(\bar{\nu})$, is now calculated explicitly. Thus, knowing the exact value for the phase error allows us to analyze one-sided interferograms (where the power spectrum does depend on the phase error) and to average spectra.

The apodizing window function that is used for all computations in these experiments is a modification of the one used by Happ and Genzel[78]

$$W(x) = 0.5 + 0.5 \times \cos\left(\frac{\pi x}{X}\right) \qquad (2-12)$$

where x is the step size in the interferogram, and X is the distance from the zero path difference to the edge of the interferogram.

The integrated intensities were calculated by first fitting a linear background to the absorption peak of the powder absorption coefficient, and then summing the area under the curve for a given interval. Usually several backgrounds were chosen.

The line widths were measured by fitting a Lorentzian with a linear background to the peak using a non-linear least-squares fitting program[79].

CHAPTER 3

POWDER ABSORPTION MEASUREMENTS

3.1 Powder Absorption Spectra of Octahedral Anions

The powder absorption spectra of three compounds with octahedral anions (PF_6, AsF_6 and SbF_6) were measured as a function of temperature from 200 K down to 6 K in the 20–125 cm^{-1} region.

The powder absorption spectra of $(TMTSF)_2PF_6$, $(TMTSF)_2AsF_6$ and of $(TMTSF)_2SbF_6$ are shown in Fig. 3–1, Fig. 3–2 and Fig. 3–3 respectively. The spectra are at various temperatures above and below the MI transition, $T_{MI} \sim 12$ K for the PF_6 and AsF_6 compounds, and $T_{MI} \sim 17$ K for the SbF_6 compound, and between 20 cm^{-1} and 90 cm^{-1}. There is no striking evidence of the MI transition in the spectra of any of the octahedral-anion compounds. The powder spectra of $(TMTSF)_2PF_6$ at 6 K agrees with the results in the mid-infrared by Bozio and Pecile *et al.*[63]. Because of the high conductivity of these compounds[54] measured for $\mathbf{E} \parallel \mathbf{a}$ which results in negligible power transmission for this polarization, the resonant modes that are observed in these powders are predominantly polarized with $\mathbf{E} \perp \mathbf{a}$. In each of the octahedral-anion spectra taken at the lowest temperature, there are four sharp resonances. As the temperature is raised the lines shift and are thermally broadened[80]. These modes agree with those seen in the single-crystal reflectivity in $(TMTSF)_2PF_6$ for $\mathbf{E} \perp \mathbf{a}$ by Eldridge and Bates[54]. The modes in $(TMTSF)_2SbF_6$ also agree with those seen in the $\mathbf{E} \perp \mathbf{a}$ single-crystal reflectivity by Ng, Timusk and

Bechgaard[57] and Eldridge and Bates[56]. The modes in $(TMTSF)_2AsF_6$, however, were not seen by Ng, Timusk and Bechgaard in their $\mathbf{E}\perp\mathbf{a}$ single-crystal reflectivity measurements[58], but have been seen by Eldridge and Bates using a composite-bolometer technique[56].

The wave number as a function of temperature for each of the four resonances in $(TMTSF)_2PF_6$, $(TMTSF)_2AsF_6$ and $(TMTSF)_2SbF_6$ are shown in Fig. 3–4, Fig. 3–5 and Fig. 3–6 respectively. In each of the figures, three of the lines have a strong dependence on the temperature indicating an intermolecular (or "external" or "lattice") mode, and the remaining line shows no dependence on the temperature and is thus an intramolecular (or "internal") mode. Extrapolating to $T = 0$ K, $(TMTSF)_2PF_6$ has three lattice modes at 50 ± 0.4 cm^{-1}, 69 ± 0.4 cm^{-1} and 71 ± 0.4 cm^{-1} and one internal mode at 61 ± 0.4 cm^{-1}. Similarly, $(TMTSF)_2AsF_6$ has three lattice modes at 48 ± 0.4 cm^{-1}, 60.4 ± 0.4 cm^{-1}, and 67.5 ± 0.4 cm^{-1} and one internal mode at 56.5 ± 0.4 cm^{-1}, and $(TMTSF)_2SbF_6$ has three lattice modes at 47 ± 0.4 cm^{-1}, 60 ± 0.4 cm^{-1} and 66 ± 0.4 cm^{-1}, and one internal mode at 54.5 ± 0.4 cm^{-1}.

The integrated intensities for each of the four resonances in $(TMTSF)_2PF_6$, $(TMTSF)_4AsF_6$ and $(TMTSF)_2SbF_6$ are shown in Fig. 3–7, Fig. 3–8 and Fig. 3–9 respectively. The intensity of the lines increases down to $\sim$ 12 K in the PF_6 and the AsF_6 compounds, and $\sim$ 17 K in the SbF_6 compound; at which point a MI transition occurs. Below T_{MI} the intensity decreases. The fact that the intensities of these lines are seen to follow the d.c. conductivity indicates that there is electron-phonon coupling. This coupling to free-carriers is similar to that previously observed for a lattice mode in TTF-TCNQ[81].

The spectra for the protonated and deuterated $(TMTSF)_2PF_6$ at 6 K, along with the percentage shifts in the peaks, are shown in Fig. 3–10. The lattice modes can be translational, librational, or a mixture of both. The octahedral compounds

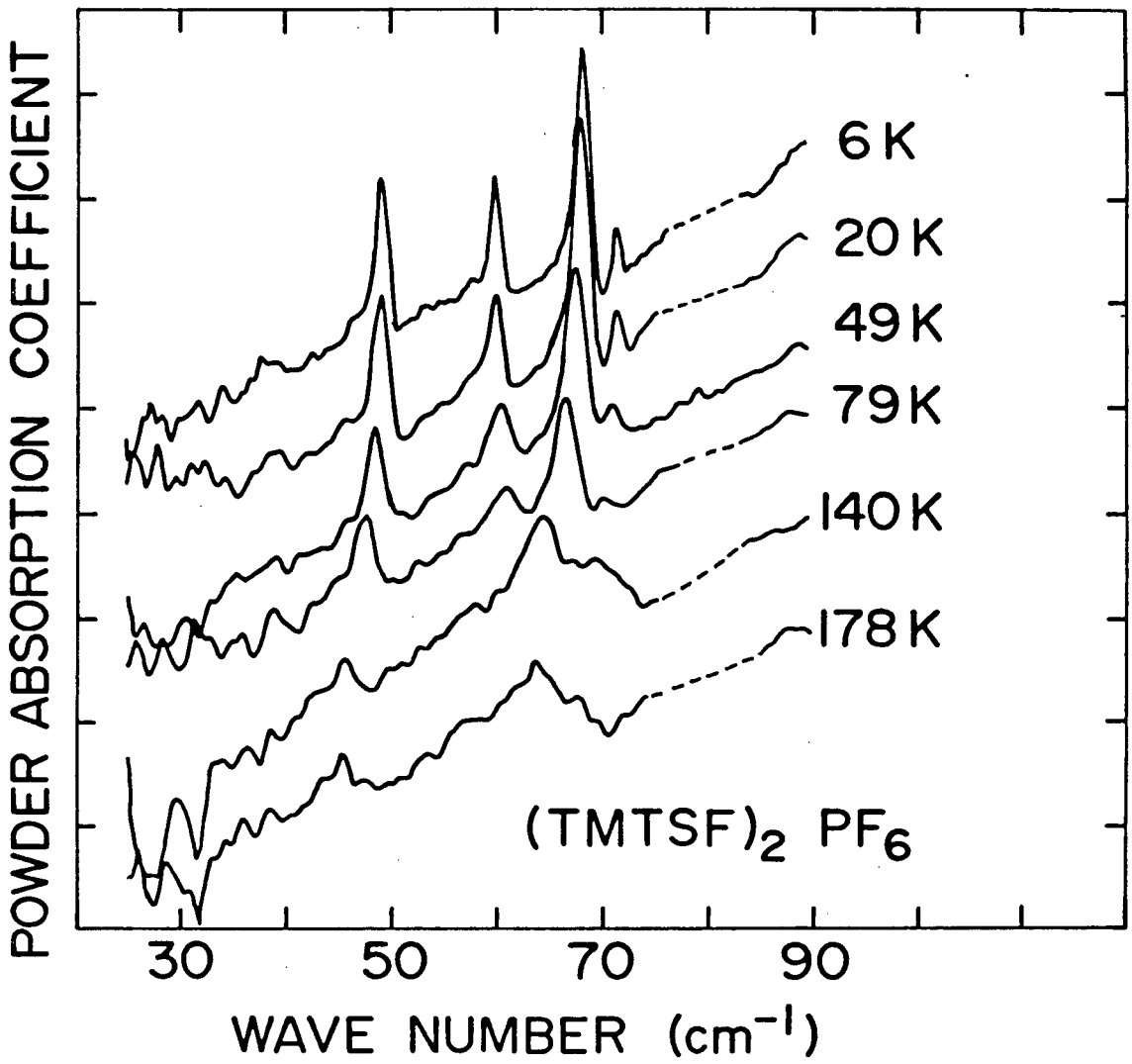

Figure 3-1 Powder absorption coefficient αd (in arbitrary units) of $(TMTSF)_2PF_6$ powder in Nujol on a polyethylene backing showing the four resonances. The dashed line at 80 cm^{-1} replaces an incompletely cancelled polyethylene absorption line. The curves have the same scale and are displaced for clarity.

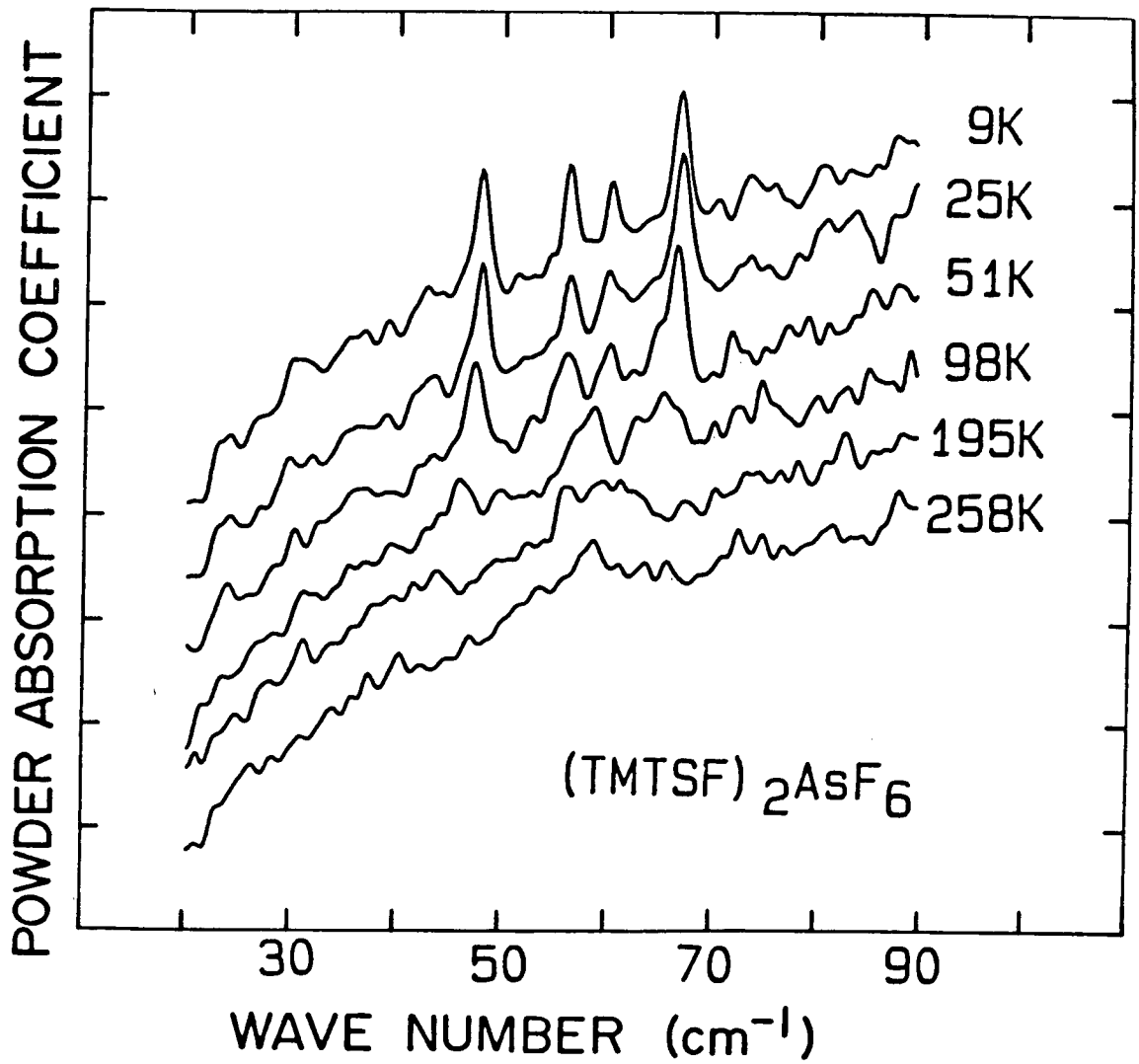

Figure 3-2 Powder absorption coefficient αd (in arbitrary units) of $(TMTFS)_2AsF_6$ powder in Nujol on a TPX backing showing the four resonances. The curves have the same scale and are displaced for clarity.

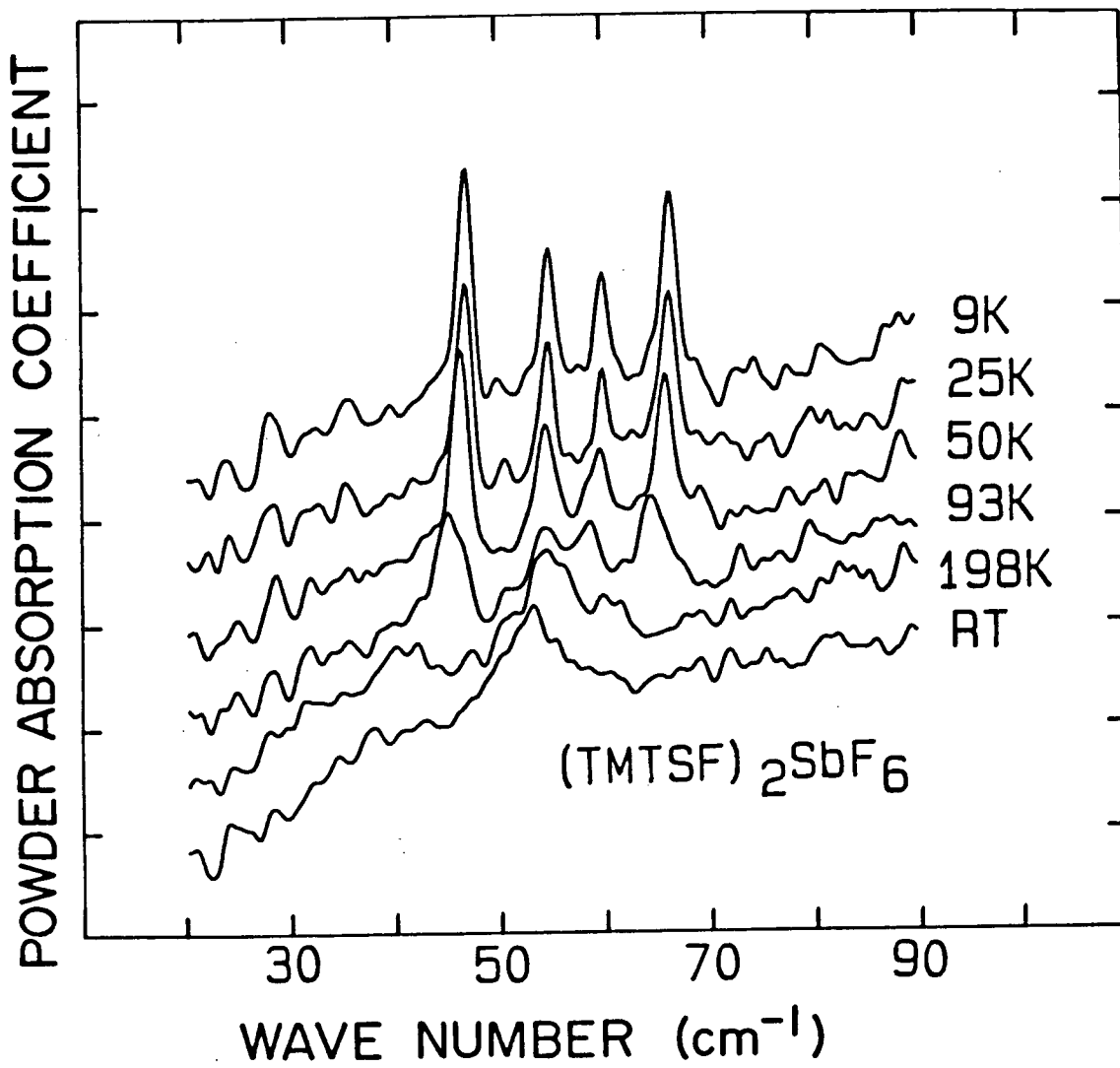

Figure 3-3 Powder absorption coefficient αd (in arbitrary units) of $(TMTSF)_2SbF_6$ powder in Nujol on a TPX backing showing the four resonances. The curves have the same scale and are displaced for clarity.

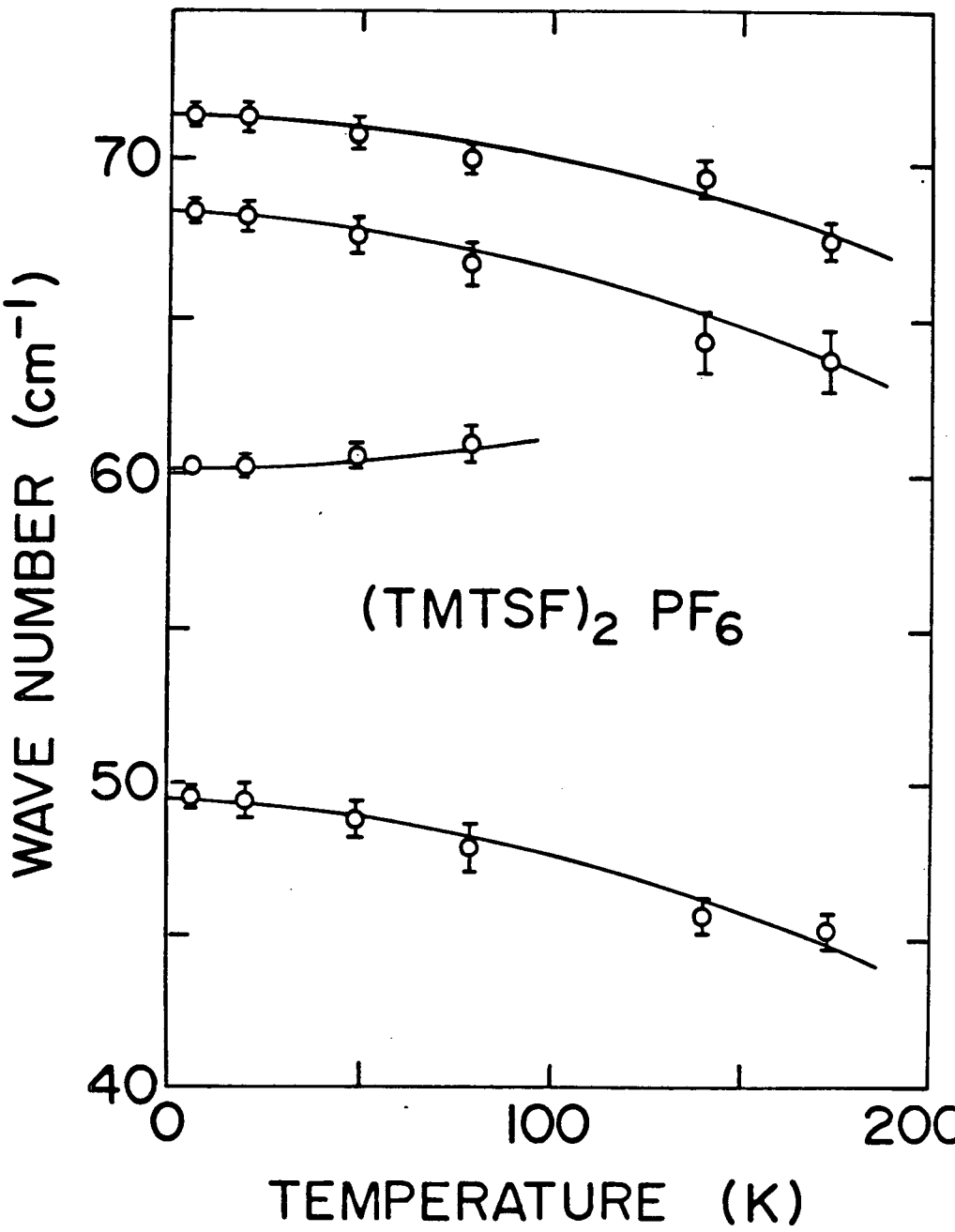

Figure 3-4 The temperature dependence of wave number of the four $(TMTSF)_2PF_6$ lines seen in Figure 3–1. Three lattice modes are indicated by the strong temperatue dependence. An internal mode is seen at 61 cm^{-1} ($T = 0$ K).

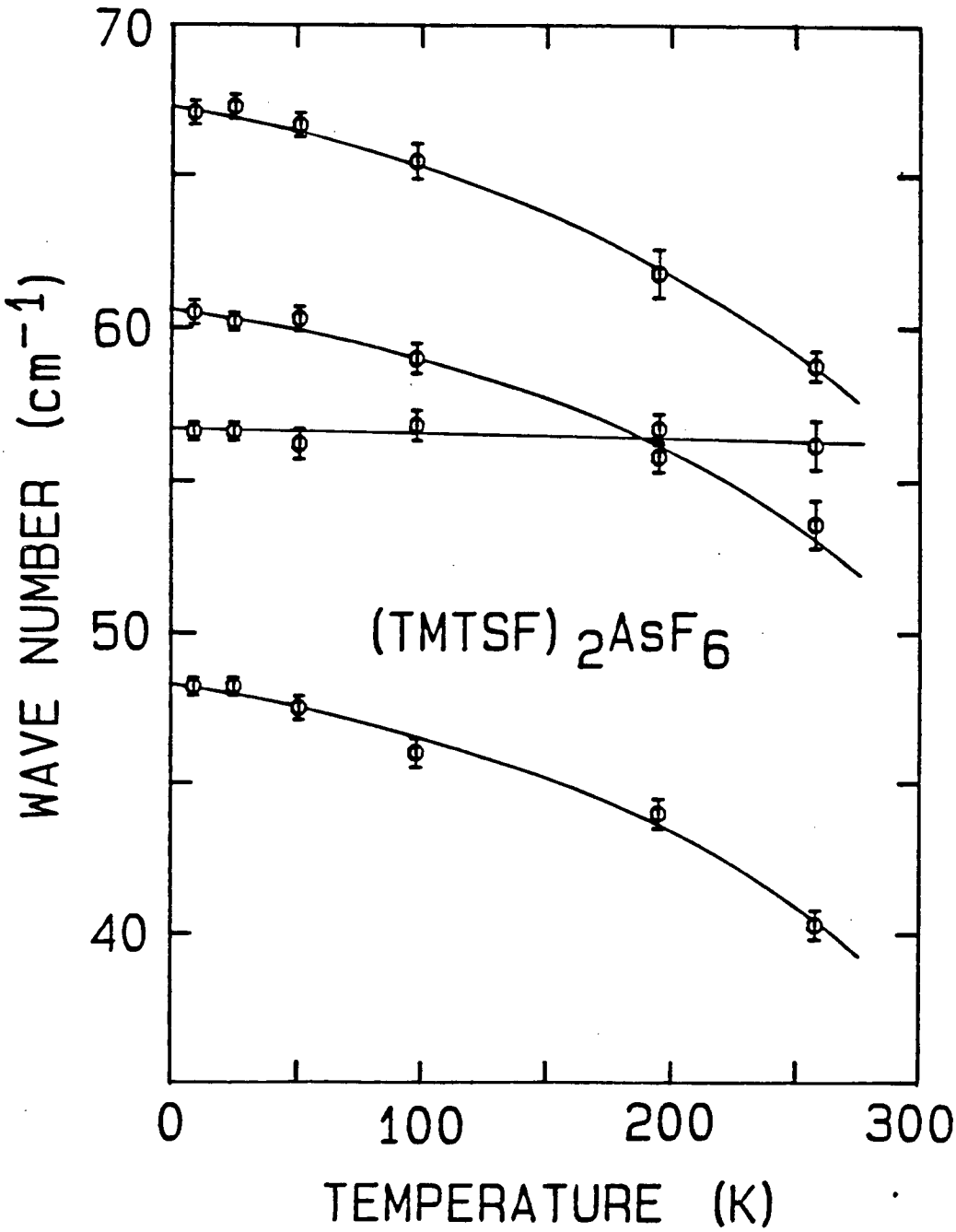

Figure 3-5 Temperature dependence of wave number of the four $(TMTSF)_2AsF_6$ lines seen in Figure 3–2. Three lattice modes are indicated by the strong temperature dependence. An internal mode is seen at 56.5 cm^{-1} ($T = 0$ K).

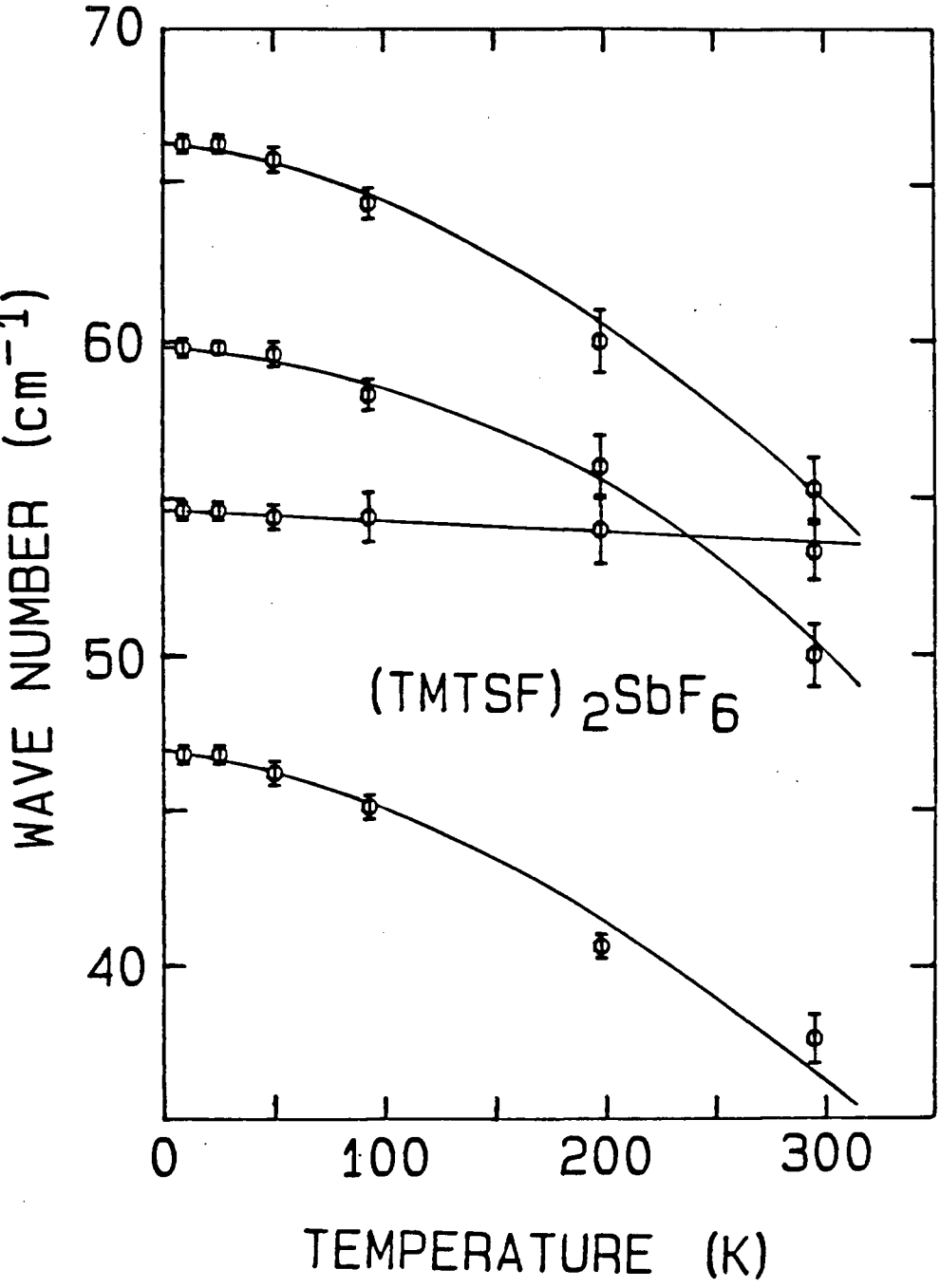

Figure 3-6 Temperature dependence of wave number of the four $(TMTSF)_2SbF_6$ lines in Figure 3–3. Three lattice modes are indicated by the strong temperature dependence. An internal mode is seen at 54.5 cm^{-1} ($T = 0$ K).

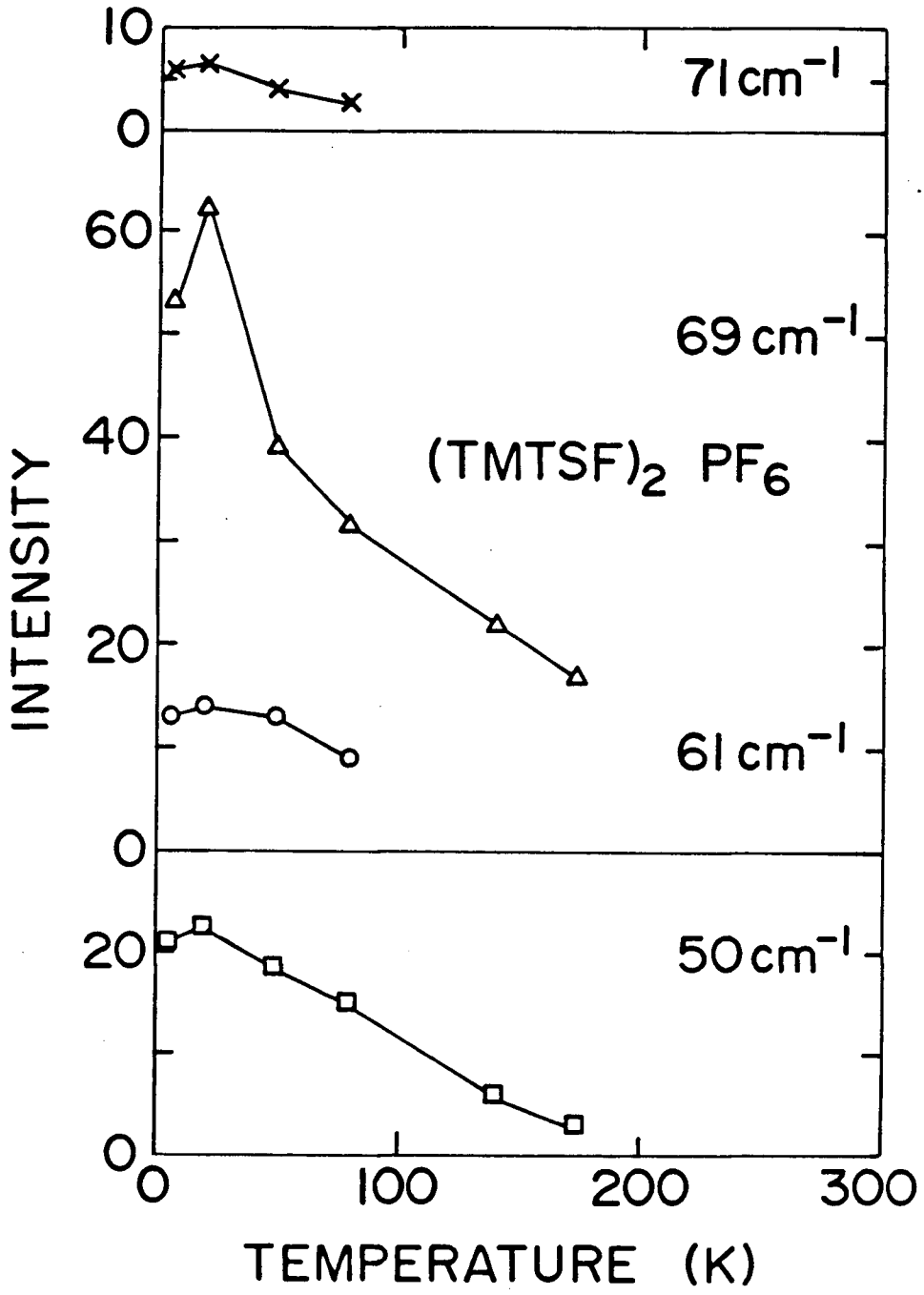

Figure 3-7 The integrated intensity of the four lines of $(TMTSF)_2PF_6$ seen in Fig. 3–1 versus temperature. The units are arbitrary, but each of the lines has the same scale. Note the turnover below the phase transition at ~ 12 K, indicating the onset of the insulating SDW state.

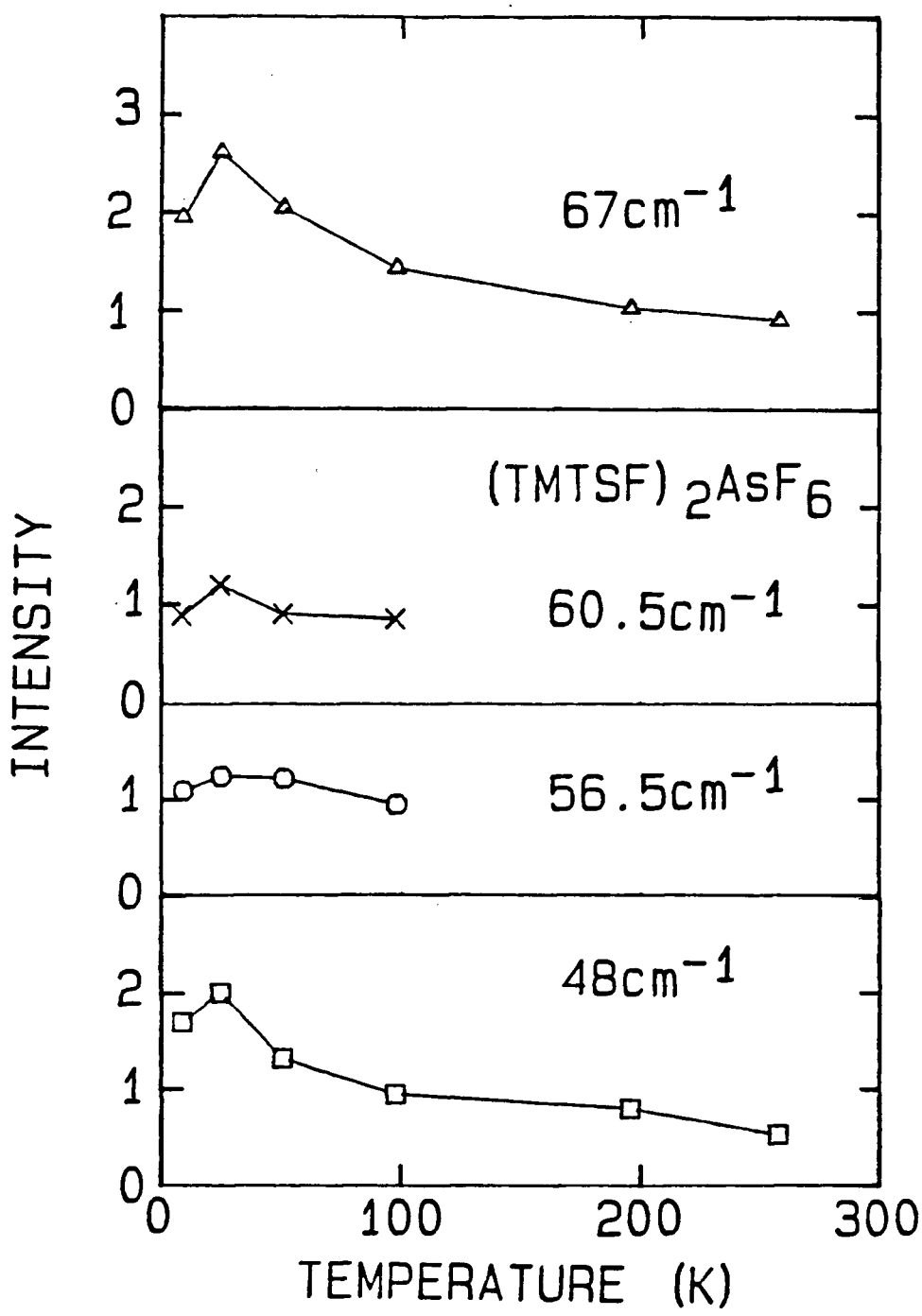

Figure 3-8 The integrated intensity of the four lines of $(TMTSF)_2AsF_6$ seen in Fig. 3–2 versus temperature. The units are arbitrary, but each of the lines has the same scale. Note the turnover below the phase transition at $\sim$ 12 K, indicating the onset of the insulating SDW state.

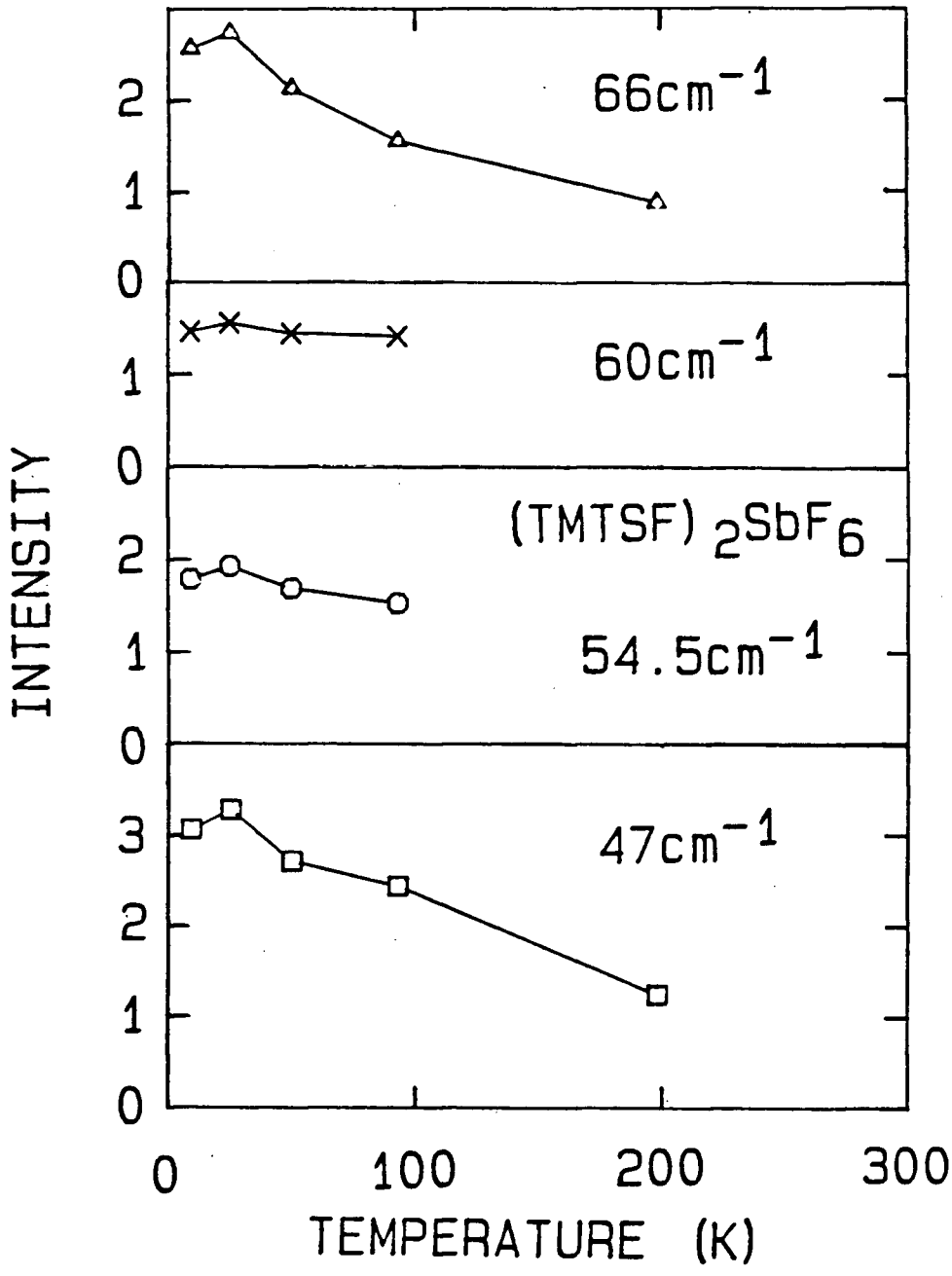

Figure 3-9 The integrated intensity of the four lines of $(TMTSF)_2SbF_6$ seen in Fig. 3–3 versus temperature. The units are arbitrary, but each of the lines has the same scale. Note the turnover below the phase transition at $\sim$ 17 K, indicating the onset of the insulating SDW state.

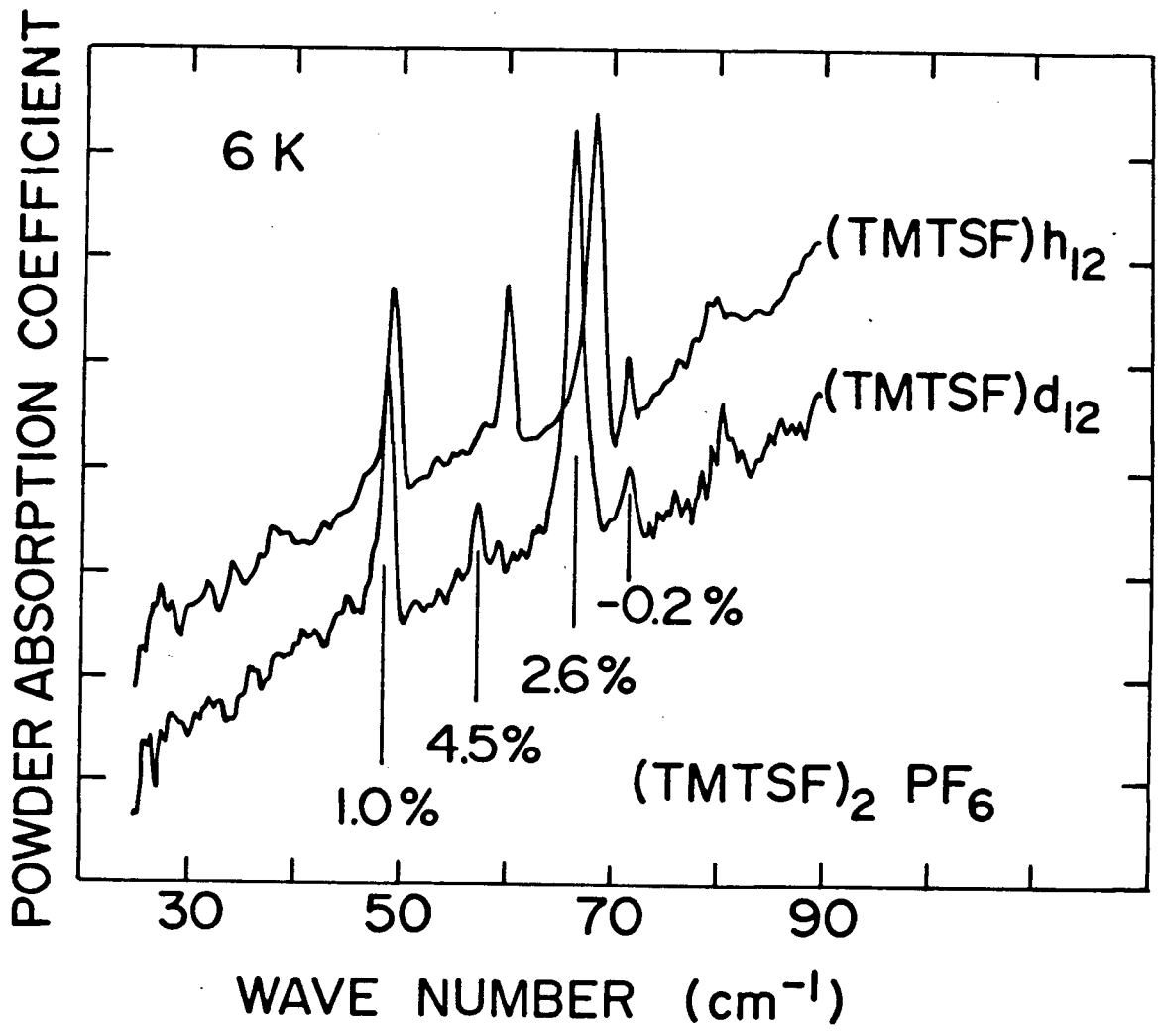

Figure 3-10 The 6-K powder spectra of protonated and deuterated $(TMTSF)_2PF_6$ powders, in Nujol on a polyethylene backing showing the four resonances. The percentage decrease in wave number is indicated. The curves have been rescaled and vertically displaced for clarity.

Table III–I[a]

Caculated and measured isotope shifts of the $(TMTSF)_2X$ lattice modes. (Coordinates are shown in Fig. 3–12)

Type	Molecules involved	ν_p/ν_d (calc)	ν_p/ν_d (meas)
Translational	2(TMTSF) 1(PF_6)	1.002	
Translational	TMTSF alone	1.013	1.010
Libration R_x	2(TMTSF) 1(PF_6)	1.001	
Libration R_x	TMTSF alone	1.044	
Libration R_y	2(TMTSF) 1(PF_6)	1.002	
Libration R_y	TMTSF alone	1.052	
Libration R_z	2(TMTSF) 1(PF_6)	1.002	
Libration R_z	TMTSF alone	1.024	1.026
?	2(TMTSF) 1(PF_6)		0.998

[a] Ref. 82

are different from the tetrahedral ones in that the librational modes of the anions are not allowed by symmetry to couple with the infrared active lattice modes involving the TMTSF. For the tetrahedral compounds infrared active modes can involve librations of the anions. Table III–I shows the calculated shifts expected upon deuteration for the various pure (unmixed) lattice modes. The shifts for the translational modes were calculated starting from

$$\nu \propto \sqrt{\frac{K}{m_r}} \qquad (3-1a)$$

and assuming that upon deuteration the change in the force constants is small, then

$$\frac{\nu_p}{\nu_d} = \sqrt{\frac{m_r^{deut}}{m_r^{prot}}} \qquad (3-1b)$$

where the reduced mass is defined as

$$\frac{1}{m_r} = \frac{1}{m} + \frac{1}{2M} \qquad (3-2)$$

for the two TMTSF molecules and one PF_6 molecule. This is different from the usual expression for the reduced mass in the $\mathbf{k} = 0$ optical mode, because, in this case, both TMTSF molecules move together. The system was therefore treated as if it contained only two masses; one of mass m and another of mass $2M$ (the anion mass is m, the TMTSF mass is M, and the terms "prot" and "deut" represent the protonated and deuterated compounds respectively). The shift for the librational modes is calculated in the following manner

$$\frac{\nu_p}{\nu_d} = \sqrt{\frac{I_{ii}^{deut}}{I_{ii}^{prot}}} \qquad (3-3)$$

where the moments of inertia are defined as

$$\frac{1}{I_{ii}} = \frac{1}{I_{ii}^{anion}} + \frac{1}{2I_{ii}^{TMTSF}} \qquad (3-4)$$

for two TMTSF molecules and one PF_6 molecule. Again, the system is being treated as if it contained only two masses (an anion of mass m and a cation of mass $2M$) and hence only two moments of inertia. The justification for this type of approach is motivated by the experimental results. If the system is treated for three masses the calculated shifts upon deuteration are too large; however, if the system is treated as it consists of only two masses (m and $2M$) then the agreement with observations is much closer. Here I_{ii} represents the moment of inertia along the principal axes ($i = x, y$ or z) in the anion molecule and in the TMTSF molecule. Because the anion PF_6 is centrosymmetric, and we have chosen the origin at the center and the principal axes along the P–F bonds, then all of the moments are the same. The moment of inertia in the TMTSF molecule is calculated in the form

of an inertial tensor using the bond lengths and angles from the structure paper for $(TMTSF)_2PF_6$[15]. The internal coordinate system for the TMTSF molecule is shown in Fig. 3–11. The origin is chosen at the center of the C–C bond joining the two fulvalene rings. The measured values of ν_p/ν_d are also shown in Table III–I next to the ratio it most closely matches. This suggests that in $(TMTSF)_2PF_6$ the line at 50 cm^{-1} is a translational mode involving just the TMTSF molecule, and that the line at 69 cm^{-1} is a librational mode along the z-axis involving just the TMTSF molecule. The lattice mode at 71 cm^{-1} experiences a very small shift upon deuteration. Because of the associated error of $\pm 0.2\%$, it is impossible to assign it to a translational or a librational mode directly, however, from group theory we would expect the librations to include just the TMTSF molecules. This suggests that the 71 cm^{-1} feature is a translational mode involving both the TMTSF and PF_6 molecules. The mode at 61 cm^{-1} experiences a shift of 4.5% upon deuteration. From Table III–I, this shift is comparable to that of a librational R_x mode for just the TMTSF molecules (4.4%), or a librational R_y mode for just the TMTSF molecules (5.5%). It is evident from the temperature dependence of the modes in Fig. 3–4 that the 61 cm^{-1} line is an internal mode, and not a libration. The proximity of the 4.5% shift to the librational R_x and R_y modes, however, indicates that the internal mode probably has a torsion or a bending about either the x- or the y-axis.

The two possible low-energy internal modes together with the calculated isotope shifts are shown in Fig. 3–11. The shift for the in-plane bending about the x-axis, the $\nu_{54}(b_{2u})$ mode, is calculated[82]

$$\frac{\nu_p}{\nu_d} = \sqrt{\frac{(I_x - MD^2)_d}{(I_x - MD^2)_p}} \qquad (3-5)$$

This calculation is performed with only half a molecule since the origin acts as the pivot point. Thus D is the distance from the origin to the center of mass, M is the

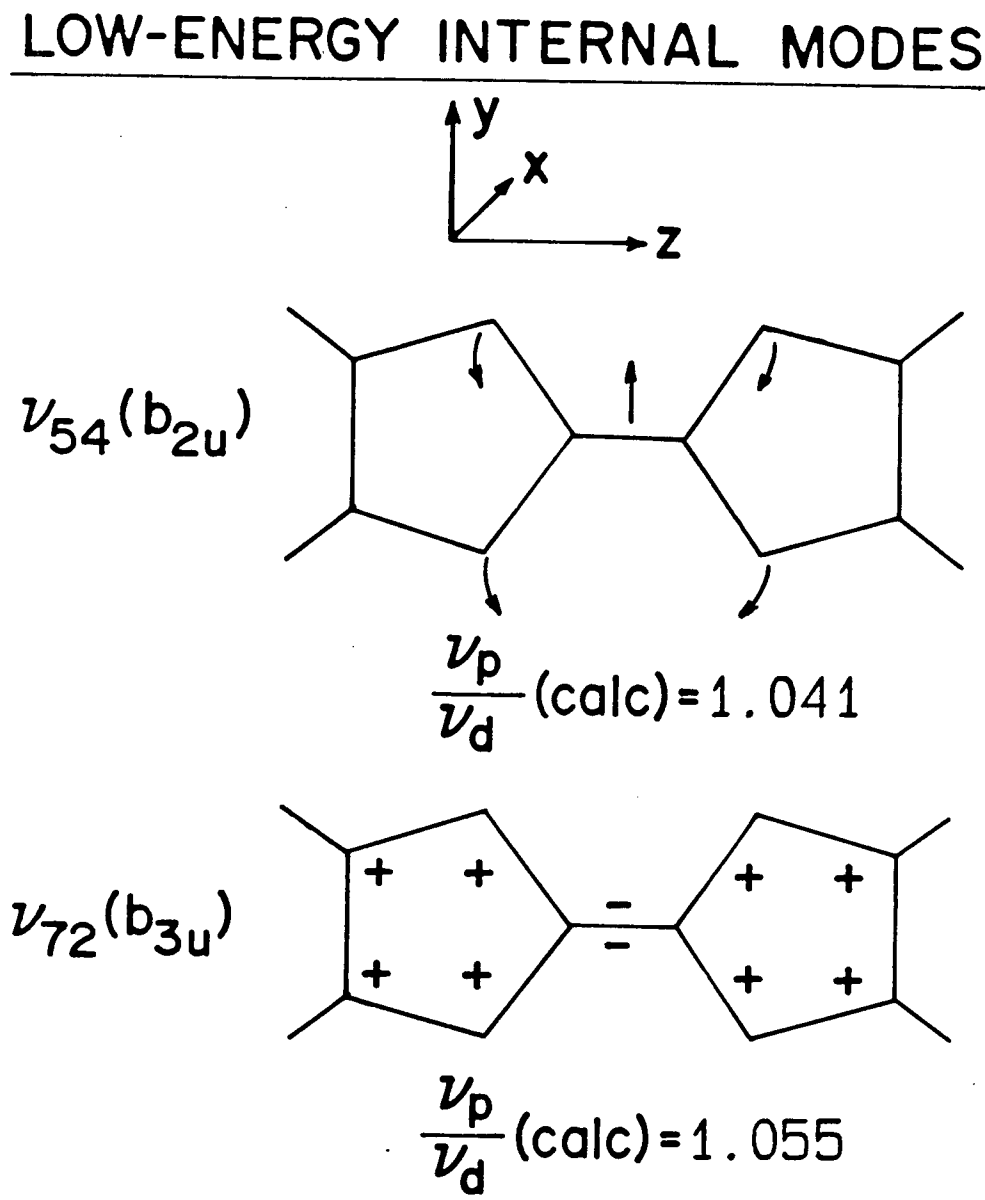

Figure 3-11 The internal coordinate system for the TMTSF molecule, and the two lowest-energy modes of TMTSF[64], with the calculated shift upon deuteration (see equations 3–5 and 3–6).

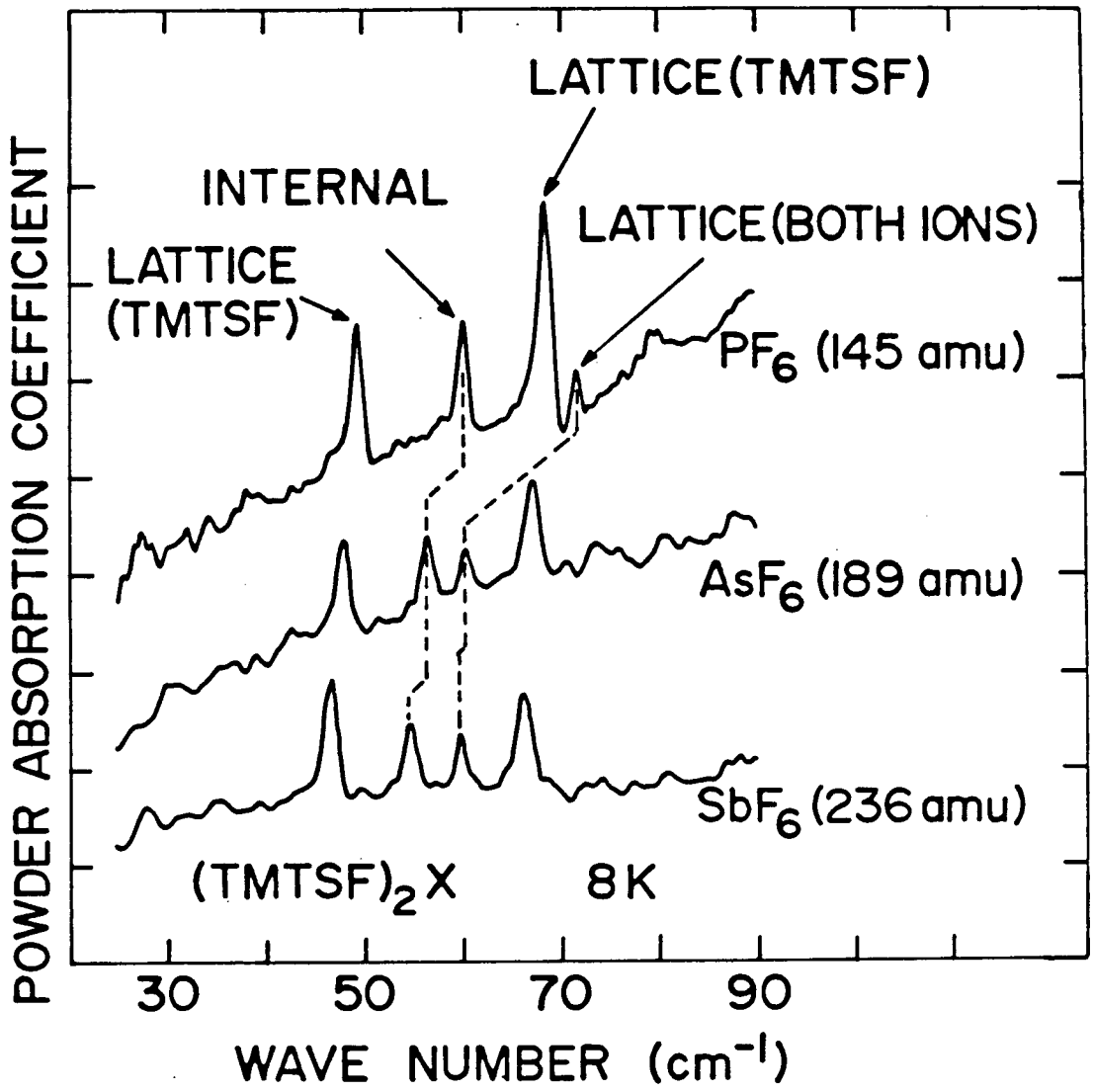

Figure 3-12 The 8-K powder absorption coefficient αd (in arbitrary units) of $(TMTSF)_2PF_6$, $(TMTSF)_2AsF_6$ and $(TMTSF)_2SbF_6$ powders in Nujol on a TPX backing, except for PF_6, which had a polyethylene mount. The curves are rescaled and vertically displaced for clarity. The nature of the resonances is indicated and the dashed lines follow the features through the compounds. The molecular weight is included for reference.

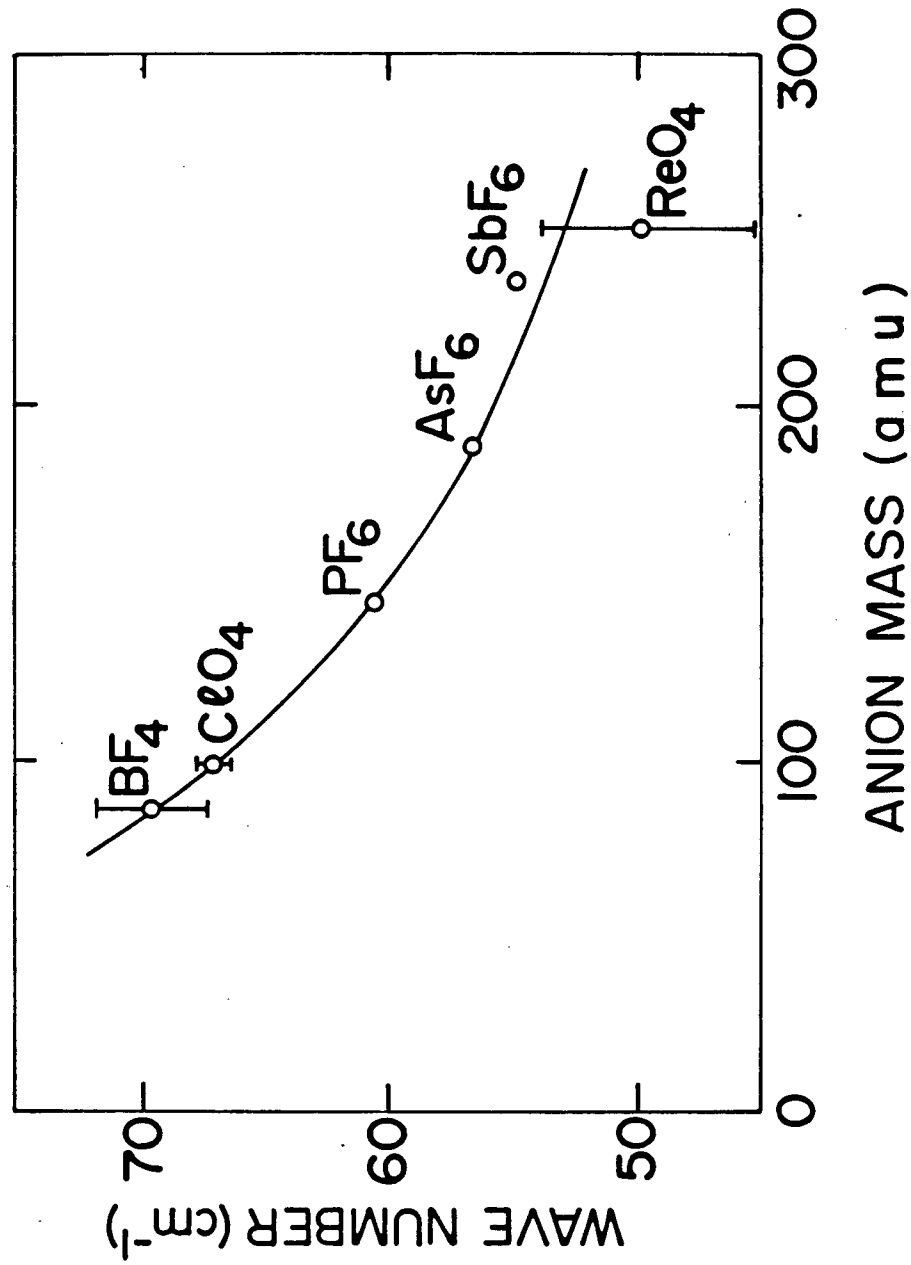

Figure 3-13 The wave number of the internal mode versus anion mass. The dependence shows a weakening of the lattice component of the force constant as the lattice expands. The accuracy of the internal mode wave number in the tetrahedral-anion compounds is poor due to the uncertainty in assignment, which resulted from the splittings and limited temperature range. The solid line is drawn as a guide to the eye.

mass of half of the molecule and $I_x = I_{xx}/2$. The shift for the out-of-plane bending about the y-axis, the $\nu_{72}(b_{3u})$ mode, is calculated[82]

$$\frac{\nu_p}{\nu_d} = \sqrt{\frac{(I_y - MD^2)_d}{(I_y - MD^2)_p}} \qquad (3-6)$$

where $I_y = I_{yy}/2$. The calculated shifts are 1.041 for the in-plane mode, and 1.055 for the out-of-plane mode. The measured shift is $4.5 \pm 0.2\%$. As in the case of TTF-TCNQ[81] it is not really possible to distinguish between these two modes on the basis of the observed 4.5% shift, but since the deuteration was not complete, and the polarized spectra in the TTF-TCNQ indicated the b_{3u} mode, it is probable that we are also observing the $\nu_{72}(b_{3u})$ mode.

The translational and librational modes are very likely mixed[82]. The irreducible representation for the translational modes (Γ_t) is given by[83]

$$\Gamma_t = (3A_g + 3A_u)(\text{TMTSF}) + 3A_u(PF_6) \qquad (3-8)$$

where A_u and A_g belong to the C_i representation which is isomorphous with the $P\bar{1}$ space group. The representation Γ_t includes the three acoustic modes, giving three Raman active and three infrared active modes. The representation the rotational vibrations (Γ_r) is given by[83]

$$\Gamma_r = (3A_u + 3A_g)(\text{TMTSF}) + 3A_g(PF_6) \qquad (3-9)$$

where the $3A_u$ modes only involve the TMTSF molecules, giving three infrared and six Raman modes. Thus one expects a total of six infrared-active modes, and since TMTSF is not at an inversion center there will be mixing of the translational and librational motions.

By following the relative intensities of the lines for different anion substitutions, the shifts of the resonances can be traced. This is not obvious from the

integrated intensities in Figs. 3–7, 3–8 and 3–9. The 8-K powder spectra of the PF_6, AsF_6 and SbF_6 compounds are compared in Fig. 3–12. this composite makes it easy to follow the shifts of the modes, starting with the lightest anion, PF_6 (145 amu) and proceeding to AsF_6 (189 amu) and SbF_6 (236 amu). The line shifts are shown in Table III–II.

Table III–II

Line shifts for different octahedral anions.

Type of resonance	PF_6 (cm^{-1}) ± 0.4	AsF_6 (cm^{-1}) ± 0.4	SbF_6 (cm^{-1}) ± 0.4
Translation	50.0	48.0	47.0
Internal	61.0	56.5	54.5
Libration R_z	69.0	67.0	66.0
Translation	71.0	60.5	60.0

The spectra in Figs. 3–1, 3–2 and 3–3 are all very similar to each other displaying four resonances, fairly close in number. Two of the lattice modes shift very little in going from one compound to another, indicating the negligible role of the anion (one is a translational mode involving just the TMTSF molecule, the other is a librational R_z mode involving just the TMTSF molecule). The third lattice mode, which involves both ions, shifts considerably between the PF_6 and AsF_6, but very little between the AsF_6 and SbF_6. In the latter case it is probably interacting with adjacent modes. The internal mode shifts slightly from one compound to another, as the force constants are modified slightly by the changing size of the unit cell. Figure 3–13 shows the wave number of the $\nu_{72}(b_{3u})$ interval mode as a function of anion mass. The fact that a smooth line can be drawn through the points indicates that the complicated dependence of the internal mode on the out-of-plane restoring forces and the methyl interaction with the anion is mostly reduced to some unknown function of the anion mass.

This sort of behavior is seen in the ν_3 mode of the ReO_4^- anion in the alkali halide salts[84]. The ν_3 mode shifts upwards as the lattice constant is decreased.

3.2 Powder Absorption Spectra of Tetrahedral Anions

The powder absorption spectra of three compounds with tetrahedral anions (BF_4, ClO_4 and ReO_4) were measured as a function of temperature from 200 K down to 6 K in the 20–90 cm^{-1} region. The spectra of these compounds are very different from those of the octahedral-anion compounds. For the tetrahedral compounds the infrared active modes can involve librations of the anions which can couple to the TMTSF infrared active lattice modes. The disorder or low site symmetry of the anions removes the degeneracy of some of the anion modes, *i.e.* we may see splitting of these bands. Other anion modes which are normally infrared inactive may be activated by the disorder.

The powder absorption spectra of $(TMTSF)_2BF_4$, $(TMTSF)_2ClO_4$ and of $(TMTSF)_2ReO_4$ are shown in Fig. 3–14, Fig. 3–15 and Fig. 3–16 respectively, at temperatures above and below the MI transition. In Figs. 3–14 and 3–16, the curves are not vertically displaced, and have the same ordinate origin and scale. Above the MI transition there is continuous and strong free-carrier absorption, increasing with wave number as expected. Below the MI transition, $T_{AO} = 38$ K for $(TMTSF)_2BF_4$ and $T_{AO} = 180$ K for $(TMTSF)_2ReO_4$, the absorption decreases due to the to the formation of a semiconducting gap at the Fermi surface.

The powder absorption spectra of protonated and deuterated $(TMTSF)_2BF_4$, $(TMTSF)_2ClO_4$ and $(TMTSF)_2ReO_4$ at ~ 6 K in the 20–90 cm^{-1} region are shown in Fig. 3–17, Fig. 3–18 and Fig. 3–19 respectively. The percentage shifts of the lines have been included.

In $(TMTSF)_2BF_4$ vibrational resonances begin to appear at 70 cm^{-1} and 80 cm^{-1}, but the peaks are broadened by thermal motion and anion disorder. At 6 K, the peaks have split up into multiplets, and there is a lot of additional structure at

33 cm^{-1} and between 40 cm^{-1} and 60 cm^{-1}, as shown in Fig. 3–14. The spectra of $(TMTSF)_2BF_4$ is very complex below the MI transition, and without more detailed temperature dependent measurements the assignments cannot be certain. Tentative assignments based on the isotope shifts shown in Fig. 3–17 and the calculations in Table III-I indicate that the mode at $\sim$ 40 cm^{-1} is a lattice mode involving both the TMTSF molecule and the anion molecule, and the modes at $\sim$ 50 cm^{-1} and $\sim$ 80 cm^{-1} are translational and librational lattice modes respectivley. The internal $\nu_{72}(b_{3u})$ mode is at $\sim$ 70 cm^{-1}. The positions are approximate because we cannot be certain which of the multiplet peaks corresponds to the true resonance. The feature at 32 cm^{-1} does not shift.

Below T_{AO} in $(TMTSF)_2ReO_4$ broad vibrational resonances appear. At 10 K there are four lines that dominate the spectra between 35 cm^{-1} and 60 cm^{-1}, similar to the sort of spectra displayed in the compounds with octahedral anions. There is also additional structure seen at 28 cm^{-1}, 70 cm^{-1} and 80 cm^{-1}, as shown in Fig. 3–16. While the ReO_4 compound does not have the same multiplet structure as seen in the BF_4 compound, it does have some shoulders on the peaks as well as some extra structure between 60 cm^{-1} and 90 cm^{-1}. Tentative assignments based on the isotope shifts shown in Fig. 3–19 and the calculations in Table III-I indicate that the resonance at 40 cm^{-1} is a translational mode involving just the TMTSF molecule, the resonance at 49 cm^{-1} is a lattice mode involving both the TMTSF molecule and the anion molecule and the line at 54 cm^{-1} is a librational mode involving just the TMTSF. The internal mode is very difficult to locate and seems to be split into peaks at $\sim$ 42 cm^{-1} and $\sim$ 51 cm^{-1}, however both of these peaks have isotopic shifts that are characteristic of the $\nu_{72}(b_{3u})$ internal mode, and there is an uncertainty of $\sim$ 5 cm^{-1} in its position.

The spectra for $(TMTSF)_2ClO_4$, shown in Fig. 3–15, is slightly different in behavior than the BF_4 and ReO_4 compounds. A MI transition due to anion ordering occurs at $T_{AO} = 24$ K in this compound, but the Fermi surface is not destroyed and

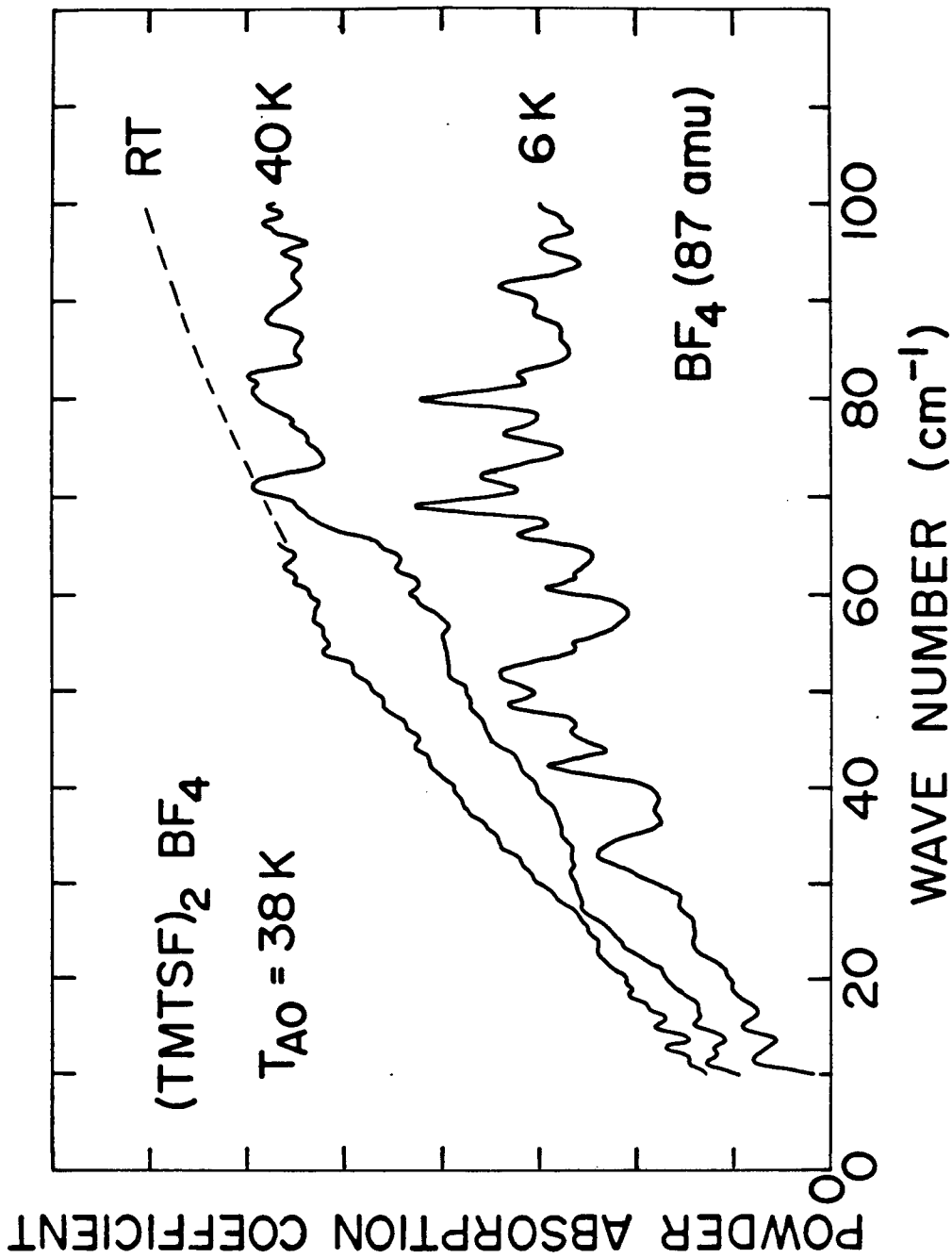

Figure 3-14 Powder absorption coefficient αd (in arbitrary units) of $(TMTSF)_2BF_4$ powder in Nujol on on a TPX backing. The curves are not displaced and have the same scale and origin. The anion-ordering temperature is indicated. A dashed line extrapolates the room temperature spectrum above 65 cm^{-1} due to large noise resulting from the strong absorption. Cooling through T_{AO} was at < 1 K/min.

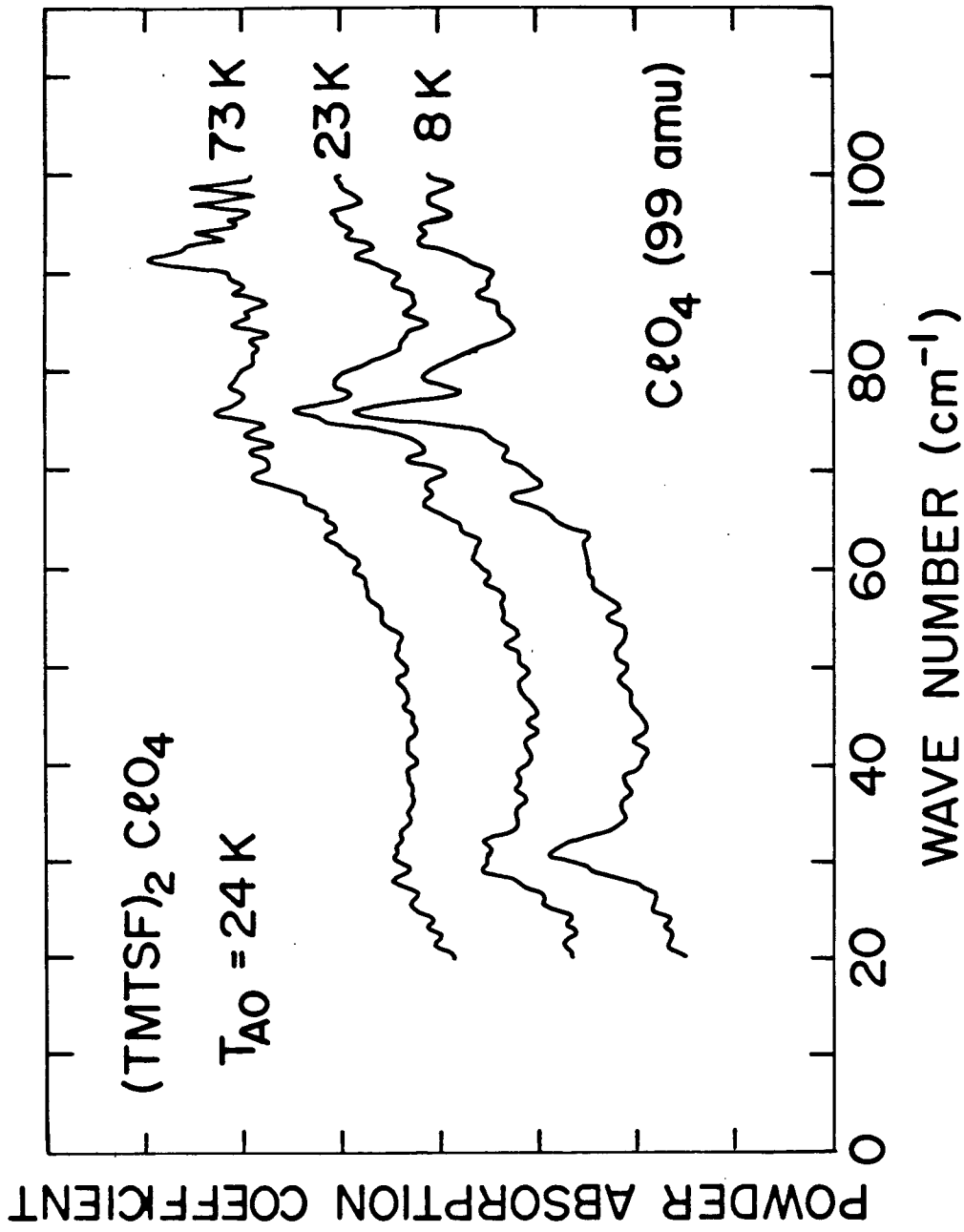

Figure 3-15 Powder absorption coefficient αd (arbitrary units) of $(TMTSF)_2ClO_4$ powder in Nujol on a TPX backing. The curves are displaced for clarity. The anion-ordering temperature is indicated. Cooling through T_{AO} was at < 1 K/min.

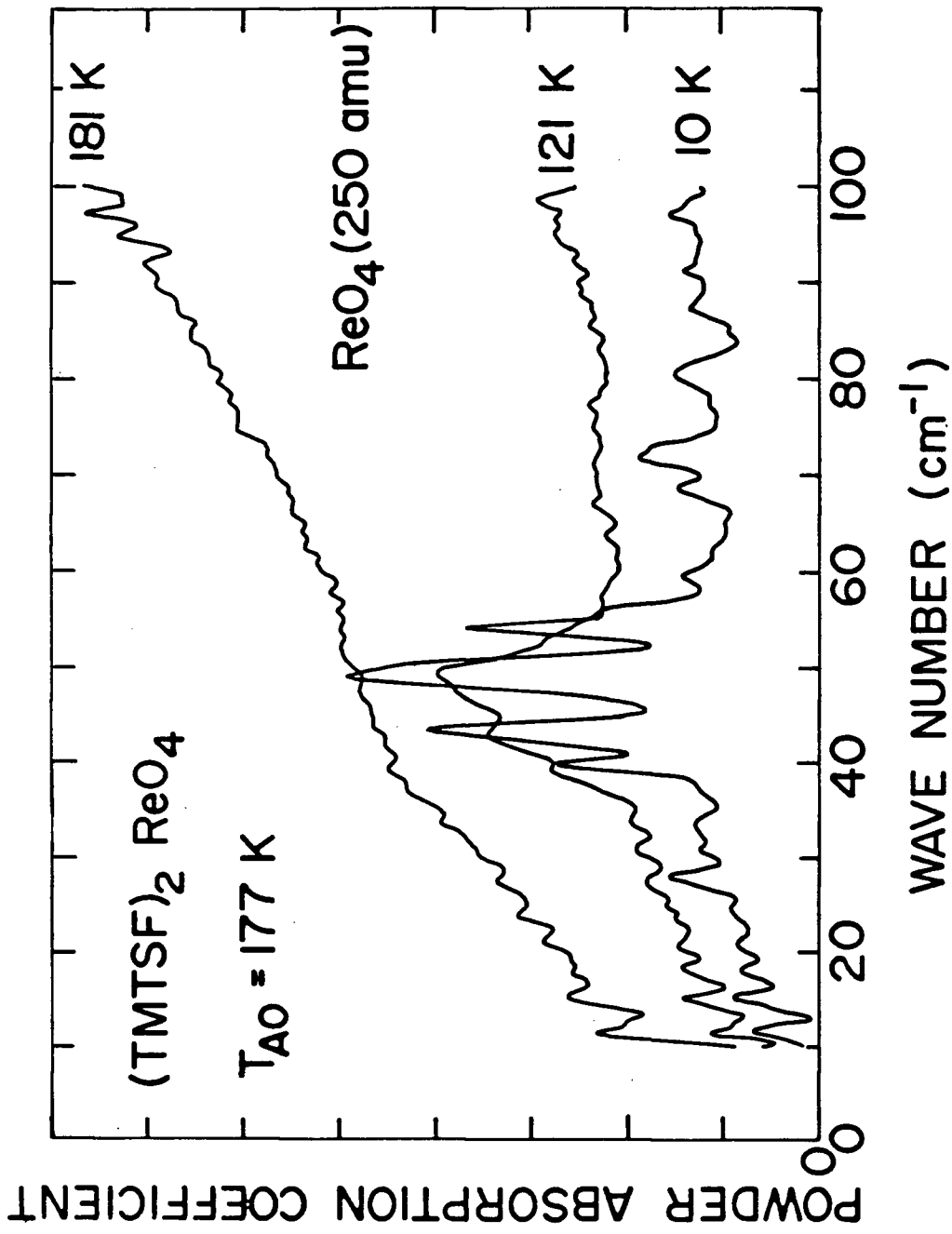

Figure 3-16 Powder absorption coefficient αd (arbitrary units) of $(TMTSF)_2ReO_4$ powder in Nujol on a TPX backing. The curves have not been displaced and have the same scale and origin. The anion-ordering temperature is indicated. Cooling through T_{AO} was at < 1 K/min.

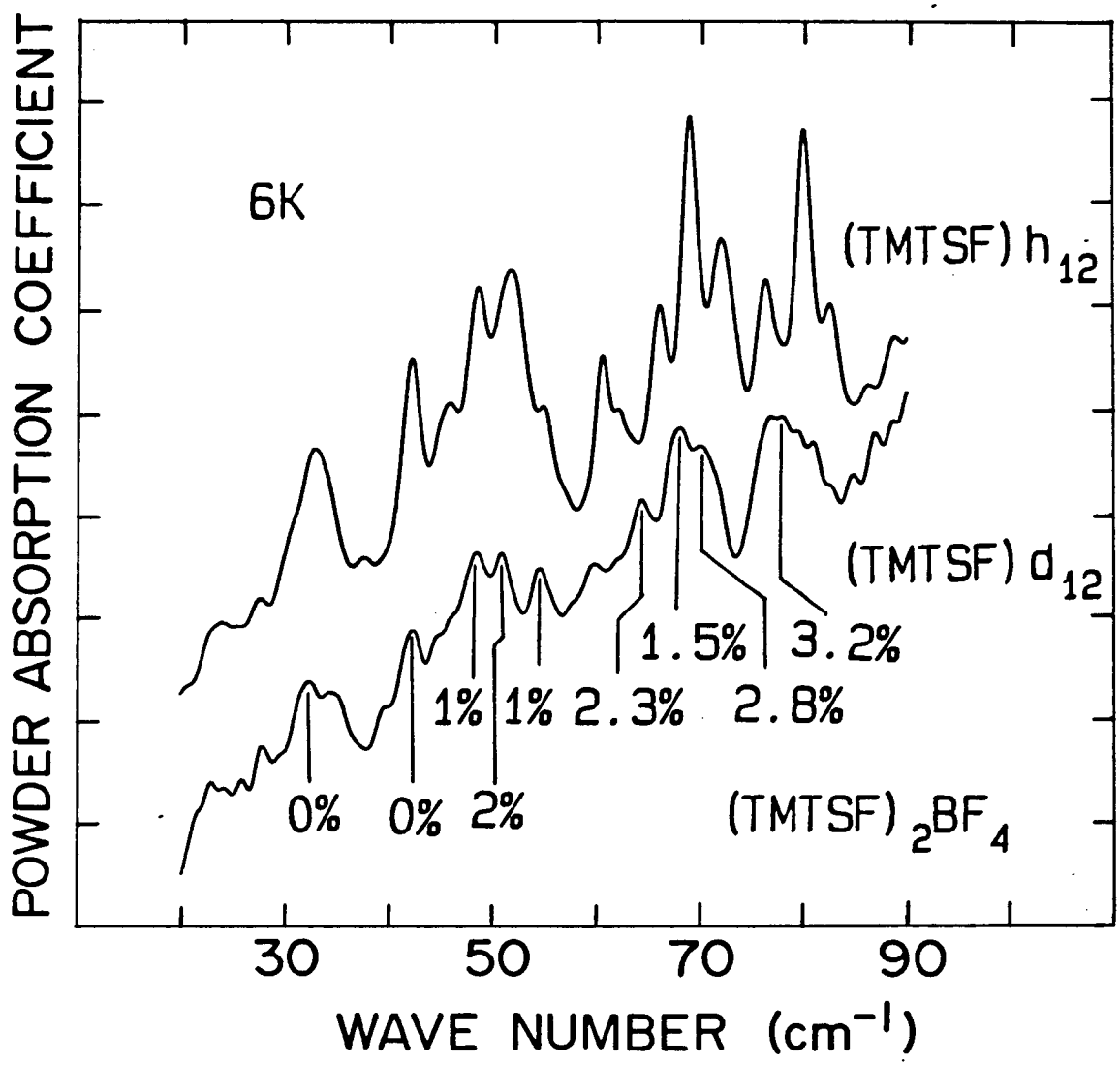

Figure 3-17 The 6-K powder absorption spectra αd of protonated and deuterated $(TMTSF)_2BF_4$ powders in Nujol on TPX mounts. The percentage decrease in wave number is indicated. The curves have been rescaled and offset for clarity. The deuterated spectra is of poorer quality because fewer crystals were used.

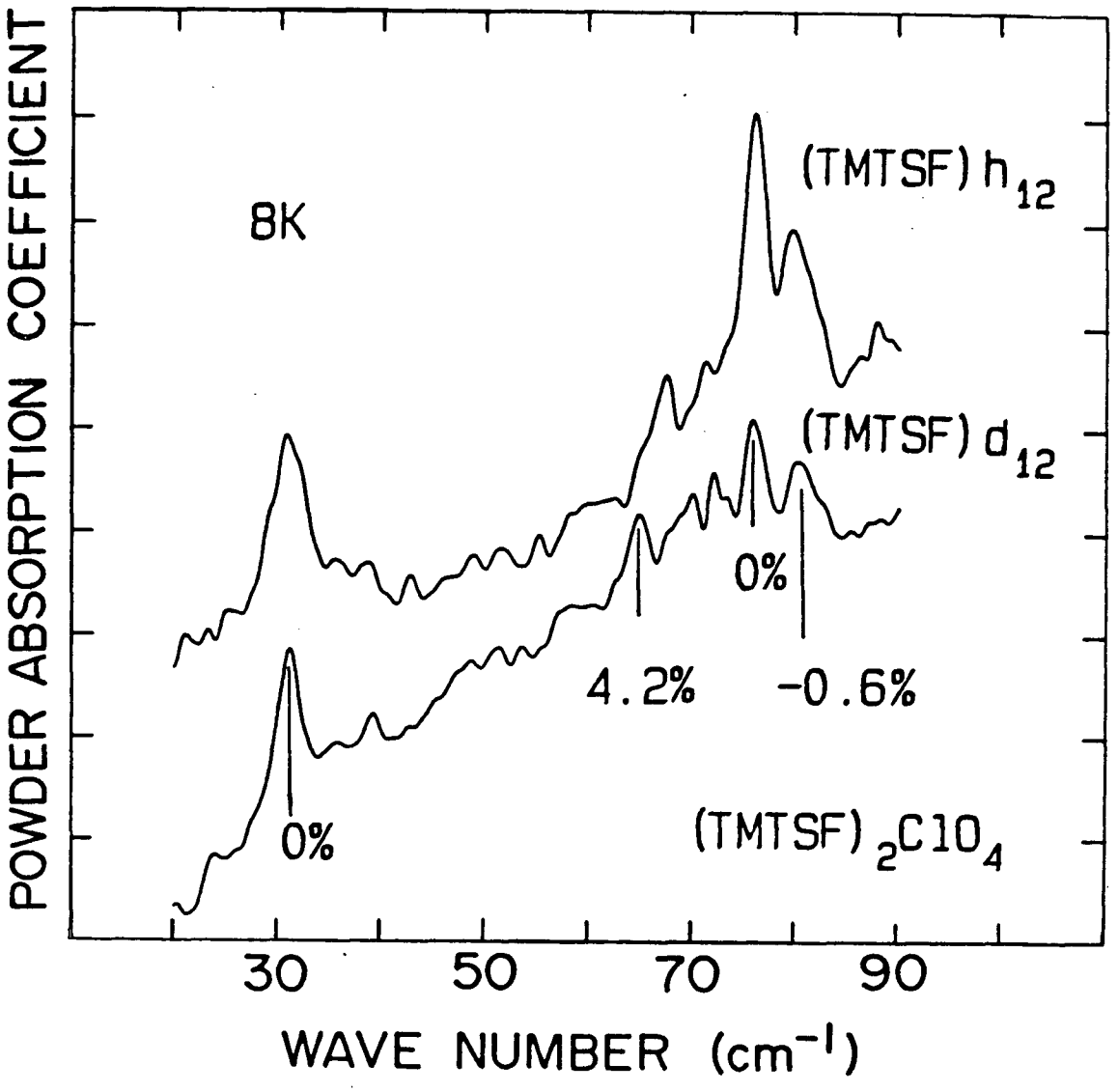

Figure 3-18 The 6-K powder absorption spectra αd of protonated and deuterated $(TMTSF)_2ClO_4$ powders in Nujol on TPX mounts. The percentage decrease in wave number is indicated. The curves have been rescaled and offset for clarity. The deuterated spectra is of poorer quality because fewer crystals were used.

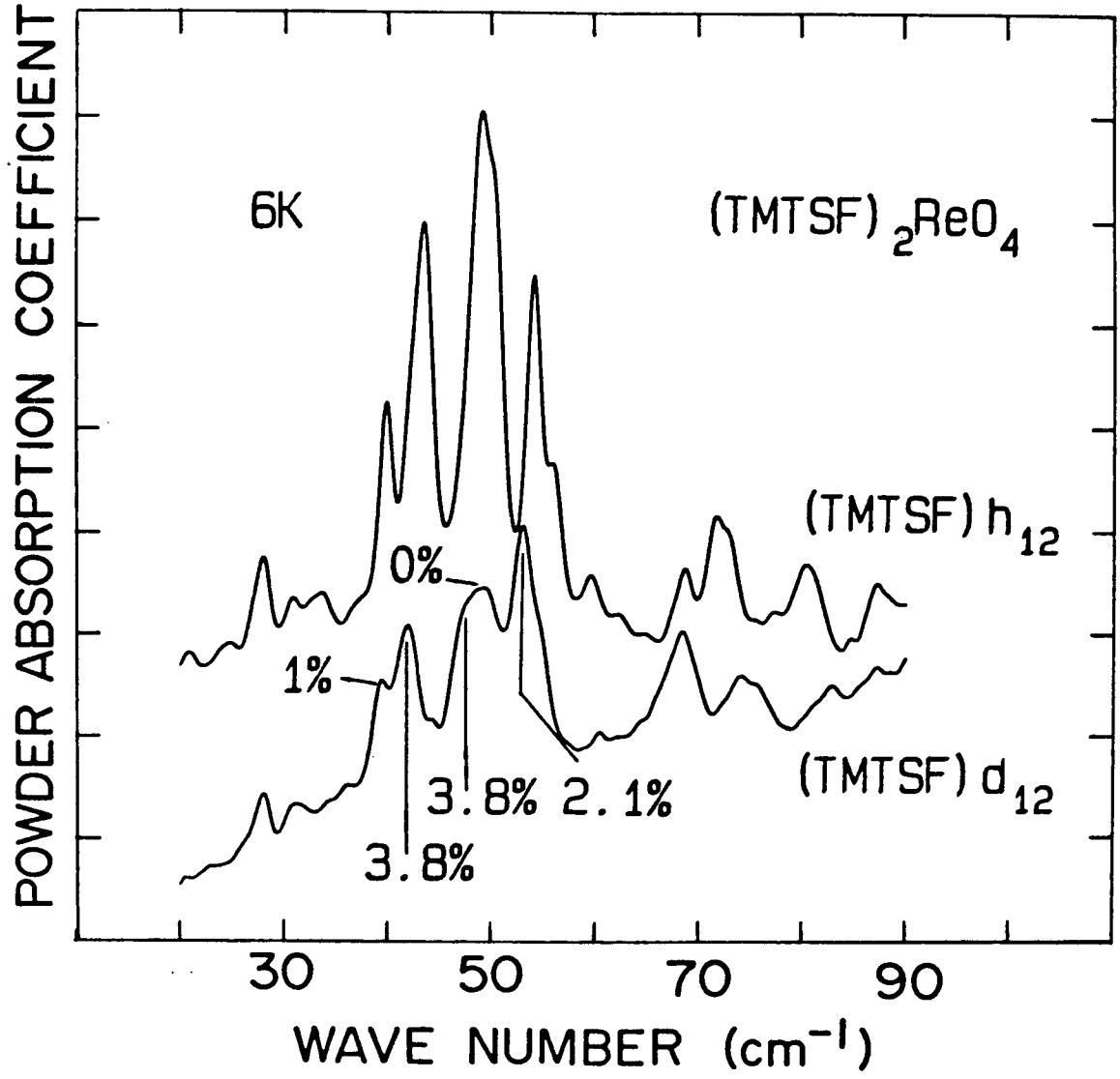

Figure 3-19 The 8-K powder absorption spectra αd of protonated and deuterated $(TMTSF)_2ReO_4$ powders in Nujol on TPX mounts. The percentage decrease in wave number is indicated. The curves have been rescaled and offset for clarity. The deuterated spectra is of poorer qulaity because fewer crystals were used.

no semiconducting gap appears. This means that the free-carrier absorption will not change very much. The curves in in Fig. 3–15 have therefore been displaced for clarity. Above T_{AO} only very broad features may be seen. At T_{AO}, however, four broad features are seen between 65 cm^{-1} and 85 cm^{-1}, and at 8 K an additional sharp feature at 31 cm^{-1}. Tentataive assignments based upon the isotope shifts shown in Fig. 3–18 and the calculations in Table III-I indicate that the internal $\nu_{72}(b_{3u})$ mode is found at $\sim$ 67 cm^{-1}, while the lines at 71 cm^{-1}, 76 cm^{-1} and 79 cm^{-1} are lattice modes. The poor resolution in the deuterated $(TMTSF)_2ClO_4$ spectra makes it really impossible to say which of the lattice modes is which. This portion of the spectrum (the three external modes and one internal mode) is just what we see in the octahedral anions.

The multiplets seen in $(TMTSF)_2BF_4$ and the shoulders in $(TMTSF)_2ReO_4$ below the anion-ordering transition are not as evident in $(TMTSF)_2ClO_4$. In the BF_4 and ReO_4 compounds the AO transition changes the unit cell from $a \times b \times c$ to $2a \times 2b \times 2c$[23]. The resulting superlattice is responsible for mapping many of the infrared inactive zone-boundary phonons back to the zone origin where some become infrared active. This would explain the extra structure which suddenly appears below T_{AO}. In the ClO_4 compound, the AO transition changes the unit cell from $a \times b \times c$ to $a \times 2b \times c$. This superlattice does not map as many of the zone-boundary phonons back to the zone origin, consequently the extra structure seen in BF_4 and ReO_4 is not as strong in the ClO_4 compound.

All of the samples were cooled slowly through the anion-ordering transition at a rate of < 1 K/min to ensure a relaxed state. The effect of rapid cooling into a quenched state was to broaden the lines seen in the spectra. This broadening is due to the anion disorder being frozen into the lattice.

One of the interesting features in the spectra of these compounds appears at 31 cm^{-1}. This feature is seen very strongly in the $\mathbf{E} \parallel \mathbf{b}'$ single crystal reflectivity spectrum of $(TMTSF)_2ClO_4$[54]. It appears in both polarizations and was first seen by

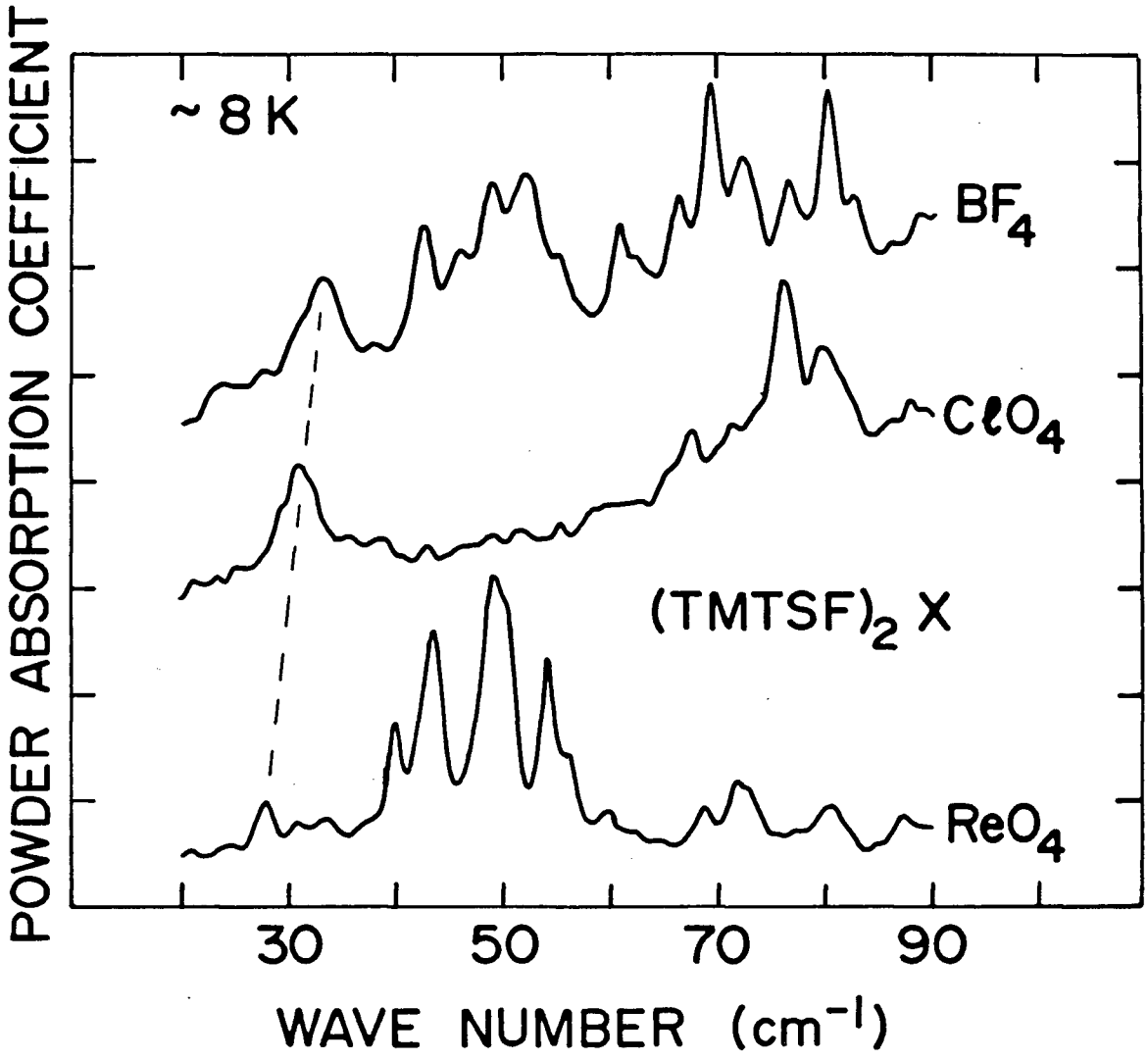

Figure 3-20 The low-temperature powder absorption coefficients of the three tetrahedral-anion compounds, rescaled and displaced for clarity. A dashed line joins the common "30 cm^{-1}" features. Notice also the large wavenumber shift of the four normal lines between the ClO_4 and the ReO_4 compounds.

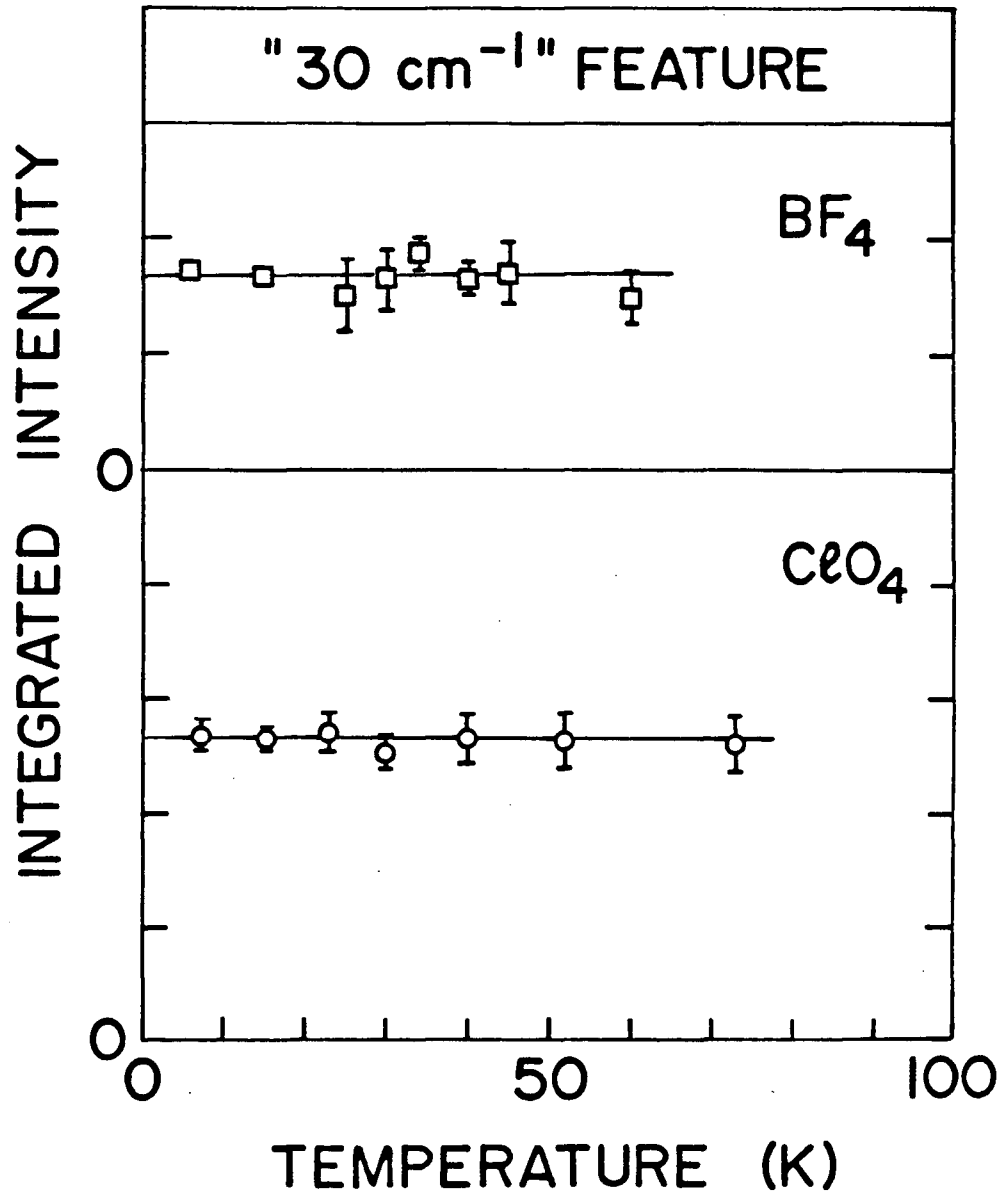

Figure 3-21 The integrated intensity of the "30 cm^{-1}" feature in the powder spectra of the BF_4 and ClO_4 compounds. The intensity is constant well beyond T_{AO}. The data were taken up to a temperature beyond which the feature was too broad to measure.

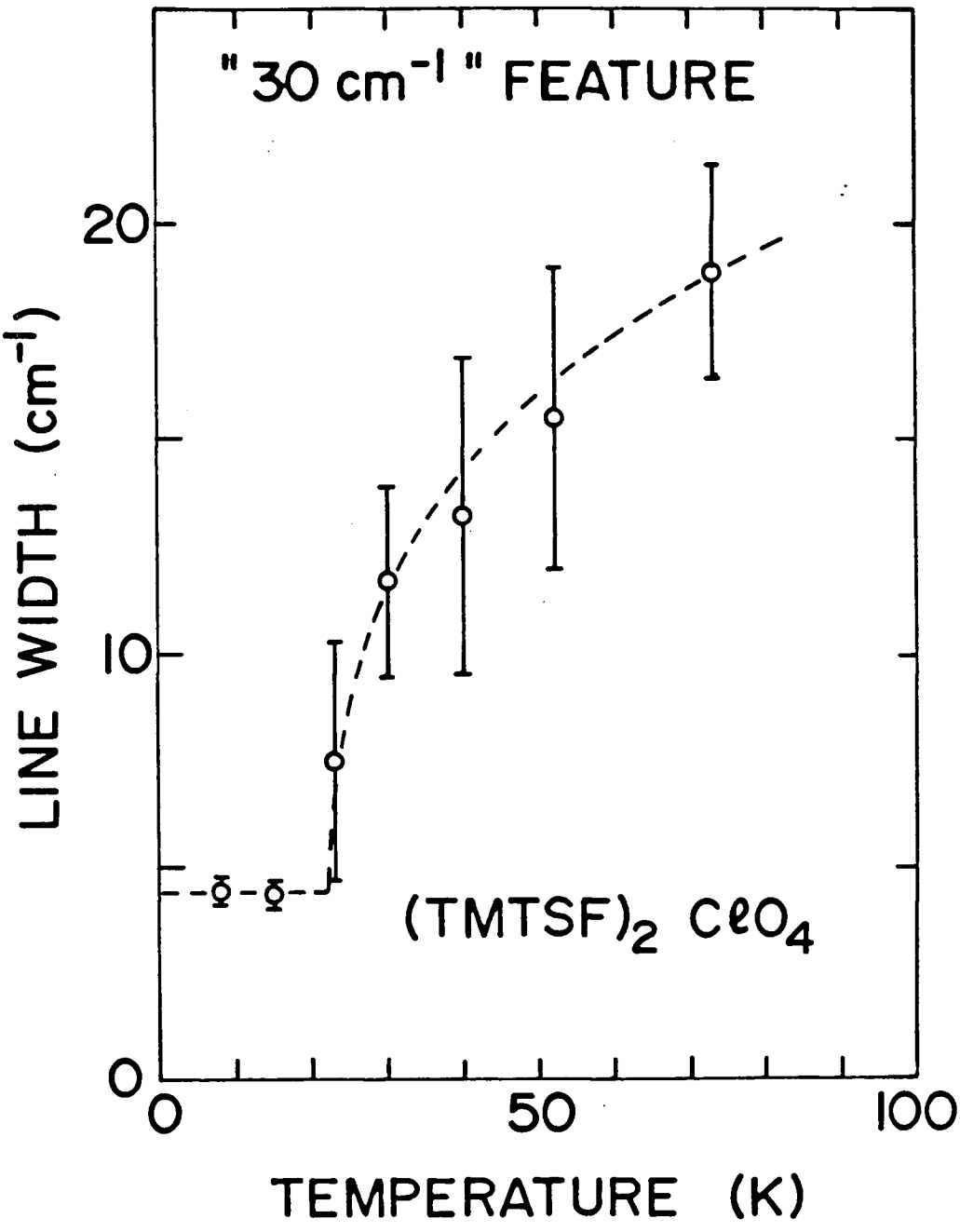

Figure 3-22 The full width at half-maximum of the "30 cm^{-1}" feature in the powder spectrum of $(TMTSF)_2ClO_4$. The line was fitted to a Lorentzian on a sloping background. Above T_{AO} the line is broadened quickly and was not a true Lorentzian. The error bars indicate this. The dashed line is drawn as a guide to the eye.

Ng, Timusk and Bechgaard[57] and by Challener, Richards and Green[53]. Ng, Timusk and Bechgaard found that for **E** || **a**, the feature at 2 K was reduced by the application of a magnetic field of 7 kG. The tunneling experiments on $(TMTSF)_2ClO_4$[36] indicated a pseudogap of 3–4 meV (24–32 cm^{-1}). Because the peak at 31 cm^{-1} (3.8 meV) falls into this range, and because of its magnetic field dependence, this feature was interpreted as evidence of ambient pressure fluctuating superconductivity in the material by Jerome. Challenar, Richards and Green[53] found no magnetic field dependence in the same feature, but it appears clear, both from their experimental procedure and from the structure seen in their spectra around 75 cm^{-1}, that they were measuring the **E**⊥**a** features, as seen in our spectra. Challenar *et al.* suggested that the feature was a coupled electron-phonon mode and suggested a comparision with other tetrahedral-anion compounds.

The results for the three tetrahedral-anion spectra are shown together in Fig. 3–20. A "30 cm^{-1}" feature is common to all three. Furthermore, if one plots the integrated intensity versus temperature, as seen in Fig. 3–21, one finds that it is constant up to a temperature beyond which it is too broad to measure. The width of the feature is constant below the anion-ordering temperature, but rises sharply above it and continues to grow with rising temperature, as shown in Fig. 3–22. This behavior may be explained in the following manner. The superlattice formed by the anion ordering leads to a zone-folding in which infrared inactive zone-boundary phonons are folded back to the origin and some become infrared active. This is the cause of the shoulders in the $(TMTSF)_2ReO_4$ and the multiplets in $(TMTSF)_2BF_4$ spectra. The "30 cm^{-1}" feature would appear to be a zone-boundary transverse acoustic phonon activated in this manner. It must couple very strongly with the electrons to have such a large oscillator strength. Above the anion-ordering transition, absorption would occur due to defect-induced one-phonon processes[85] along the entire phonon branch, proportional to the density of states. This would explain the sudden increase in width above the transition

temperature and the apparent downward shift in wave number. As the temperature and disorder increase, longer-wavelength phonons will contribute. The integrated intensity should be constant above and below T_{AO}, since the absorption mechanism is unchanged, only the way in which the momentum is conserved being different. Since the feature occurs near the same wave number for each compound, the zone-boundary transverse acoustic phonon would involve only the TMTSF molecules. The topic is treated in detail in Chapter 4, where simple dynamical models of the $(TMTSF)_2X$ salts are investigated. The results of Chapter 4 indeed show a low-lying zone-boundary transverse acoustic phonon which involves just the TMTSF molecules in the region of interest. If this is the case, however, then we might expect at least a 1.3% decrease in frequency upon deuteration (see Table III–I). Looking at the "30 cm^{-1}" feature, one sees that it shows no downward shift at all, and the perchlorate feature actually shifted up by $0.5 \pm 0.2\%$. On the other hand, two of the regular perchlorate lattice modes also had frequency shifts of 0% and an increase of $0.6 \pm 0.2\%$ respectively. Thus it would appear that a change in force constant is offsetting the mass increase. This is due to a decrease in the bond lengths in the deuterated methyl groups, which contracts the lattice. This is a common occurence in deuterated crystals.

The $\nu_{72}(b_{3u})$ internal mode for the tetrahedral anions is plotted with those of the octahedral anions in Fig. 3–13. While there is some uncertainly as to the positions of the internal modes in the tetrahedral-anion compounds, the figure shows that the different anions are changing the lattice parameters and the restoring forces on the TMTSF molecule.

3.3 Extended Measurements for $(TMTSF)_2X$ Compounds

Extended powder transmission measurements in the 100–300 cm^{-1} range were performed on $(TMTSF)_2AsF_6$ and $(TMTSF)_2SbF_6$ at 6 K and are shown in Fig. 3–23. Powder transmission measurements in the 100–400 cm^{-1} region have

been performed on quench cooled protonated and deuterated $(TMTSF)_2BF_4$ and $(TMTSF)_2ReO_4$ at 6 K and are shown in Fig. 3–24 and Fig. 3–25 respectively. These measurements were performed with a Golay detector and hence the resolution is only 8 cm^{-1}; the rest of the figures are the result of experiments performed with a bolometer on annealed samples giving a resolution of 2 cm^{-1}. Figure 3–26 shows a comparison of the powder absorption spectra of protonated $(TMTSF)_2BF_4$ and $(TMTSF)_2ReO_4$ in the 100–350 cm^{-1} region at 6 K. Figure 3–27 shows the powder absorption spectra of protonated and deuterated $(TMTSF)_2ReO_4$ in the 100–350 cm^{-1} region at 6 K and Fig. 3–28 shows the temperature dependence of the powder absorption spectra of $(TMTSF)_2ReO_4$ in the 100–350 cm^{-1} region from 205 K down to 6 K.

There is little structure visible in either the AsF_6 or the SbF_6 compound, except for a weak mode at 250 cm^{-1} and a strong feature at 290 cm^{-1} which is seen only in the SbF_6 compound. These measurements agree with the single-crystal measurements $\mathbf{E} \perp \mathbf{a}$[57]. The feature seen at 250 cm^{-1} has been observed in the $TMTSF^+$ powder spectra[64], where it was assigned to a $\nu_{35}(b_{1u})$ or a $\nu_{53}(b_{2u})$ mode. It is characteristic for these internal modes to shift in the presence of anions, thus it is difficult to assign this resonance to either a $\nu_{35}(b_{1u})$ or a $\nu_{53}(b_{2u})$ mode. The $\nu_5(f_{2g})$ SbF_6 mode was measured at 294 cm^{-1}, but it is usually infrared inactive. Unlike the internal modes of the TMTSF molecule, we do not expect a large change in the internal modes of the anions, thus it is unlikely that a different anion mode is being observed. The ν_5 mode may be activated by disorder effects or coupling with electrons. Figure 3–29 shows the low-energy modes of the octahedral anions, and Table III–III below it shows the frequencies of these modes for the PF_6^-, AsF_6^- and SbF_6^- octahedral anions.

For the octahedral anions, a correlation table may be constructed to show how the molecular point group changes when the anion is placed into a solid geometry, as is shown in Fig. 3–30.

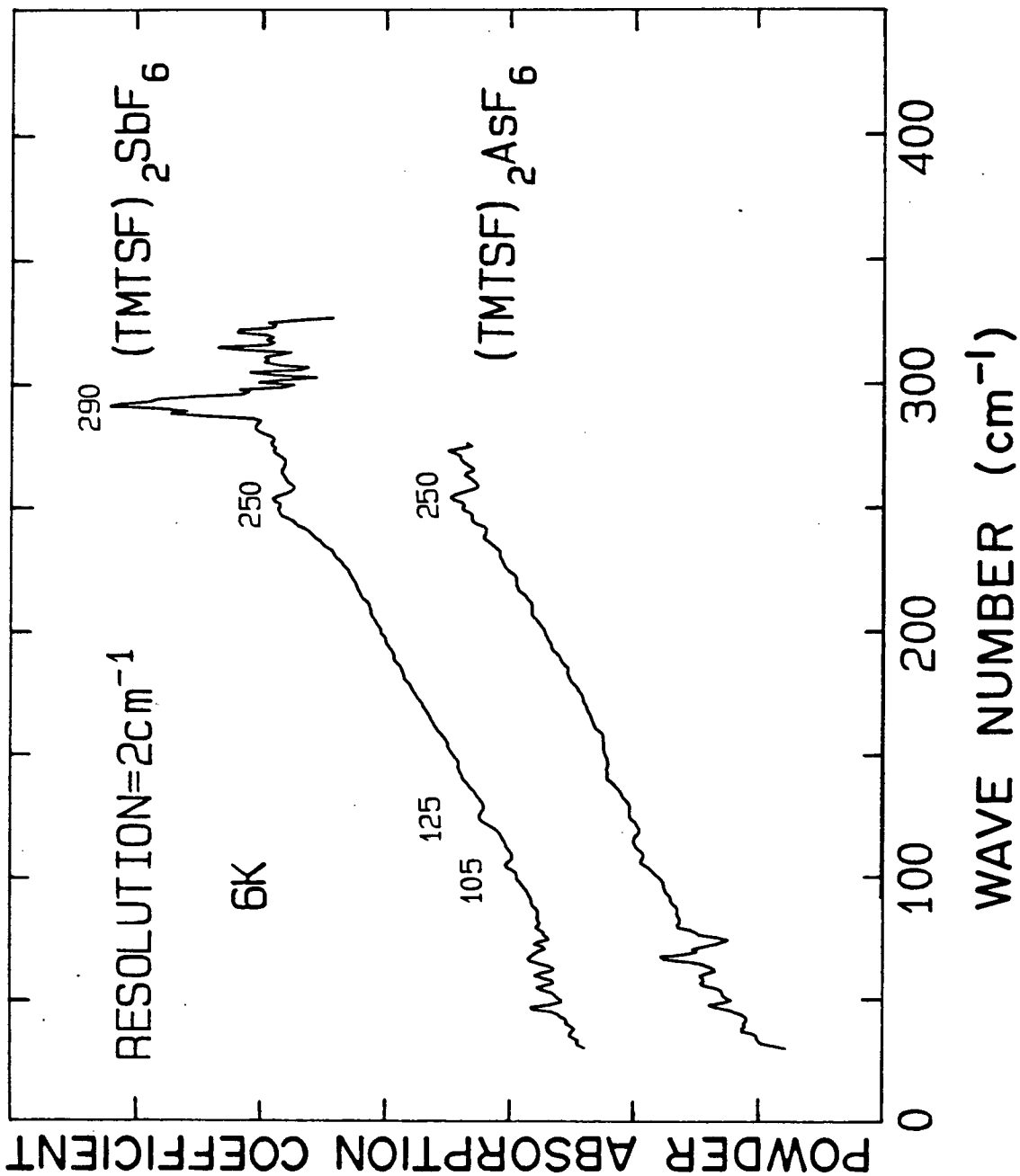

Figure 3-23 The 6-K powder absorption coefficient αd of $(TMTSF)_2AsF_6$ powder from 25–275 cm^{-1}, and $(TMTSF)_2SbF_6$ powder from 25–325 cm^{-1}, in Nujol on TPX mounts. The curves have been rescaled and offset for clarity.

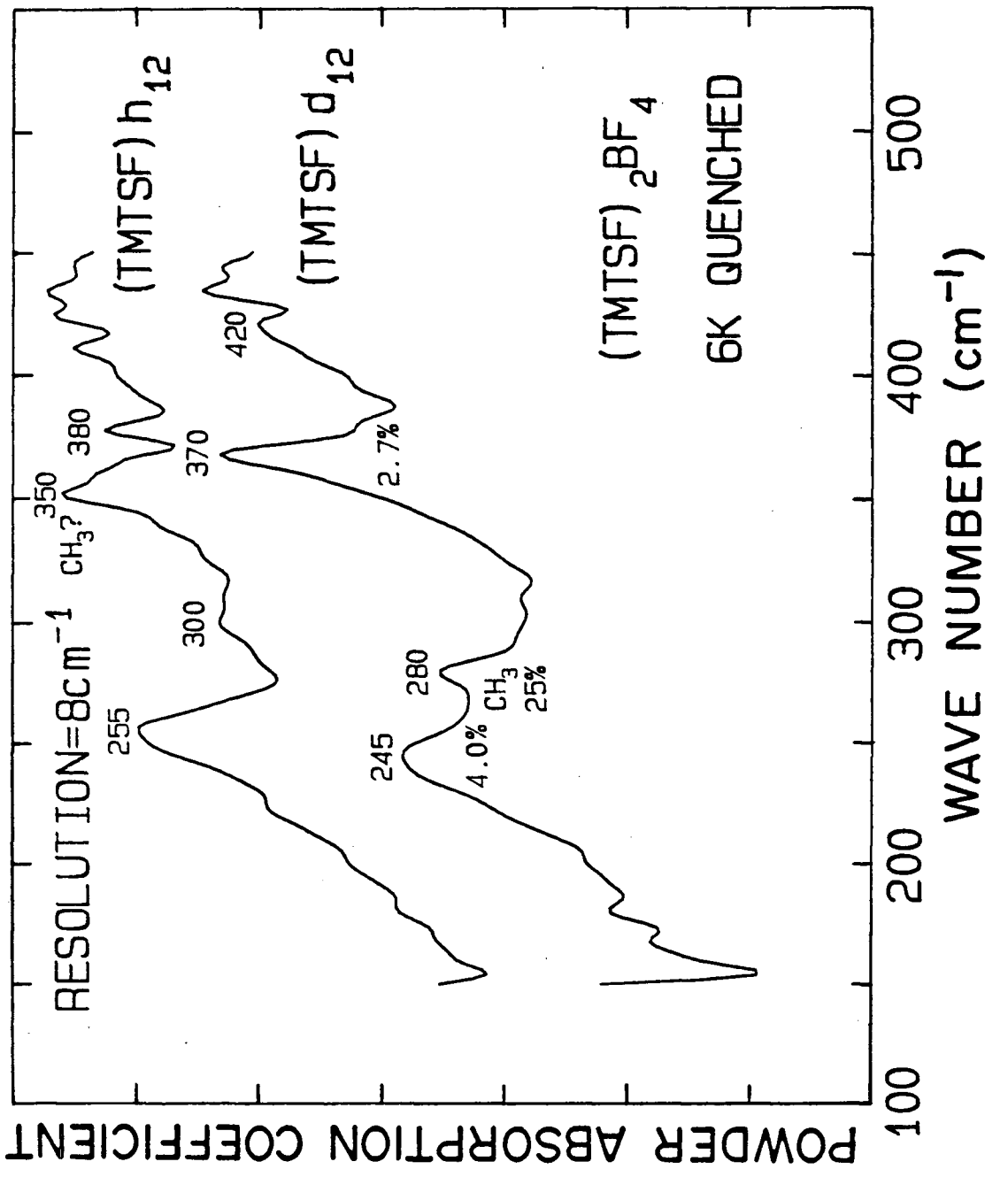

Figure 3-24 The 6-K protonated and deuterated powder absorption spectra for quench cooled $(TMTSF)_2BF_4$ powders in Nujol on TPX mounts. The positions of the peaks and the percentage shifts upon deuteration are indicated. The curves have been shifted and rescaled for clarity. Cooling through T_{AO} was > 10 K/min.

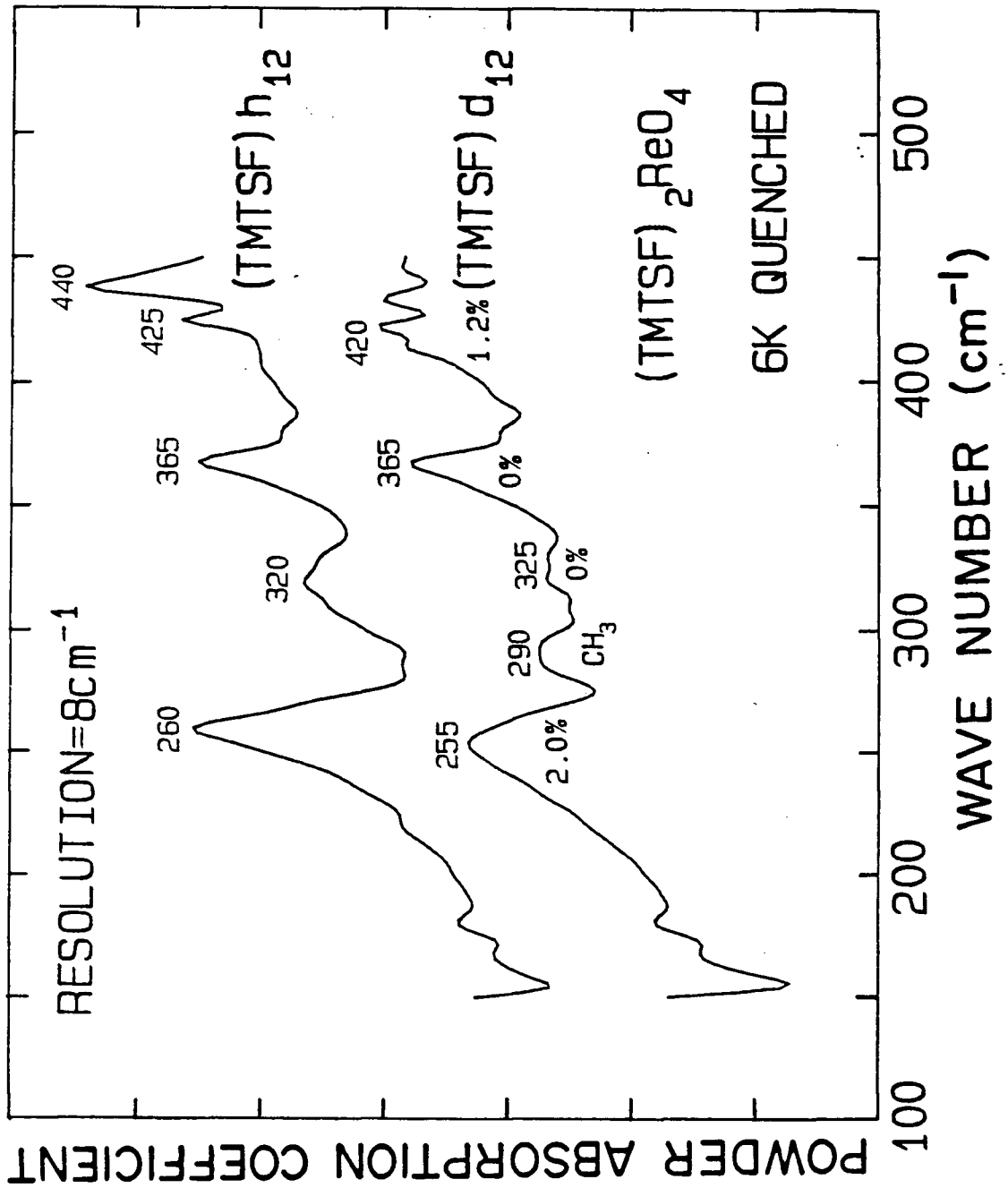

Figure 3-25 The 6-K protonated and deuterated powder absorption spectra for quench cooled $(TMTSF)_2ReO_4$ powders in Nujol on TPX mounts. The positions of the peaks and the percentage shifts upon deuteration are indicated. The curves have been shifted and rescaled for clarity. Cooling through T_{AO} was > 10 K/min.

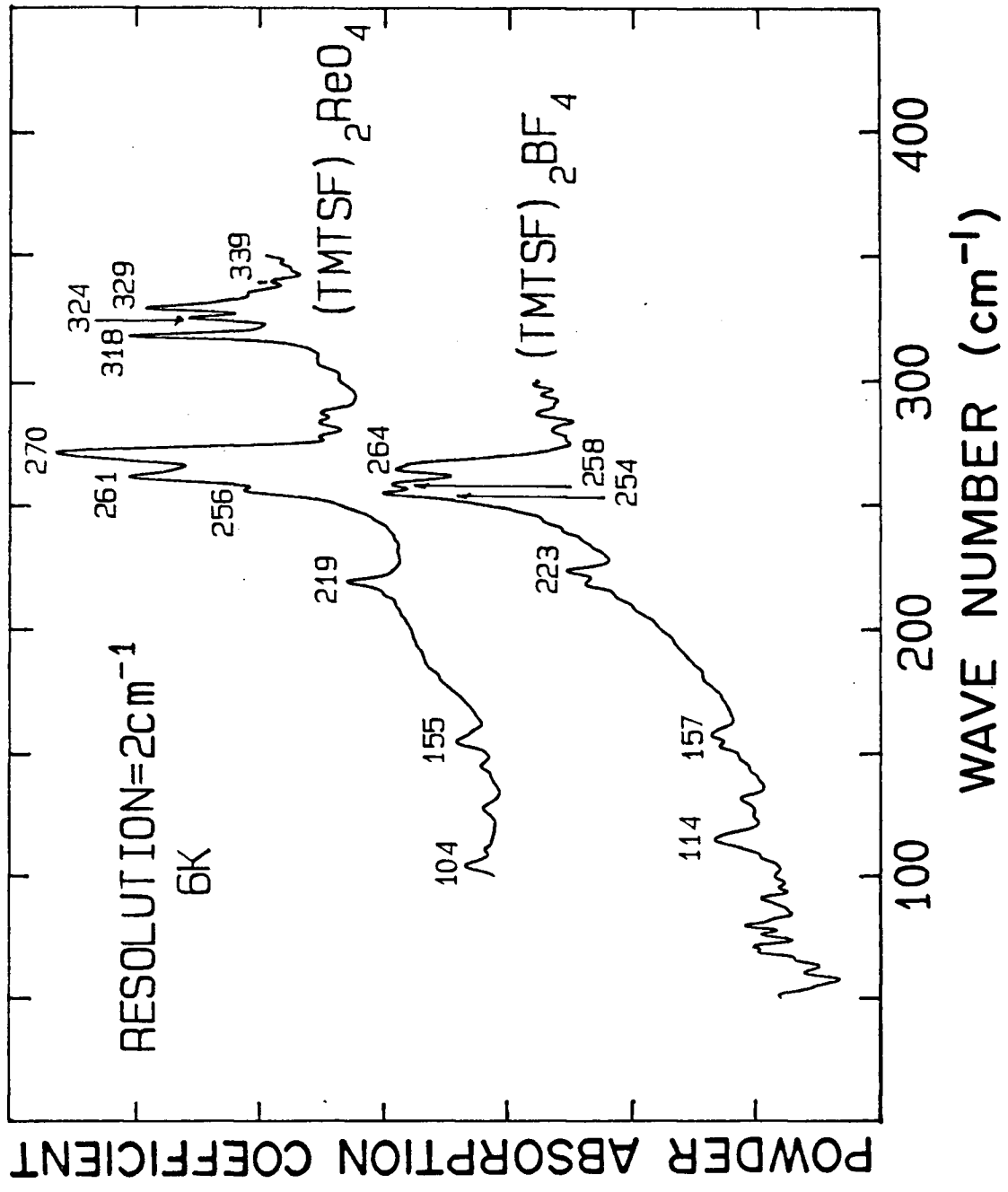

Figure 3-26 A comparison of the powder absorption spectra αd (in arbitrary units) of protonated and deuterated $(TMTSF)_2BF_4$ and $(TMTSF)_2ReO_4$ powders in Nujol on TPX mounts at 6 K in the 100–300 cm^{-1} region. The peaks have been labelled. The curves have been offset and rescaled for clarity. Cooling through the respective T_{AO}'s was < 1 K/min.

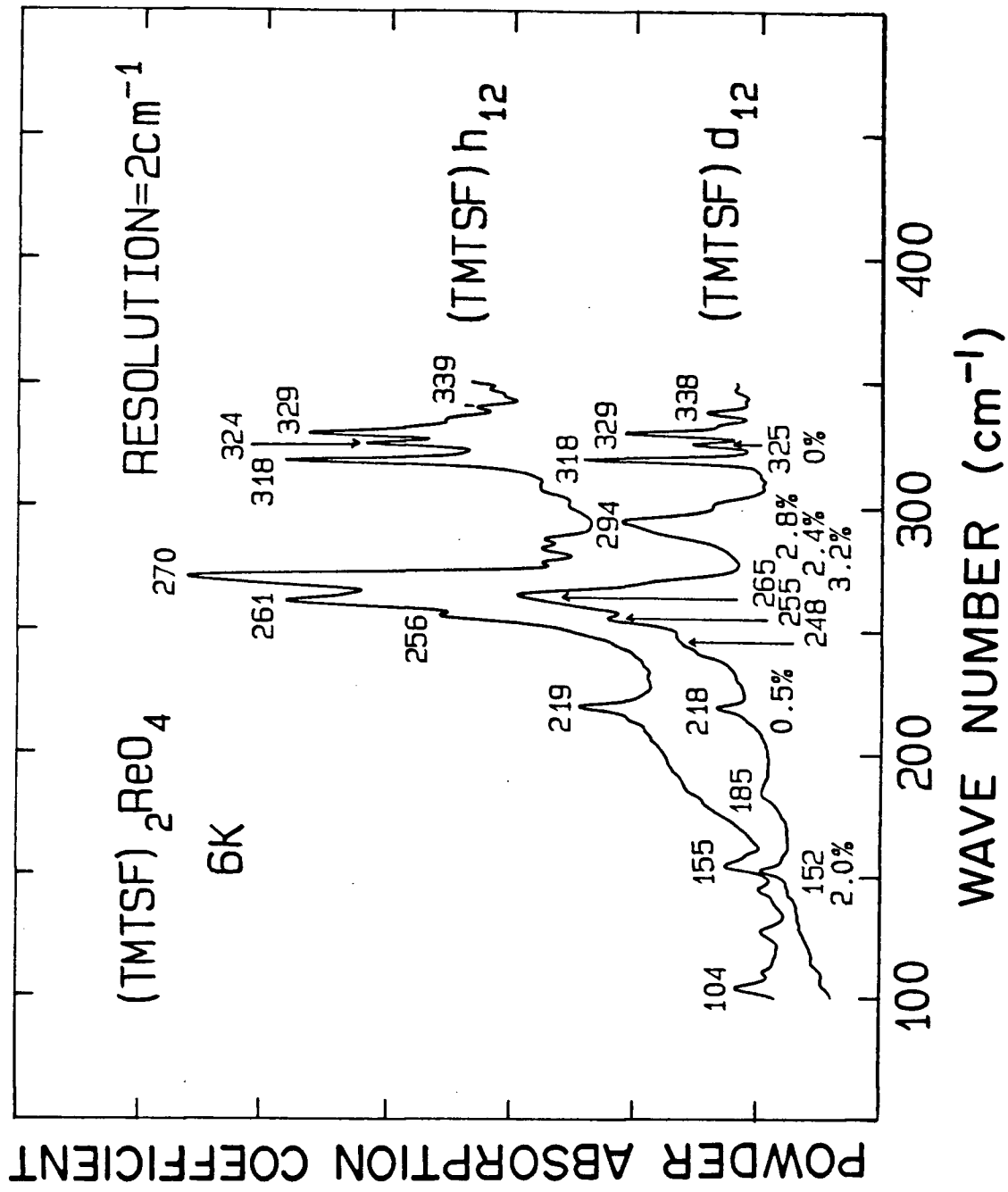

Figure 3-27 The 6-K powder absorption spectra of protonated and deuterated $(TMTSF)_2ReO_4$ powders in Nujol on TPX mounts. The positions of the peaks and the percentage shifts upon deuteration are indicated. The curves have been rescaled and offset for clarity. Cooling through T_{AO} was at < 1 K/min.

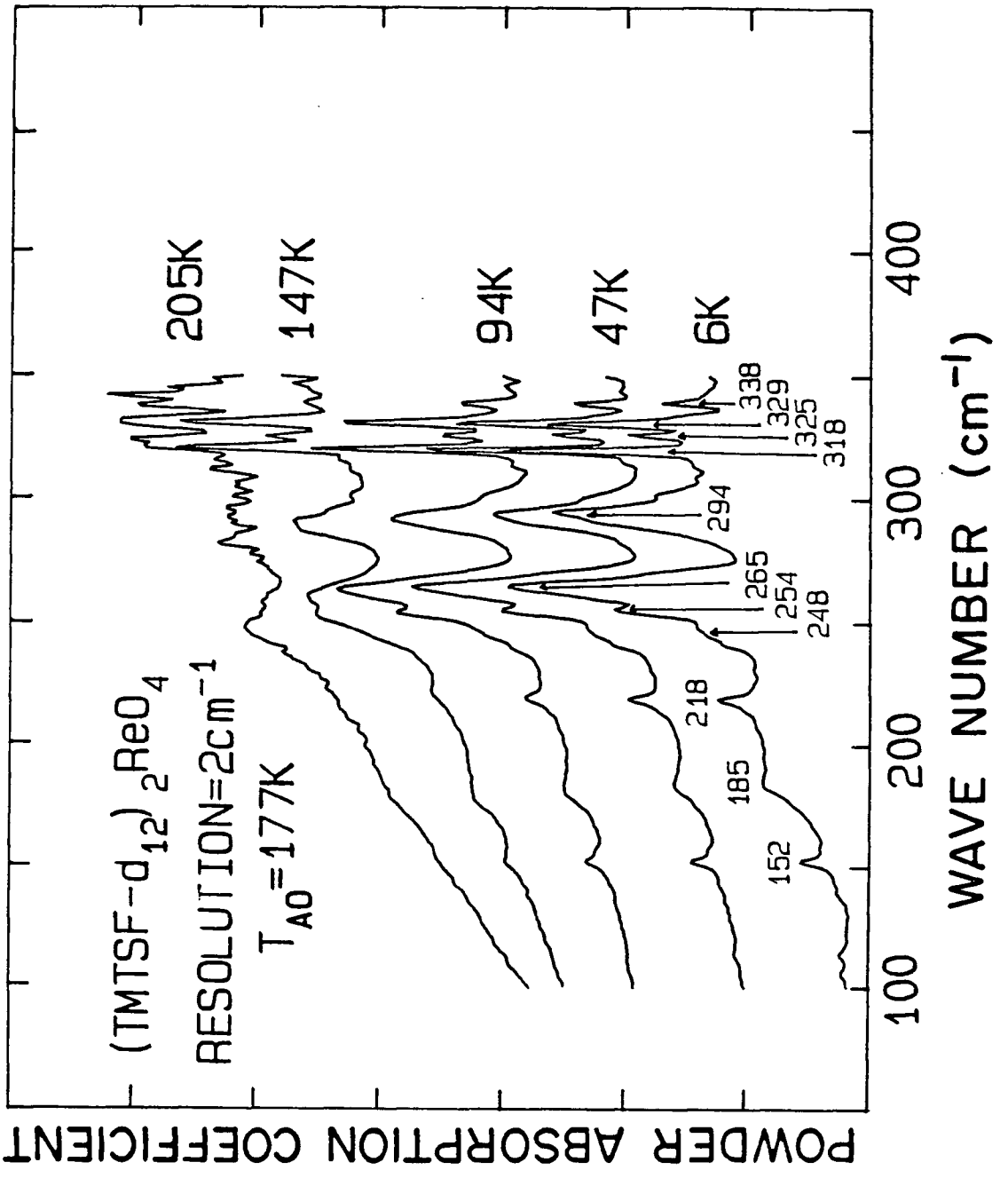

Figure 3-28 The powder absorption coefficient αd of deuterated $(TMTSF)_2ReO_4$ powder in Nujol on a TPX backing. The anion-ordering transition temperature is shown, and the peaks are labelled. The curves have the same scale, but have been displaced for clarity. Cooling through T_{AO} was at < 1 K/min.

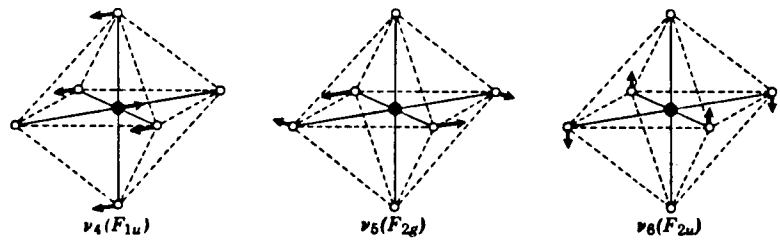

Figure 3-29 The low-energy normal modes of vibration of the octahedral anions[86]. There are a total of six normal modes for the octahedral anions.

Table III–III[a]

Low-energy internal vibrations of octahedral anions

Anion	$\nu_4(f_{1u})$ (cm^{-1})	$\nu_5(f_{2g})$ (cm^{-1})	$\nu_6(f_{2u})$ (cm^{-1})
PF_6^-	555	465	402 or 329
AsF_6^-	392	372	363
SbF_6^-	350	294	208

[a] Ref. 86: K. Nakamoto, *Infrared and Raman Spectra of Inorganic and Coordination Compounds, 3rd ed.*, John Wiley & Sons, New York (1963).

Above the MI transition in the ReO_4 compound some features are observable at $\sim$ 260 cm^{-1} and $\sim$ 320 cm^{-1}. As the temperature is lowered, these features sharpen and grow into three lines in the 250–270 cm^{-1} region, four lines in the 320–340 cm^{-1} region, and new features at 152 cm^{-1}, 185 cm^{-1}, 218 cm^{-1} and 294 cm^{-1} (the feature at 294 cm^{-1} is very strong, but appears only in the deuterated spectra). Features at 365 cm^{-1} and 425 cm^{-1} are also observed. The spectra in this work have a higher resolution than those of Bozio *et al.*[63], and also extend to lower

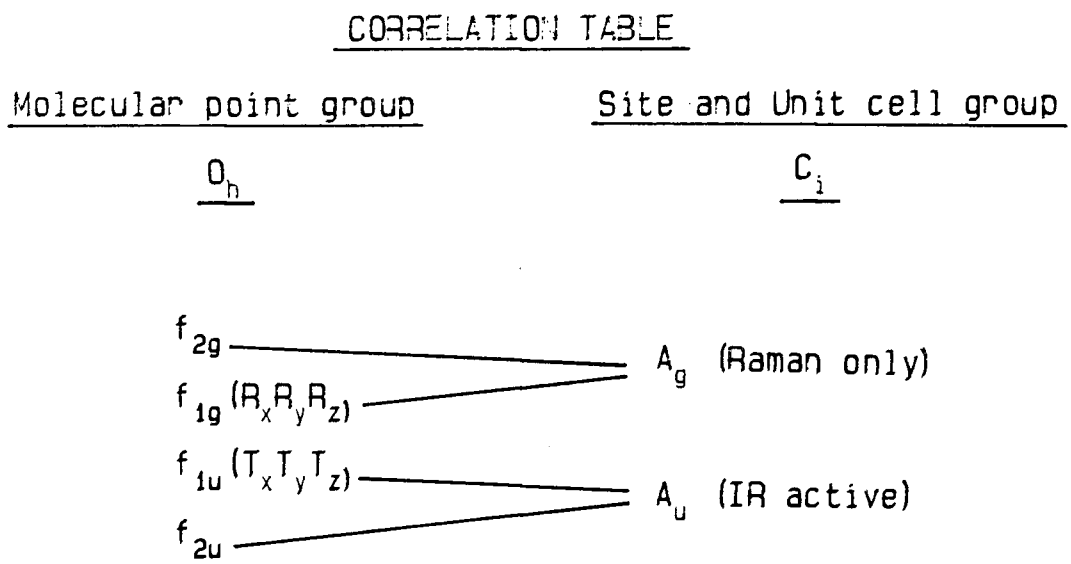

Figure 3-30 The correlation table for the molecular point group and the site and unit cell group of the octahedral anions. This table determines which modes will become infrared active.

energies. In addition, we also have spectra of the deuterated compounds which aid in the determination of vibrational modes. Similar features are seen in the BF_4 compound at 157 cm^{-1}, three lines in the 250–270 cm^{-1} region, a very strong feature at 280 cm^{-1} (which occurs only in the deuterated spectra), and two features at 370 cm^{-1} and 420 cm^{-1}.

The four sharp lines at 318 cm^{-1}, 324 cm^{-1}, 329 cm^{-1} and 339 cm^{-1} in the ReO_4 compound are not observed to shift upon deuteration, nor are they observed in the BF_4 compound. The $\nu_4(f_2)$ mode of the ReO_4^- anion is measured at 331 cm^{-1}. Figure 3–31 shows some of the low-frequency vibrations of the tetrahedral anions, and Table III–IV below it gives the frequencies of these modes for the BF_4^-, ClO_4^- and ReO_4^- tetrahedral anions.

Figure 3-31 The low-energy normal modes of vibration of the tetrahedral anions[86]. There are a total of four normal modes for the tetrahedral anions.

Table III–IV[a]

Low-energy internal vibrations of tetrahedral anions

Anion	$\nu_2(e)$ (cm^{-1})	$\nu_4(f_2)$ (cm^{-1})
BF_4^-	360	533
ClO_4^-	459	625
ReO_4^-	331	331

[a] Ref. 86: K. Nakamoto, *Infrared and Raman Spectra of Inorganic and Coordination Compounds, 3rd ed.*, John Wiley & Sons, New York (1963).

The extended measurements on the $(TMTSF)_2X$ compounds have been placed in Table III-V, along with the results of a calculation of the low-energy in-plane internal modes of the $TMTSF^+$ molecule[64], and the experimental results of powder measurements on $TMTSF^+$[64], $(TMTSF)_2PF_6$[63] and $(TMTSF)_2ReO_4$[63]. These results are preliminary, and no definite assignments have been made. There are some arguments, however, for suspecting certain modes. In the powder measurements

Table III–V

Low-Energy Internal Vibrations

TMTSF $^+$ calculated[a]	TMTSF$^+$ observed[b]	$TMTSF_2PF_6$, SbF_6, AsF_6 (8K)	$(TMTSF)_2ReO_4$ (15K)	$(TMTSF\text{-}h_{12})_2ReO_4$ (6K)[d]	$(TMTSF\text{-}d_{12})_2ReO_4$ (6K)[d]	$(TMTSF\text{-}h_{12})_2BF_4$ (6K)[d]	$(TMTSF\text{-}d_{12})_2BF_4$ (6K)[d]
$\nu_9(a_g)$ 453	452		436	425, 440	420	420	420
$\nu_{10}(a_g)$ 312	317			365	365	365	350-380
$\nu_{53}(b_{2u})$ 309						300	
$\nu_{35}(b_{2u})$ 300	298					300	
$\nu_{11}(a_g)$ 279	285		261, 271	270	265	264	
$\nu_{36}(b_{1u})$ 265	273	254[c], 250[d]		260	255	255	245
$\nu_{65}(b_{3g})$ 183					185		
$\nu_{12}(a_g)$ 137				155	152	157	
$\nu_{54}(b_{2u})$ 55		55-60[d]					
Anion $\nu_4(f_2)$			329(ReO_4)	329	329		
			318(ReO_4)	318	318		
Methyl group?					294		280
Out-of-plane					218		
g mode?							
Anion $\nu_5(f_{2g})$		290(SbF_6)[d,e]					

[a] Ref. 64: M. Meneghetti *et al.*, *J. Chem. Phys.*, **80**, 6210 (1984).

[b] Solution spectra a_g modes.

[c] Ref. 63: R. Bozio and C. Pecile, *Solid State Commun.*, **41**, 905 (1981).

[d] This work.

[e] Seen in Ng, Eldridge single-crystal measurements also.

underlined = seen to be activated at low temperatures.

on $TMTSF^+$ made by Meneghetti *et al.*[64], all of the low-energy a_g modes were observed, thus, an effort was made to identify these modes in our spectra as well.

One feature which is particularly interesting is the strong resonance at 280 cm^{-1} and 294 cm^{-1} in the deuterated BF_4 and ReO_4 compounds. Neither of these features appears in the protonated spectra of these compounds, indicating that this mode may be a low-energy torsional mode involving the methyl groups of the TMTSF molecule. For such a mode, $I_p/I_d \sim 2/1$, where I is the moment of inertia along the torsional axis, which is the C–C bond going into the methyl group. This being the case, we would expect

$$\frac{\nu_p}{\nu_d} = \sqrt{\frac{I_d}{I_p}} \sim 1.414 \qquad (3-9)$$

a 41% shift, which would place this feature at ~ 420 cm^{-1} in the protonated spectra. The spectra in Fig. 3–24 and 3–25 are very noisy in this region, and it is impossible to locate this feature. This calculation is probably not too accurate anyway, since we have ingnored the interaction of the anions with the methyl groups. (When we discussed the anion-ordering transitions of the BF_4 and ReO_4 anions, the anion-cation interaction, and hence the anion-methyl interaction, was very strong).

The four lines clustered around ~ 330 cm^{-1} in the the ReO_4 compound are probably associated with the $\nu_4(f_2)$ mode, and possibly the $\nu_2(e)$ mode. As Table III-IV shows, the $\nu_2(e)$ and $\nu_4(f_2)$ modes are degenerate at 331 cm^{-1} for a free ReO_4^- ion, however, in the solid the degenercy may be removed and a splitting of this line may occur. The $\nu_4(f_2)$ line may also experience splitting due to isotope effects. The ν_4 mode involves the rhenium atom as well as the oxygen atoms, and since the natural abundance of ^{187}Re:^{185}Re is 63%:37%, then it is possible that this mode may be split. We expect the ν_4 feature to be stronger in the infrared than the ν_2 mode, since the ν_2 mode is activated by the disorder or low site symmetry of the lattice. The lines at 318 cm^{-1} and 329 cm^{-1} are very strong and are probably

the $\nu_4(f_2)$ mode. The splitting may be caused by isotope effects, or the folding of zone-boundary internal modes back to the origin (the same mechanism thought to be responsible for the activation of the the low-energy "30 cm^{-1}" feature in this compound). The weaker lines at 324 cm^{-1} and 339 cm^{-1} may be the $\nu_2(e)$ mode being activated, or could be associated with the splitting of the $\nu_4(f_2)$ mode.

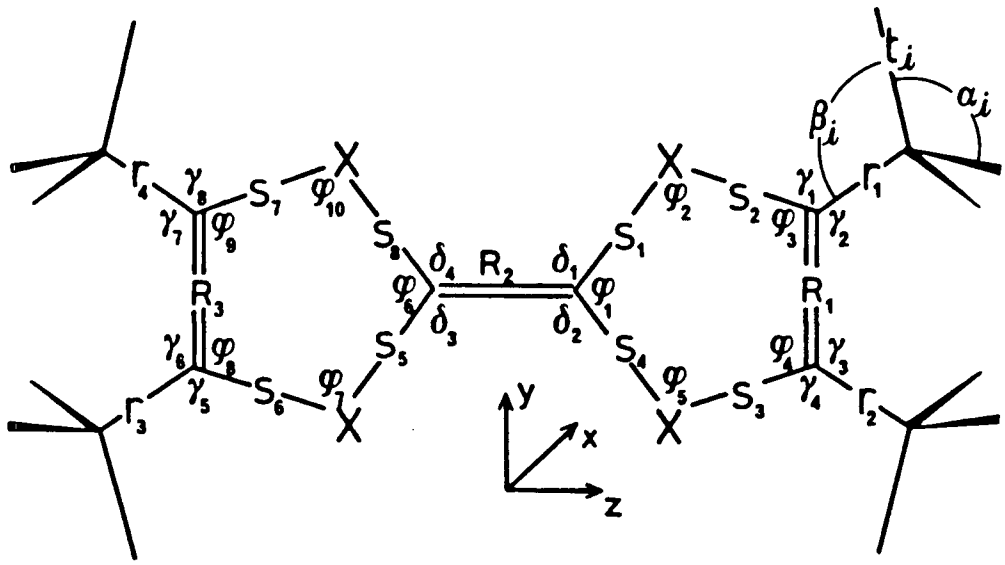

Figure 3-32 The symbolic designation of the internal coordinate system used in the normal coordinate calculation of the vibrational states of the TMTSF and $TMTSF^+$ molecules[64]. Note that all the coordinates are in the *yz*-plane.

The calculations performed by Meneghetti *et al.*[64] for the internal modes of the TMTSF and $TMTSF^+$ molecules do not predict the shifts upon deuteration for the modes; however, they do provide information about the potential energy associated with each coordinate involved in a particular vibration. The symbolic

designation of the internal coordinate system used in the normal coordinate calculation of the vibrational states of TMTSF and$TMTSF^+$ molecules is shown by Fig. 3–32.

The feature at 365 cm^{-1} is seen in both the BF_4 and ReO_4 spectra, and does not appear to shift upon deuteration, however, there is a lot of noise in the BF_4 spectra in this region. A possible candidate might be the $\nu_{10}(a_g)$ mode, which has $s_1 s_1(53)$ and $\gamma_k \gamma_k(32)$; that is 53% of the potential energy of the vibration is associated with the s_1 coordinate, and 32% is assiciated with the γ_k coordinate. This means that the methyl groups will be active in this mode, as is indicated by Fig. 3–33 which shows the modes for four low-energy a_g vibrations.

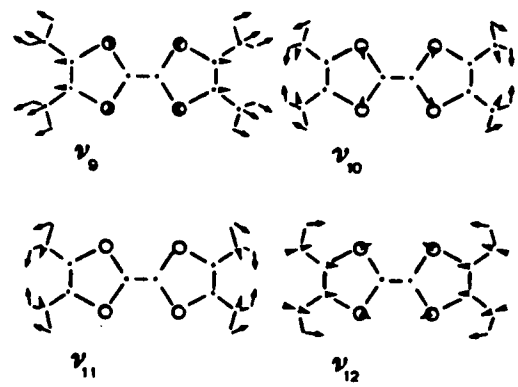

Figure 3-33 Atomic displacement vectors for the totally symmetric (a_g) modes of neutral TMTSF. Note that all of these modes involve the methyl groups.

Since there is apparently no shift upon deuteration, and this mode indicates that there should be one, this mode may be a candidate for an out-of-plane mode. A more detailed examination of this region will have to be made before any positive assignments can be made.

CHAPTER 4

LATTICE DYNAMICS OF $(TMTSF)_2X$: SIMPLE MODELS

4.1 Introduction

Having measured some of the infrared-active low-frequency lattice and internal modes, it would be meaningful to construct simplified models to understand better the dynamical behavior of these complex compounds.

In particular we suspect that the "30 cm^{-1}" feature may be a low-lying zone-boundary transverse acoustic phonon which is being activated by zone-folding due to the formation of a superlattice in the tetrahedral-anion salts. Simple models can determine which eigenfrequencies and eigenmodes correspond to the low-lying acoustic mode, and give information about its behavior. Using sound velocity measurements the force constants may be calculated. This allows us to calculate the frequency of the acoustic mode at the zone boundary.

4.2 One-dimensional Model of $(TMTSF)_2X$

We begin with the simplest conceptual picture of the $(TMTSF)_2X$ system, that is a one-dimensional lattice with a three-point basis. The construction of the system and of the cell in reciprocal space is shown in Fig. 4–1. The anion of mass m alternates along the chain with two TMTSF molecules of mass M. The force constant springs K joining the masses are all equal. The unit cell is of size a.

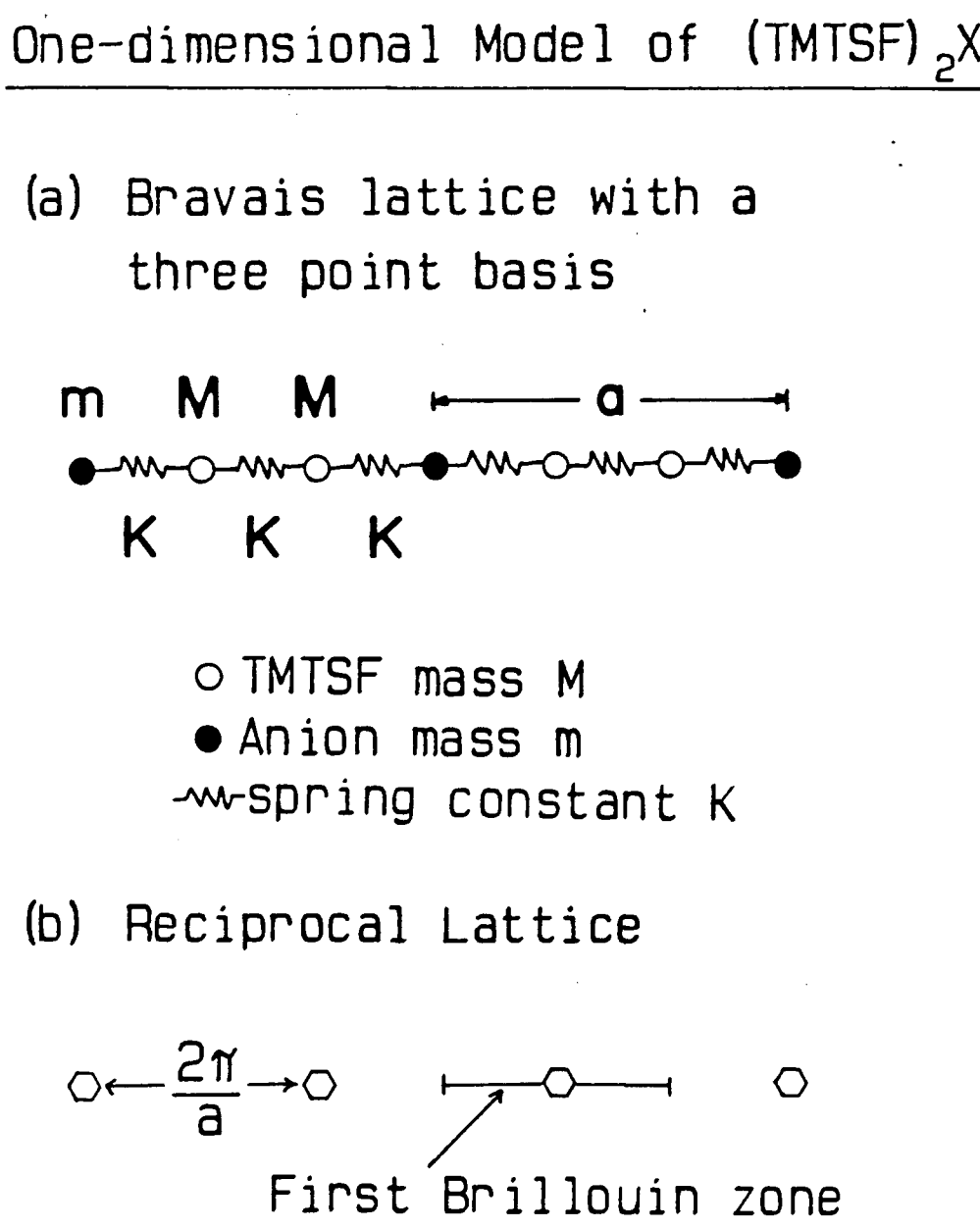

Figure 4-1 Linear system for $(TMTSF)_2X$. (a) The unit cell for the lattice. The anions are represented by the mass m, and the TMTSF molecules by the mass M. Here a is the lattice constant. The force constant springs K are all equal in this particular model. (b) The reciprocal lattice for a one-dimensional model.

Consider the equation of motion for a mass M at a point $\mathbf{R}$ in the lattice[87]

$$M\frac{\partial^2 \mathbf{u_R}}{\partial t^2} = \sum_{\mathbf{R}'} \mathbf{K}^{jj'}(\mathbf{R}' - \mathbf{R}) \cdot \mathbf{u}_{\mathbf{R}'} \qquad (4-1)$$

where $\mathbf{u_R}$ is the displacement of M about $\mathbf{R}$, $\mathbf{R}'$ locates the nearest neighbours. The two indices j and j' locate the force constants in the unit cell. In other words, for each postion j in the unit cell the index j' points to each of the other points in the unit cell and labels the force constant springs joining them. Because the masses in the unit cell may not be equal, j also indexes the mass, m_j. Looking for harmonic solutions to this equation of the form

$$\mathbf{u}(\mathbf{q}, t) \sim e^{(\mathbf{q}\cdot\mathbf{a} - \omega t)} \qquad (4-2)$$

where $\mathbf{q}$ is the wave vector, then equation 4–1 becomes

$$\omega^2 m_j \mathbf{u_R} = \sum_{\mathbf{R}'} \mathbf{K}^{jj'}(\mathbf{R}' - \mathbf{R}) \cdot \mathbf{u}_{\mathbf{R}'} \qquad (4-3)$$

To generate solutions which are defined in reciprocal space (since we expect the solutions to involve the periodicity of the lattice), equation 4–3 must be changed from the direct lattice representation to one in reciprocal space. Using Fourier transforms, we define the following relations

$$U(\mathbf{q})e^{i\mathbf{q}\cdot\mathbf{R}} = \mathbf{u_R}, \qquad (4-4)$$

$$\mathbf{K}^{jj'}(\mathbf{q}) = \sum_{\mathbf{R}'} \mathbf{K}^{jj'}(\mathbf{R}' - \mathbf{R}) e^{i\mathbf{q}\cdot(\mathbf{R}'-\mathbf{R})}. \qquad (4-5)$$

substituting equations 4–4 and 4–5 into equation 4–3 gives the result

$$\sum_{j'} \left\{ \mathbf{K}^{jj'}(\mathbf{q}) - \omega^2 m_j \delta_{jj'} \right\} U_{j'}(\mathbf{q}) = 0. \qquad (4-6)$$

For our simple one-dimensional system by assuming the non-trivial solution (non-zero displacements). then the summations must be zero and equation 4–6 becomes

$$\sum_{j} \left\{ \mathbf{K}_{\alpha}^{jj'} - \omega^2 \mathrm{m}_j \delta_{jj'} \right\} = 0. \qquad (4-7)$$

Here α indicates the lattice direction. By evaluating $\mathbf{K}^{jj'}(\mathbf{q})$ in equation 4–5 and substituting the results into equation 4–7, we can determine the system of coupled linear differential equations. The secular equation is

$$\begin{vmatrix} 2K - \omega^2 m_1 & -Ke^{iqa/3} & -Ke^{-iqa/3} \\ -Ke^{-iqa/3} & 2K - \omega^2 m_2 & -Ke^{iqa/3} \\ -Ke^{iqa/3} & -Ke^{-iqa/3} & 2K - \omega^2 m_3 \end{vmatrix} = 0. \qquad (4-8)$$

Evaluating the determinant results in

$$\begin{aligned} &\omega^6(m_1 m_2 m_3) - \omega^4(m_1 m_2 + m_2 m_3 + m_3 m_1) \\ &+3K^2\omega^2(m_1 + m_2 + m_3) - 2K^3(1 - \cos(qa)) = 0. \end{aligned} \qquad (4-9)$$

From the model, $m_1 = m$ (m is the anion mass) and $m_2 = m_3 = M$ (M is the mass of the TMTSF molecule). Only those phonons at the zone origin and at the zone boundary are of real interest. Hence, we want to find solutions for $\mathbf{q} = 0$ and $\mathbf{q} = \frac{\pi}{a}$ in equation 4–9

$$\omega_1(0) = \sqrt{\frac{3K}{M}} \qquad (4-10a)$$

$$\omega_2(0) = \sqrt{\frac{2K}{m_r}} \qquad (4-10b)$$

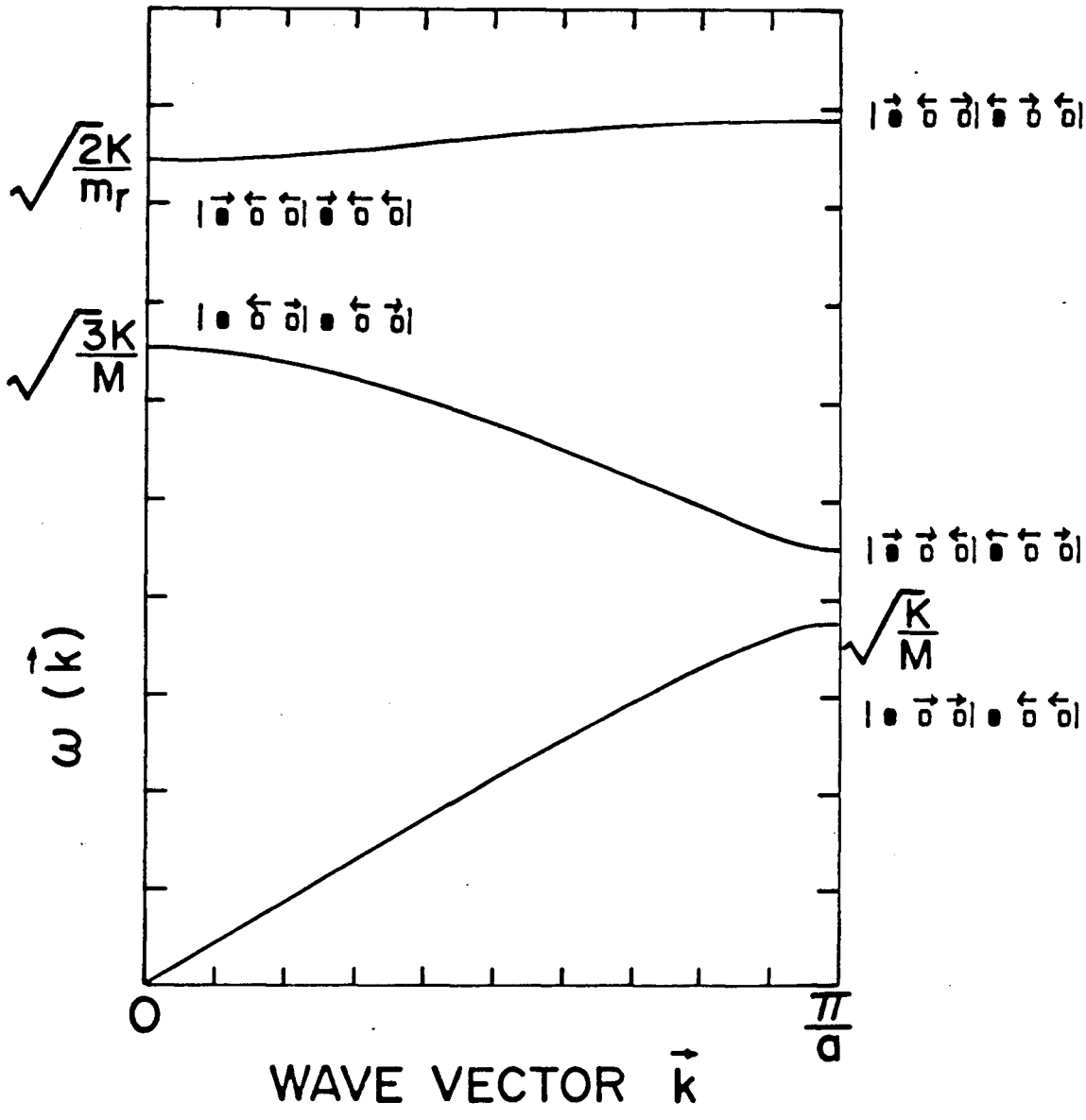

Figure 4-2 The frequency dispersion curves for the one-dimensional model shown with the eignemodes at the zone origin and at the zone boundary. The reduced mass, m_r, is defined as $m_r = 1/m + 1/2M$. Note that the zone-boundary acoustic phonon involves just the TMTSF molecules.

Where the reduced mass $m_r = 1/m + 1/2M$. For $\mathbf{q} = \frac{\pi}{a}$, the zone boundary of the first brillouin zone in reciprocal space

$$\omega_1(\frac{\pi}{a}) = \sqrt{\frac{K}{M}} \qquad (4-11a)$$

$$\omega_2(\frac{\pi}{a}) = \sqrt{\frac{K}{2mM}(2M + 3m - \sqrt{4M^2 + 9m^2 - 4mM}} \qquad (4-11b)$$

and

$$\omega_3(\frac{\pi}{a}) = \sqrt{\frac{K}{2mM}(2M + 3m + \sqrt{4M^2 + 9m^2 - 4mM}} \qquad (4-11c)$$

The band structure for this model calculated for the values m=1, M=2, and K=4, and shown along with the eigenmodes at the zone origin and at the zone boundary in Fig. 4–2. The zone-boundary acoustic phonon involves just the TMTSF molecules. This will be examined in more detail in the two-dimensional model.

4.3 Two-dimensional model of $(TMTSF)_2X$

One can argue from a physical point of view that since the **ab** plane does not differ greatly from the **ac** plane the two-dimensional analysis reveals almost as much as a three-dimensional analysis would. The configuration of the unit cell that we have chosen is shown in Fig. 4–3, along with the unit cell in reciprocal space and the first Brillouin zone, This model represents the **ab** plane, so we can now identify a stack direction (**a**-axis) and a transverse direction (**b**-axis). The calculation has been set up to allow each of the masses in the unit cell to be different. The TMTSF molecules are represented by m_1 and m_2, although $\mid m_1 \mid = \mid m_2 \mid$. The TMTSF molecules are aranged in stacks, and are seperated by a distance a along the **a** or y direction. Each stack or chain is seperated from the next by a distance of $2a$. The anions of mass m_3 are placed between the stacks at regular intervals, a distance a away from the chain along the **b** or x direction. The anions repeat with spacing

$2a$ along the x and y directions, interacting with every other TMTSF molecule in the stack, in this way forming their own sublattice. The TMTSF molecules are connected by a force constant spring K_1, and the anions are joined to alternate TMTSF molecules by force constant springs K_2. The unit cell is of size $2a \times 2a$.

Once again we must find the set of coupled equations, this involves solving equation 4–7, only there are now two lattice directions α and β so that with this new degree of freedom the 3×3 determinant will become a 6×6 determinant for the two-dimensional model.

$$\begin{vmatrix} 2K_2 - \omega^2 m_1 & 0 & -2K_2\cos(q_x a) & 0 & 0 & 0 \\ 0 & -\omega^2 m_2 & 0 & 0 & 0 & 0 \\ -2K_2\cos(q_x a) & 0 & 2K_2 - \omega^2 m_3 & 0 & 0 & 0 \\ 0 & 0 & 0 & 2K_1 - \omega^2 m_1 & -2K_1\cos(q_y a) & 0 \\ 0 & 0 & 0 & -2K_1\cos(q_y a) & 2K_1 - \omega^2 m_2 & 0 \\ 0 & 0 & 0 & 0 & 0 & -\omega^2 m_3 \end{vmatrix} = 0. \tag{4-12}$$

Notice that in this particular model we have completely decoupled the x and y systems, thus the 6×6 matrix can be reduced to two 3×3 matrices. The first determinant corresponds to $\alpha = x$ and $\beta = x$, and the second determinant to $\alpha = y$ and $\beta = y$. If we define the reduced mass μ_{ij} as

$$\mu_{ij} = \frac{m_i m_j}{m_i + m_j}. \tag{4-13}$$

Solving for the first determinant gives the eigenmodes with a q_x dependence

$$\omega_1(\mathbf{q}) = \sqrt{\frac{K_2}{\mu_{13}} - \sqrt{\frac{K_2^2}{\mu_{13}^2} - \frac{4K_2^2\sin^2(q_x a)}{m_1 m_3}}} \tag{4-14a}$$

$$\omega_2(\mathbf{q}) = \sqrt{\frac{K_2}{\mu_{13}} + \sqrt{\frac{K_2^2}{\mu_{13}^2} - \frac{4K_2^2\sin^2(q_x a)}{m_1 m_2}}} \tag{4-14b}$$

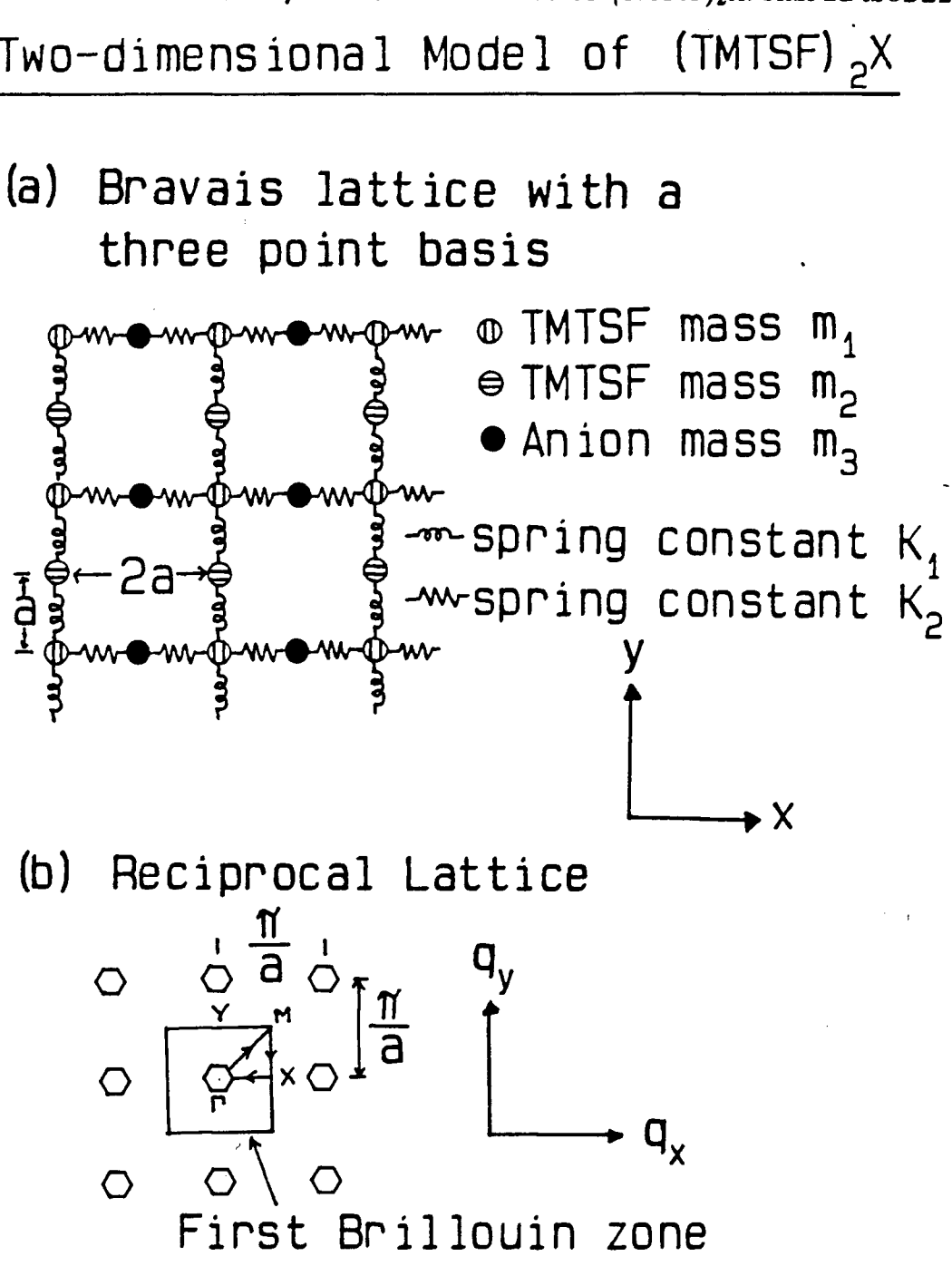

Figure 4-3 Two-dimensional system for $(TMTSF)_2X$. (a) The anions of mass m_3 are joined to alternate TMTSF molecules of mass $|\ m_1\ | = |\ m_2\ |$ by force constant springs K_2. The TMTSF molecules are joined by force constant springs K_1. The unit cell is of size $2a \times 2a$. The coordinate system for the direct lattice is shown. (b) The reciprocal lattice for the two-dimensional system and the first brillouin zone. The coordinate system for the reciprocal lattice is shown.

Recall that for a cubic lattice in real space, the reciprocal lattice will also be cubic with its axes oriented in the same directions as the axes in the direct lattice. Thus, these branches represent the modes which propogate along the x-direction, transverse to the stacks. Solving the second determinant gives the eigenfrequencies with a q_y dependence

$$\omega_3(\mathbf{q}) = \sqrt{\frac{K_1}{\mu_{12}} - \sqrt{\frac{K_1^2}{\mu_{12}^2} - \frac{4K_1^2 \sin(q_y a)}{m_1 m_2}}} \qquad (4-14c)$$

$$\omega_4(\mathbf{q}) = \sqrt{\frac{K_1}{\mu_{12}} + \sqrt{\frac{K_1^2}{\mu_{12}^2} - \frac{4K_1^2 \sin(q_y a)}{m_1 m_2}}} \qquad (4-14d)$$

These branches represent the modes which are polarized along stacks. Note that one of the effects of decoupling the x and y systems is to give eigenmodes which are completely polarized along the x- or y-direction in the direct lattice.

The transverse and longitudinal modes usually refer to the motion of the ions with respect to the direction of the wave vector. Because this model represents two uncoupled one-dimensional models, we would have no transverse modes in the true sense. Instead, we simply denote the direction of the ions as either being in the transverse (x) direction or longitudinal (y) direction. If we consider that the frequency dispersion curves are those for a a wave vector in the q_y direction, then this is equivalent to a model with more degrees of freedom where true transverse modes would exist; using this simple trick we can consider the phonons in our simple model as being truly transverse or longitudinal.

The frequency dispersion curves are calculated using the estimates $m_1 = m_2 = 1$, $m_3 = \frac{1}{2}$, $K_1 = 1$ and $K_2 = \frac{1}{4}$, based on the mass ratios and the relative coupling strengths, along the paths $\Gamma \rightarrow \mathrm{M} \rightarrow \mathrm{X} \rightarrow \Gamma$ and $\Gamma \rightarrow \mathrm{M} \rightarrow \mathrm{Y} \rightarrow \Gamma$ in reciprocal space and are shown in Fig. 4–4 and Fig. 4–5 respectively.

The frequency dispersion curves at M shows a transverse acoustic phonon and a longitudinal acoustic phonon present, along with the longitudinal and transverse

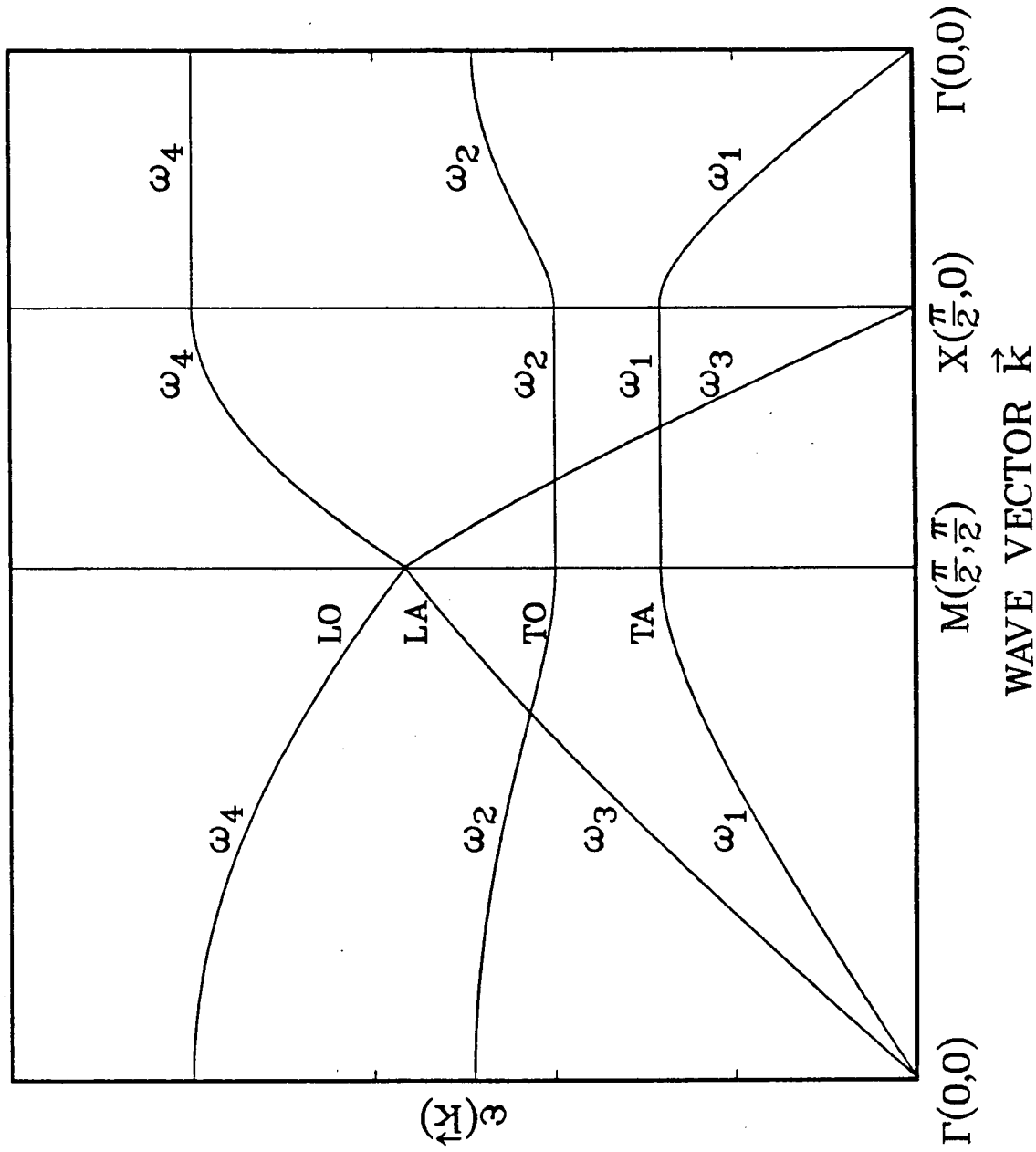

Figure 4-4 The frequency dispersion curves for the two-dimensional model for the path $\Gamma \rightarrow M \rightarrow X \rightarrow \Gamma$. The branches have been labelled according to which solution they correspond to. Along the path M→X the longitudinal acoustic mode goes to zero, while the transverse acoustic mode remains constant, as does the transverse optic mode. The transverse modes depend only on q_x, and the longitudinal modes only depend on q_y; thus if either one of these variables is constant (as is the case along M→X and X→ Γ), then the corresponding mode will not change along the path.

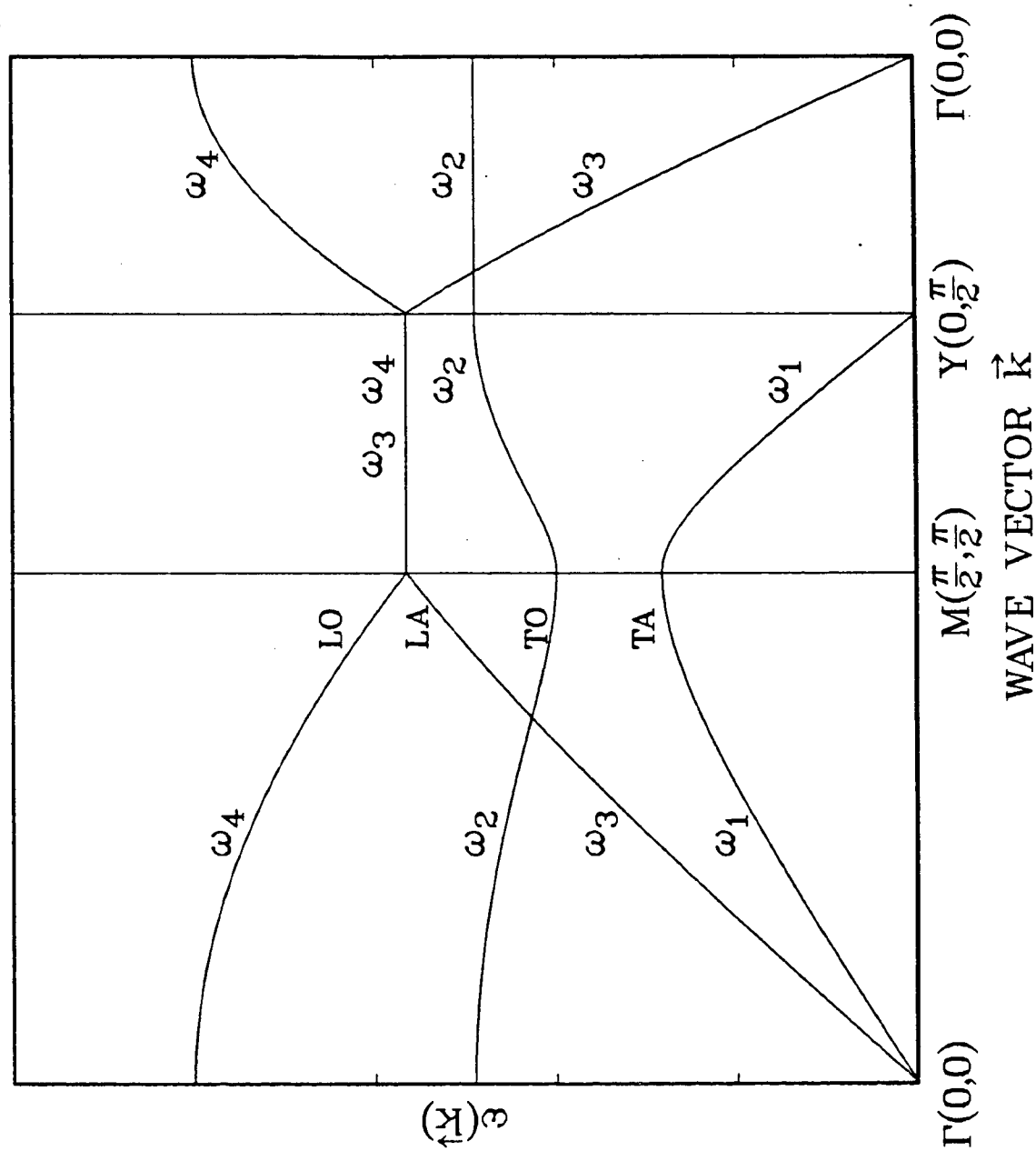

Figure 4-5 The frequency dispersion curves for the two-dimensional model for the path $\Gamma \rightarrow M \rightarrow Y \rightarrow \Gamma$. The branches have been labelled according to which solution they correspond to. Along the path M→Y the transverse acoustic mode goes to zero, while the longitudinal acoustic mode remains constant, as does the longitudinal optic mode. The transverse modes depend only on q_x, and the longitudnal modes only depend on q_y; thus if either one of these variables is constant (as is the case along M→Y and Y→ Γ), then the corresponding mode will not change along the path.

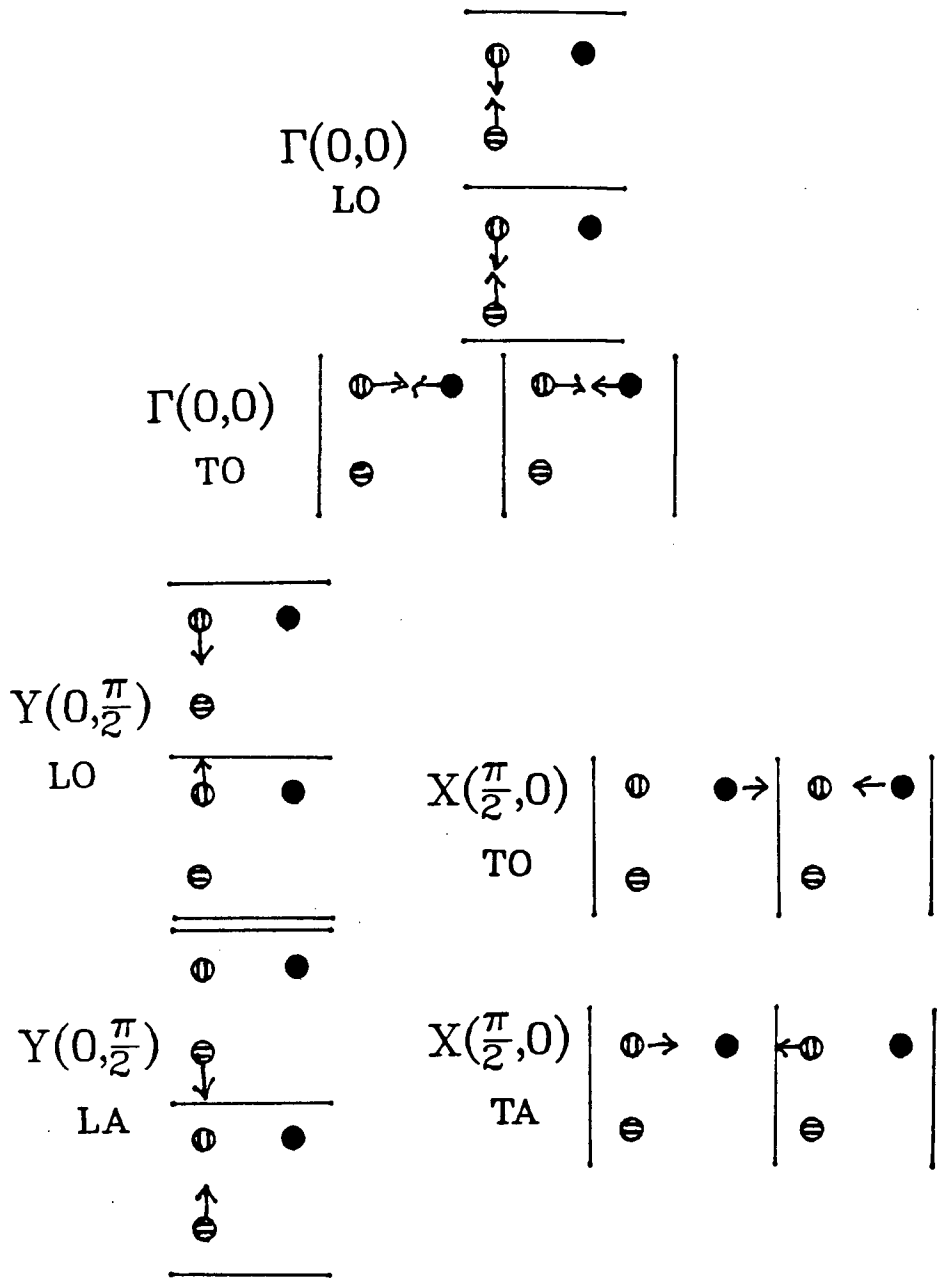

Figure 4-6 The eigenmodes of the optical phonons at Γ (the zone origin), the transverse optic and transverse acoustic phonons at X, and the longitudinal optic and longitudinal acoustic phonons at Y (the faces of the first Brillouin zone). The eigenmodes at the origin are the only ones that may be observed optically, unless zone folding occurs. Note that the zone-boundary longitudinal optic, longitudinal acoustic and and transverse acoustic involve just the TMTSF molecules.

optic modes. Along the $\Gamma \rightarrow X$ path the longitudinal acoustic phonon disappears, and along the $\Gamma \rightarrow Y$ path the transverse acoustic phonon disappears. The eigenmodes for the phonons at Γ (the zone origin) and X and Y (the zone faces) are shown in Fig. 4–6. The zone origin is chosen because these are the modes that may be activated using optical techniques. The zone faces show the eigenmodes of the acoustic phonons which are not active at the zone origin.

At the zone boundary only the longitudinal optic, longitudinal acoustic, and transverse acoustic phonons involve just the TMTSF molecules, however the longitudinal acoustic and longitudinal optic phonons are degenerate and are not really distinct. Thus, both the one- and the two-dimensional models have shown that the low frequency zone-boundary acoustic phonon involves just the TMTSF molecules.

4.4 An Estimate of the TMTSF Acoustic Phonon

An estimate of the zone-boundary phonon can be obtained based on sound velocity measurements along the a-axis. This corresponds to the longitudinal acoustic mode at the origin. From the previous section, we know that the frequency $\omega_3(\mathbf{q})$, which for convenience will be labeled $\omega_{LA}(\mathbf{q})$, is given by

$$\omega_{LA}^2(q_y) = \frac{K_1}{\mu_{12}} \left\{ 1 - \sqrt{1 - \frac{4m_1m_2}{(m_1+m_2)} \sin^2(q_y a)} \right\}. \qquad (4-15)$$

For this mode, $m_1 = m_2$, equation 4–15 may be rewritten

$$\omega_{LA}(q_y) = \left(\frac{K_1}{\mu_{12}}\right)^{\frac{1}{2}} \left\{ 1 - \sqrt{1 - \sin^2(q_y a)} \right\}^{\frac{1}{2}}. \qquad (4-16)$$

The velocity of sound, v_s, at the zone origin is defined as

$$v_s = \left. \frac{\partial \omega_a}{\partial q_y} \right|_{q_y=0}. \qquad (4-17)$$

Substituting equation 4–16 into 4–17 and evaluating in the limit as $q_y \rightarrow 0$, since direct substitution yields an indeterminant value, gives the expression

$$v_s = \left(\frac{K_1}{\mu_{12}}\right)^{\frac{1}{2}} \frac{a}{\sqrt{2}} \text{ cm/s} \qquad (4-18)$$

or

$$K_1 = \frac{2\mu_{12}v_s^2}{a^2} \text{ g/s}^2. \qquad (4-19)$$

Note that we are working with cgs units. The velocity of sound has been measured in $(TMTSF)_2FSO_3$[88] by Lacoe *et al.* and found to be

$$v_s^{FSO_3} = 3.8 \times 10^5 \text{ cm/s } (\pm 25\%)$$

and in $(TMTSF)_2PF_6$[89] by Chaikin *et al.*

$$v_s^{PF_6} = 3.1 \times 10^5 \text{ cm/s } (\pm 5\%)$$

along the **a**-axis. The large error in the FSO_3 crystal is due to problems with the sample dimensions. The mass of the TMTSF molecule is 448.05 amu, thus the reduced mass is $\mu_{12} = 3.7189 \times 10^{-22}$ g. The distance between the anions is taken to be 7.266 Å[15], which is twice the lattice spacing in our model, that is $2a$, thus $a = 3.633 \times 10^{-8}$ cm. Using these values and the velocity of sound for the PF_6 compound and substituting into equation 4–19 gives the value for the spring force constant K_1

$$K_1 = 5.371 \pm 0.537 \times 10^4 \text{ gm/s}^2.$$

At the zone boundary, equation 4–16 becomes

$$\omega_{LA}(\frac{\pi}{a}) = \sqrt{\frac{K_1}{\mu_{12}}} \text{ rads/s.} \qquad (4-20)$$

Thus the angular frequency of the phonon at the zone boundary is

$$\omega_{LA}(\frac{\pi}{a}) = 1.202 \pm 0.06 \times 10^{13} \text{ rad/s}.$$

This, however, is the angular frequency. Recalling that $f = \frac{\omega}{2\pi}$, then

$$f_{LA}(\frac{\pi}{a}) = 1.912 \pm 0.095 \times 10^{12} \text{ Hz}.$$

Finally, the conversion factor to wave numbers is $1\text{cm}^{-1} = 3.0 \times 10^{10}$ Hz (some other useful relations are given in Appendix A). The longitudinal acoustic phonon is calculated to have a frequency of

$$\nu_{LA}(\frac{\pi}{a}) = 63.73 \pm 3.19 \text{ cm}^{-1}.$$

It is not unusual for the frequency of the transverse acoustic phonon to be half that of the longitudinal phonon[90]. For the choice of masses and spring force constants (which are reasonable in view of the fact that no accurate data for the intermolecular restoring forces is available) in this simple model, we get the result that at the zone boundary the transverse acoustic phonon is half the frequency of the longitudnal acoustic phonon. Thus, it would not be unrealistic to expect the transverse acoustic phonon to have a frequency of

$$\nu_{TA}(\frac{\pi}{a}) \sim 30 \text{ cm}^{-1}.$$

These simple models show that 30 cm^{-1} is a reasonable estimate of the zone-boundary transverse acoustic phonon, and that such a mode would likely involve just the TMTSF molecule.

CHAPTER 5

CONCLUSIONS

5.1 Conclusions

The compounds with centrosymmetric and non-centrosymmetric anions (anions with octahedral and tetrahedral symmetry) show behavior which is both different and similar. The presence of four sharp resonances, three external modes and one internal mode, is common to all of the $(TMTSF)_2X$ salts examined. They are very sharp, however, in the compounds with octahedral anions. Those compounds with tetrahedral anions undergo anion-ordering transitions which results in the formation of a superlattice. Thus, zone-boundary phonons which are infrared inactive are mapped back to the origin where they may become infrared active. The four resonances are broad due to disorder effects, and are accompanied by multiplets and shoulders in the compounds with $2a \times 2b \times 2c$ superlattice (BF_4 and ReO_4), but are well defined in the ClO_4 compound with the superlattice along just one transverse direction $a \times 2b \times c$. In addition to these features, there is a prominent feature at $\sim$ 30 cm^{-1} in all of the tetrahedral-anion compounds. From its behavior as a function of temperature, and the fact that it appears in all three of these compounds, it is likely that this feature is a zone-boundary transverse acoustic phonon that has a similar frequency in all of the compounds. Calculations using simple models support this conclusion. This feature is very strong, due probably to electron-phonon coupling and it may be related to the superconductivity.

Extended measurements only yield information on internal modes that are common to all of the $(TMTSF)_2X$ salts examined. The tetrahedral anion salts, however, show evidence of zone folding in this region. Anion internal modes are identified, as well as a TMTSF methyl torsional mode.

5.2 Suggestions for Future Experiments

The "30 cm^{-1}" feature represents some very elegant physics, although it is questionable whether or not it is associated with FSC. It is interesting to note that all of the compounds in which it has been observed so far have anion-ordering transitions along the **b**-axis, which appears to be necessary for superconductivity. $(TMTSF)_2NO_3$, however, has an anion-ordering transition along the **a**-axis, resulting in a $2a \times b \times c$ anion superlattice and has been found not to exhibit superconductivity under pressure[14]. If the "30 cm^{-1}" feature is a transverse acoustic phonon, then because it is completely polarized in the transverse direction, it should not be activated by a superlattice formed along the stack direction. That is, at Y in the reciprocal lattice, and along the $\Gamma \rightarrow$Y direction, this mode is not infrared active. The formation of the superlattice would fold Y back to the origin; however, only the longitudnal acoustic phonon could be activated in this manner. It is possible that a longitudnal acoustic phonon might become infrared active, and thus one would observe a feature similar to the one at 30 cm^{-1}, but at roughly twice the frequency (nominally at 60 cm^{-1}).

The assignments of the methyl torsion modes are not certain, and these measurements should be extended. In the future, the crystals should be weighed. This would allow an approximate figure for the powder absorption coefficient, α, to ± 20 %.

BIBLIOGRAPHY

[1] R.L. Greene and G.B. Street, *Science*, **229**, 651 (November 1984).

[2] A.J. Epstein and J.S. Miller, *Sci. Am.*, **241**, 52 (October 1979).

[3] K. Bechgaard and D. Jérome, *Sci. Am.*, **247**, 50 (july 1982).

[4] W.A. Little, *Phys. Rev. A*, **134**, 1416 (1964).

[5] J. Bardeen, L.N. Cooper and J.R. Schriffer, *Phys. Rev.*, **108**, 1175 (1957).

[5] K. Bechgaard and D. Jérome, *Sci. Am.*, **247**, 50 (July 1982).

[6] R.E. Peierls, *Quantum Theory of Solids*, (Oxford University Press, London), 108.

[7] J. Bardeen, *Solid State Commun.*, **13**, 357 (1973).

[8] L.B. Coleman, M.J. Cohen, D.J. Sandman, F.G. Yamagishi, A.F. Garito and A.J. Heeger, *Solid State Commun.*, **12**, 1125 (1973).

[9] D. Allender, J.W. Bray and J. Bardeen, *Phys. Rev. B*, **9**, 119 (1974).

[10] P.A. Lee, T.M. Rice and P.W. Anderson, *Solid State Commun.*, **14**, 703 (1974).

[11] K. Bechgaard, C.S. Jacobsen, K. Mortensen, H.J. Pedersen and N. Thorup, *Solid State Commun.*, **33**, 1119 (1980).

[12] D. Jérome, A. Mazaud, M. Ribault and K. Bechgaard, *J. Phys Lett. (Paris)*, **41**, L95 (1980).

[13] T.J. Kistenmacher, *Solid State Commun.*, **51**, 931 (1984).

[14] M.A. Beno, J.W. Williams, M.M. Lee and D.O. Cowan, *Solid State Commun.*, **44**, 1195 (1982).

[15] N. Thorup, G. Rindorf, H. Soling and K. Bechgaard, *Acta. Crst. B*, **37**, 1236 (1981).

[16] K. Bechgaard, *Mol. Cryst. Liq. Cryst.*, **79**, 1 (1982).

[17] H. Kobayashi, A. Kobayashi, G. Saito and H. Inokuchi, *C.S.J Chem. Lett.*, 245 (1982).

[18] G. Rindorf, H. Soling and N. Thorup, *Acta. Cryst. B*, **38**, 2805 (1982).

[19] T.J. Emge, M.A. Beno, C.A. Daws, H.H. Wang and J.W. Williams, *Mol. Cryst. Liq. Cryst.*, **116**, 153 (1984).

[20] P.M. Grant, *J. Phys. Colloq. C3 (Paris)*, **44**, 847 (1983).

[21] *Chem. Scripta*, **17**, 85 (1981).

[22] J.P. Pouget, R. Moret, R. Comes and K. Bechgaard, *Mol. Cryst. Liq. Cryst.*, **79**, 129 (1982).

[23] P.C.W. Leung, A.J. Schultz, H.H. Wang, T.J. Emge, G.A. Ball, D.D. Cox and J.M. Williams, *Phys. Rev. B*, **30**, 1615 (1984).

[24] R. Moret, J.P. Pouget, R. Comes and K. Bechgaard, *Phys. Rev. Lett.* **49**, 1008 (1982).

[25] K. Andres, F. Wudl, D.B. McWhan, G.A. Thomas, D. Nalewajek and A.L. Stevens *Phys. Rev. Lett.*, **45**, 1449 (1980).

[26] M. Ribault, G. Benedek, D. Jérome and K. Bechgaard, *J. Phys. Lett. (Paris)*, **41**, L397 (1980).

[27] R.L. Greene and E.M. Engler, *Phys. Rev. Lett.*, **45**, 1587 (1980).

[28] M. Ribault, J.P. Pouget, D. Jérome, K. Bechgaard, *J. Phys. Lett. (Paris)*, **41**, L607 (1980).

[29] S.S.P. Parkin, M. Ribault, D. Jérome and K. Bechgaard, *J. Phys. C*, **14**, L445 (1981).

[30] A. Fournel, C. More, G. Roger, J.P. Sorbier, J.M. Delrieu, D. Jérome, M. Ribault and K. Bechgaard, *J. Phys. Lett. (Paris)*, **42**, L445 (1981).

[31] C. More, G. Roger, J.P. Sorbier, D. Jérome, M. Ribault and K. Bechgaard, *J. Phys. Lett. (Paris)*, **42**, L313 (1981).

[32] J.C. Scott, H.J. Pedersen and K. Bechgaard, *Phys. Rev. B*, **24**, 475 (1981).

[33] K. Mortensen, Y. Tomkiewicz and K. Bechgaard, *Phys. Rev. B*, **25**, 3319 (1982).

[34] K. Mortensen, Y. Tomkiewicz, T.D. Schultz and E.M. Engler, *Phys. Rev. Lett.*, **46**, 1234 (1981).

[35] L.J. Azvedo, J.E. Schirber and E.M. Engler, *Phys. Rev. B*, **29**, 464 (1984).

[36] D. Jérome and H.J. Schultz, *Adv. in Phys.*, **31** 299 (1982).

[37] R. Brusetti, M. Ribault, D. Jérome and K. Bechgaard, *J. Phys. (Paris)*, **43** 52 (1982).

[38] P.M. Chaikin, G. Grüner, E.M. Engler and R.L. Greene, *Phys. Rev. Lett.*, **23**, 1874 (1980).

[39] W.M. Walsh, Jr., F. Wudl, G.A. Thomas, D. Nalewajek, J.J. Hauser, P.A. Lee and T. Poehler, *Phys. Rev. Lett.*, 45, 829 (1980).

[40] H.H.S Javadi, S. Sridhar, G. Grüner, L. Chaing and F. Wudl, *submitted to Phys. Rev. Lett.*

[41] R.L. Green, P. Haen, S.Z. Huang, E.M. Engler, M.-Y. Choi and P.M. Chaikin, *Mol. Cryst. Liq. Cryst.*, **79**, 183 (1982).

[42] S.S.P. Parkin, D. Jérome and K. Bechgaard, *Mol. Cryst. Liq. Cryst.*, **79**, 213 (1982).

[43] K. Bechgard, K. Carneiro, M. Olsen, F.B. Rasmussen, C.S. Jacobsen, *Phys. Rev. Lett.*, **46**, 852 (1981).

[44] S.S.P Parkin, M. Ribault, D. Jérome and K. Bechgaard, *J. Phys. C : Solid State Phys.*, **14**, L445 (1981).

[45] H. Schwenk, K. Andres and F. Wudl, *Phys. Rev. B*, **27**, 5846 (1983).

[46] P. Garoche, R. Brusetti, D. Jérome and K. Bechgaard, *J. Phys. Lett. (Paris)*, **43**, L147 (1982).

[47] C.S. Jacobsen, H.J. Pedersen, K. Mortensen, G. Rindorf, N. Thorup, J.B. Torrance and K. Bechgaard, *J. Phys. C : Solid state Phys.*, **15**, 2651 (1982).

[48] P. Garoche, R. Brusetti and K. Bechgaard, *Phys. Rev. Lett.*, **49**, 1346 (1982).

[49] T. Takahashi, D. Jérome and K. Bechgaard, *J. Phys. Lett. (Paris)*, **43**, L565 (1982).

[50] D.U. Gubser, W.W. Fuller, T.O. Poehler, D.O. Cowan, M. Lee, R.S. Potember, L-Y. Chaing and A.N. Bloch, *Phys. Rev. B*, **24**, 478 (1981). and P.M. Chaikin,

[51] H.K. Ng, T. Timusk and K. Bechgaard, *J. Phys. Colloq. C3 (Paris)*, **44**, 867 (1983).

[52] W.A. Challener, P.L. Richards and R.L. Greene, *J. Phys Colloq. C3 (Paris)*, **44**, 873 (1983).

[53] W.A. Challener, P.L. Richards and R.L. Greene, *Solid State Commun.*, **51**, 765 (1984).

[54] J.E. Eldridge and G.S. Bates, *Mol. Cryst. Liq. Cryst.*, **119**, 183 (1985).

[55] C.S. Jacobsen, D.B. Tanner and K. Bechgaard, *Phys. Rev. B*, **28**, 7019 (1983).

[56] J.E. Eldridge and G.S. Bates, *to be published.*

[57] H.K. Ng, T. Timusk and K. Bechgaard, *phys. Rev. B*, **30**, 5824 (1984).

[58] H.K. Ng, *Unpublished Ph.D. Thesis, McMaster University*, (1984).

[59] J.E. Eldridge and Frances E. Bates, *Phys. Rev. B*, **28**, 6972 (1983).

[60] J.E. Eldridge, *Phys. Rev. B*, **31**, 5465 (1985).

[61] F. Wooten, *Optical Properties of Solids*, (Academic Press, 1972), Appendix G.

[62] T.S. Moss, *Optical Properties of Semiconductors*, (Butterworth Publications Ltd., London, 1959) p. 25.

[63] R. Bozio, C. Pecile, K. Bechgaard, F. Wudl and D. Nalewajek, *Solid State Commun.*, **41**, 905 (1982).

[64] M. Meneghetti, R. Bozio, I. Zanon, C. Pecile, G. Ricotta, and Miranda Zanetti, *J. Chem. Phys.*, **80**, 6210 (1984).

[65] H.J. Schultz, *Mol. Cryst. Liq. Cryst.*, **79**, 199 (1982).

[66] H.J. Schultz, D. Jérome, A. Mazaud, M. Ribault and K. Bechgaard, *J. Phys. (Paris)*, **42**, 991 (1981).

[67] D. Djurek, M. Prester, D. Jérome and K. Bechgaard, *J. Phys. C*, **15**, L669 (1982).

[68] M.-Y. Choi, P.M. Chaikin, S.Z. Huang, P. Haen, E.M. Engler and R.L. Green, *Phys. Rev. B*, **25**, 6208 (1982).

[69] J.J. Hauser, *Phys. Rev. B*, **11**, 738 (1975).

[70] M.M. Lee, J.P. Stakes, F.W. Wigal, T.J. Kistenmacher, D.O. Cowan, T.O. Poehler, A.N. Bloch, F.W. Fuller and D.U. Gubser, *Mol. Cryst. Liq. Cryst.*, **79**, 145 (1982).

[71] Strem Chemicals Ltd.

[72] a) A. Moradpour, V. Peyrussan, I. Johansen and K. Bechgaard, *J. Org. Chem.*, **48**, (1983).

[73] P.H. Martin and E. Puplett, *Infrared Phys.*, **10**, 105 (1969).

[74] Janis Research Company, 22 Spencer Street, Stoneham, Mass.

[75] Infrared Laboratories, Inc., 1808 E. 17 th St., Tucson, Arizona 85710.

[76] Pye Unicam Ltd., York Street, Cambridge, England. CB1 2PX

[77] M.L. Forman, W.H. Steel and G.A. Vanasse, *J. Opt. Soc. Am.*, **56**, 59 (1966).

[78] H. Happ and L. Genzel, *Infrared Phys.*, **1**, 39 (1961).

[79] P.R. Bevington, *Data Reduction and Error Analysis for the Physical Sciences*, McGraw–Hill, New York (1969).

[80] Two–phonon "difference" processes, which are very temperature dependent, will be the main mechanism of relaxation of these vibrations in this energy region (see J.E. Eldridge and P.R. Staal, *Phys. Rev. B*, **16**, 4608 (1977).

[81] J.E. Eldridge and Frances E. Bates, *Phys. Rev. B*, **26**, 1590 (1982).

[82] E. Burges, H. Banadeo and E. D'Alessio, *J. chem. Phys.*, **65**, 2460 (1976).

[83] Frances E. Bates, *private communication.*

[84] W.E. Moerner, A.R. Chraplyvy and A.J.Sievers, *Phys. Rev. B*, **29**, 6694 (1984).

[85] J.E. Eldridge, *Phys. Rev. B*, **6**, 3128 (1972).

[86] K. Nakamoto, *Infrared and Raman Spectra of Inorganic and Coordination Compounds, Third Edition*, John Wiley & Sons, New York (1963).

[87] N.W. Ashcroft and N.D. Mermin, *Solid State Physics*, Holt, Rinehart and Winston, Saunders College, p. 437 (1976).

[88] R.C Lacoe, P.M. Chaikin, F. Wudl, S.D. Cox and J. Brennan, *Mol. Crst. Liq. Cryst.*, **119**, 155 (1985).

[89] P.M. Chaikin, T. Tiedje and A.N. Bloch, *Solid State Commun.*, **41**, 739 (1982).

[90] H.A. Mook and C.R. Watson, Jr., *Phys. Rev. Lett.*, **36**, 801 (1976).

APPENDIX A

$$
\begin{aligned}
1\ \mathrm{cm}^{-1} &= 124\ \mu\mathrm{eV} \\
&= 3 \times 10^{10}\ \mathrm{Hz} \\
&= 1.9 \times 10^{11}\ \mathrm{rad/s} \\
&= 1.44\ ^{\circ}\mathrm{K} \\
&= 10.7\ \mathrm{kG} \\
&= 2.1 \times 10^{-1}\ (\Omega\,\mathrm{cm})^{-1} \\
1\ \mathrm{amu} &= 1.66043 \times 10^{-24}\ \mathrm{g}
\end{aligned}
$$